Nano Positioning Control Using Magnetostrictive Actuators

by

Sina Valadkhan

A thesis
presented to the University of Waterloo
in fulfillment of the
thesis requirement for the degree of
Doctor of Philosophy
in
Mechanical Engineering

Waterloo, Ontario, Canada, 2007

I hereby declare that I am the sole author of this thesis. This is a true copy of the thesis, including any required final revisions, as accepted by my examiners.

I understand that my thesis may be made electronically available to the public.

Abstract

The focus of this thesis is on the development of control systems for nano-positioning actuators using magnetostrictive materials. Magnetostrictive materials have large strokes and fast responses. However, they are less commonly used than other smart materials such as piezoceramics due to their highly nonlinear and hysteretic behaviour.

It is necessary to arrive at an accurate model which can predict the material response at any magnetic field and load condition. Furthermore, due to the nonlinearity of the material, a closed-loop feedback system with a stabilizing controller is needed.

Different hysteresis models for magnetostrictive materials are implemented and compared. Since load-dependence is one of the main features of hysteresis for magnetostrictive materials, load-dependent models are studied. An existing load-dependent model is implemented and compared with a new load-dependent hysteresis model which is developed by energy considerations.

Passivity of the magnetostrictive system was shown using a physical argument. The results are used to develop a stabilizing controller. Using the properties of the Preisach model, an alternative approach for controller design is proposed. Tracking properties and stability of the controllers were shown.

An experimental setup has been developed for data collection and model and controller evaluation.

Acknowledgements

This thesis has been written with the help, support, and advice of many people to whom I am greatly in debt. I would like to thank my supervisors Kirsten Morris and Amir Khajepour for their help, patience, support, friendship, and trust in giving me the freedom to try my own ideas. I wish to acknowledge the members of my committee Robert Gorbet, Ralph Smith, Stephen Corbin, and Zoran Miskovic for their useful comments, suggestions and discussions.

I would like to thank Robert Wagner for his friendship, sense of humor and help with machining and mechanical parts. I wish to express my gratitude to Jan Huissoon and Robert Gorbet for lending equipment. I would like to acknowledge my co-workers and lab mates Alex Shum, Michael Wybenga, Babak Ebrahimi, Hanieh Aghighi, Nima Eslaminasab, and Siamak Arzanpour for the time we spent together, their friendship, and welcome distractions.

I appreciate the friendship and support of my friends. I wish to thank Fatemeh Jafargholi, Hanif Bayat Movahed, Gianfranco Mazzanti, Weihong Huang, James Chan, Dongping Qi, Maria Khomenko, Mohadeseh Azimlu, Shahla Aliakbari, Gaven McDonald, Houshin Nejati, Kaveh Khojasteh, Sattar Taheri Araghi, Ali Tabei, Parisa Bohlouli, Kourosh Afrousheh, Reyhaneh Bassam, Roshanak Teymoori, Saeed Behzadipour, Mahdieh Sadat Emrani, Mohamad Moraghebi, Afsaneh Kohandani, and Amjad Ashoorion for their friendship and companionship.

Finally, I wish to thank my wife and best friend Zahra Fakhraai for her love, kindness, and support at all times. She made my life much more enjoyable and without her, this thesis would not be possible.

Contents

List of Tables

List of Figures

Chapter 1

Introduction

In recent years, a growing demand for micropositioning actuators has been seen in industry. Micropositioning actuators are now commonly used for optical fiber alignment, biological cell micromanipulation, scanning microscopes and chip manufacturing. Currently, most of the micropositioning actuators are made of piezoceramic materials because of their fast response time and almost linear behaviour.

Still, there is a demand for actuators with a higher force, larger stroke and faster response time. For this purpose, the possibility of using other active materials for actuation has been examined in the past decade. Among possible choices, Terfenol-D, a magnetostrictive material, is a competitive choice. Terfenol-D is an alloy of iron, terbium and dysprosium. In Figure 1-1 a rod made of Terfenol-D is shown. Terfenol-D is a brittle metal and cannot stand tension or shear. It reacts to a magnetic field, to which, it becomes larger in size. Terfenol-D is not polarized; that is, regardless of the direction of a magnetic field, it becomes longer. Because of the required magnetic field for the excitation, Terfenol-D actuators are usually larger in size compared to piezoceramic stack actuators. However, because of the large force and strain they produce, they are an attractive choice in many applications. Terfenol-D also has a very fast response time which makes it suitable for high-frequency applications [20].

Terfenol-D provides more displacement (about 50% more) compared to piezoceramics. But, it is less commonly used partly because it is highly nonlinear and its underlying physics and

Figure 1-1: Terfenol-D rod (top) and cold-rolled steel rod (bottom).

magneto-mechanical response are not fully understood. Terfenol-D, like other magnetic materials, has hysteresis. Because of its nonlinearity and hysteresis, Terfenol-D actuators are difficult to control. In many micropositioning tasks, sub-micron accuracy is required. This requires an accurate hysteresis model and control system. For this purpose, extensive research in hysteresis modeling and control is underway.

To achieve the required performance, Terfenol-D actuators need to be used in a closed-loop feedback system. External physical conditions affect the hysteretic behaviour of magnetostrictive materials. The shape of the hysteresis curve changes significantly if the mechanical loading is changed. Development of a feedback control considering the dependence of hysteresis on many physical conditions together with intrinsic nonlinearity of the system is difficult and complex. Furthermore, robust stability is needed before the actuator can be used in a real application.

In [57], a test rig was designed for measuring different parameters of a Terfenol-D sample. From this test rig, a set of experimental curves was obtained for a fixed stress. These curves were used in three existing hysteresis models, and the ease of use and accuracy of these models were discussed and compared.

This thesis is a continuation of [57]. Several upgrades are done on the test rig. A new set of experimental data is obtained under different loading conditions. A new load-dependent hysteresis model is developed and compared with an existing load-dependent hysteresis model. The accuracy of the models are discussed.

In this thesis, a new approach is used to establish stability for Terfenol-D closed-loop feedback system. Using a physical argument, it is shown that Terfenol-D actuators satisfy a passivity condition. This passivity result is not based on any model for Terfenol-D hysteresis, that is, this result holds for any model. The storage function is found and discussed for the homogenized energy model. This result is used to design a stabilizing velocity controller for the system.

A PI (proportional-integral) controller is used to develop a position controller for the magnetostrictive actuator. It is shown that if the hysteretic system satisfies certain assumptions, tracking and stability is guaranteed. The validity of assumptions are discussed. These results are used to develop a position controller and an alternative velocity controller.

The controllers discussed here are simulated using a Preisach model. Numerical optimization is used to find the optimal controller parameters. The optimization is subjected to stability constraints. The optimal controller is evaluated experimentally and the results are discussed.

The outline of this thesis is as follows: In Chapter 2, background and related literature is reviewed. Chapter 3 discusses the hysteresis models for Terfenol-D and its load-dependent behaviour. In Chapter 4, the closed-loop control of magnetostrictive actuators is discussed. Related background material, passivity of magnetostrictive actuators and velocity and position controllers are included in this chapter. The experimental apparatus used in this thesis is explained in Chapter 5. The optimization and experimental evaluation of the controllers are also discussed in this chapter. This thesis in concluded in Chapter 6.

Chapter 2

Review of hysteresis models

In this chapter, background and literature related to the modeling of magnetostrictive materials are reviewed. In the first section, the hysteresis curve and related terminology is discussed. Since the most important nonlinearity in magnetostrictive materials is their hysteresis, the existing models for hysteresis are discussed next. In Section 3 modeling of magnetostrictive materials in particular is reviewed.

2.1 Hysteresis curve

A hysteresis curve is a plot of system output versus system input for one or more cycles. For magnetic materials, it is a plot of magnetization M versus magnetic field H. Two typical hysteresis curves are shown in Figure 2-1. This shape of curve is called sigmoid, which is seen frequently in many physical phenomena.

In this figure, the inner curve is obtained when the input is oscillating between $+a$ and $-a$ and the outer curve when the input is oscillating between $+H_{sat}$ and $-H_{sat}$. In each curve, the upper part is for when H is decreasing, and the lower part is for when H is increasing. The magnetization reaches a final value when the absolute value of H becomes larger than a specific value H_{sat}. This is called the saturation of the material.

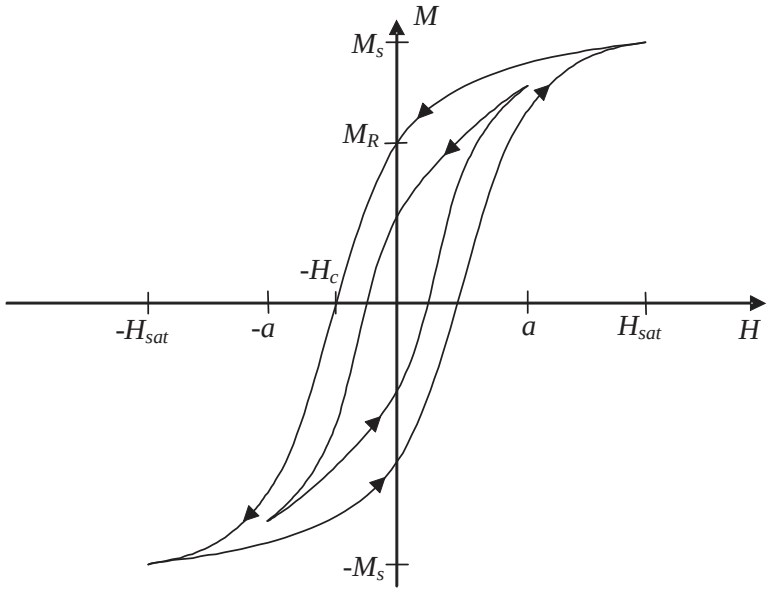

Figure 2-1: Two typical hysteresis curves.

The hysteresis curve when the input is oscillating between $+H_{sat}$ and $-H_{sat}$ is called "the major loop", which is the outer curve in Figure 2-1. If the input oscillates between any other value, especially if it is not symmetric about zero, the produced curve is called a minor loop. Minor loops always lie inside the major loop.

Suppose that the magnetic field H is large enough so that the material is saturated. If H is brought back to zero monotonically, the magnetization M is not decreased to zero; instead it will decrease to a positive nonzero value which is called "the remanence magnetization". This point is labeled M_R in Figure 2-1. If zero magnetization is requested, H needs to be further decreased. At some negative value of H, the magnetization is zero. The absolute value of this magnetic field H is called "the coercive force" H_C, as shown in Figure 2-1. The coercive force is a measure of the strength of the material when it is used as a permanent magnet. For more details about the formal theory of magnetic materials, see [35].

2.2 Hysteresis models

It is more than 70 years since magnetic hysteresis was first studied and there is still much active research in this field. There are many models for magnetic hysteresis and it would be impossible to mention all of them here [33, 64, 27, 57, 29]. In this section the most common hysteresis models are reviewed.

2.2.1 Preisach model

The Preisach model [33] is the most common and probably the most important hysteresis model in the literature. It is used for many hysteretic systems [62, 18, 19]. This model is not based on any physical model of hysteretic materials and has a mathematical structure which can generate curves like the sigmoid curve. It was developed about seventy years ago for magnetic materials.

In this model, the output, magnetization, is the weighted sum of the output of a continuum of hysteresis relays. The output of each relay can be either $+1$ or -1, which is determined by the input, H field. Although this model is not explicitly based on any physical model, its structure is intuitively related to the formal theory of magnetic materials. Magnetic materials are believed to be made of a large number of magnetic dipoles. Each dipole is like a small permanent magnet. The dipoles are allowed to rotate in their places and the final magnetization is the aggregation of magnetizations of dipoles. Each Preisach relay is intuitively related to one of the dipoles.

Model structure

The basis of this model is the hysteresis relay shown in Figure 2-2. Model input, which is shown in the horizontal axis, is directly fed to this relay. The output of the relay, which is shown in vertical axis, is used for computing the model output.

The output of this relay is either $+1$ or -1. The relay retains its state unless the input passes $s + r$ or $s - r$. If the relay is in $+1$ state and the input goes less than $s - r$, the relay

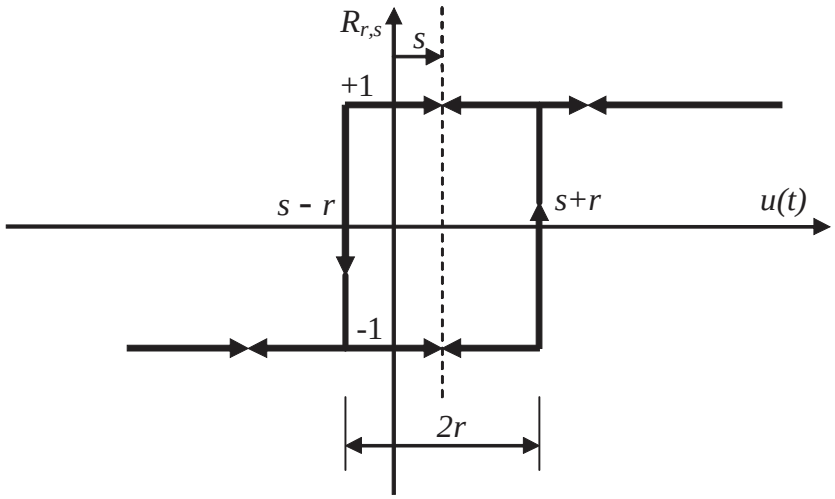

Figure 2-2: The hysteresis relay.

switches to -1, and if the relay is in -1 state and the input goes above $s+r$, the relay switches to $+1$ state, otherwise, the output remains the same.

The output of the model is:

$$y(t) = \int \int R_{r,s}[u(\cdot)](t)\mu(r,s)drds \tag{2.1}$$

Here, $u(t)$ is the input, $R_{r,s}[u(\cdot)](t)$ is the output of the relay, $\mu(r,s)$ is a weight function, and $y(t)$ is the model output. As it can be seen, an infinite number of relays with different s and r are used, and their outputs, after being multiplied by a weight function $\mu(r,s)$, are added together to form the output of the model. The weight function $\mu(r,s)$ is determined by experimental data for the material.

Preisach plane

At first, this model looks very difficult to implement and simulate since it appears to need unlimited memory for its unlimited number of relays. In fact, there is no need to have unlimited memory to store the state of the system. It has been shown that the state of the system can be described by a finite sequence of numbers [17]. This great simplification is done by the introduction of the Preisach plane.

Consider a two-dimensional coordinate system with variables r and s as shown in Figure 2-3. There is a one-to-one relationship between each point (r, s) on this plane and each Preisach relay. This plane is called the Preisach plane.

It is clear from Figure 2-2 that when $r < 0$, a valid relay is not represented, so the points left of the line $r = 0$ are not considered. Also, the points which are far from the origin are not concerned since the associated relays switch only when the input value is far from zero, which indicates the saturation state of the material. Since in the modeling, the saturated zone is not of interest, these relays and the associated points in the Preisach plane are not considered.

For simplicity and because the input is physically limited, it is assumed that the output will not change if the absolute value of the input becomes greater than a specific number, S. In that case $\mu(r, s) = 0$ if $|s + r| > S$ or $|s - r| > S$. This limits the active points of the Preisach plane to a triangle, shown in Figure 2-3.

The model input affects the status of Preisach relays. When a typical input is applied to the system, some of the relays takes the state of $+1$ and the others, -1. In the Preisach plane, a line separates the relays in $+1$ state from the relays in -1 state. Figure 2-4 shows a typical boundary. The Preisach plane boundary is usually composed of lines with a slope of $+1$ or -1 only. This boundary is very important since it describes the state of the system [17]. In fact, the location of the corners of the boundary determine the boundary and hence, the state of the system. You do not need to store the state of each relay; a sequence of numbers having the location of the corners is sufficient [17].

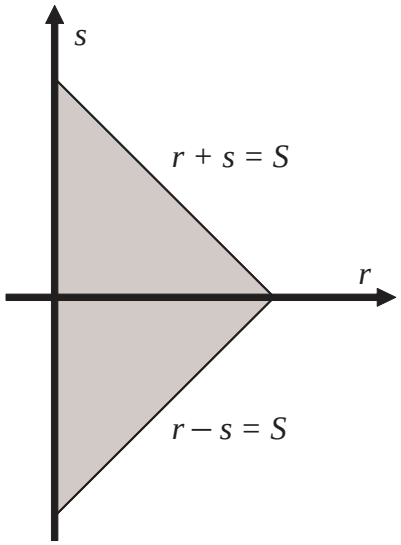

Figure 2-3: The Preisach plane.

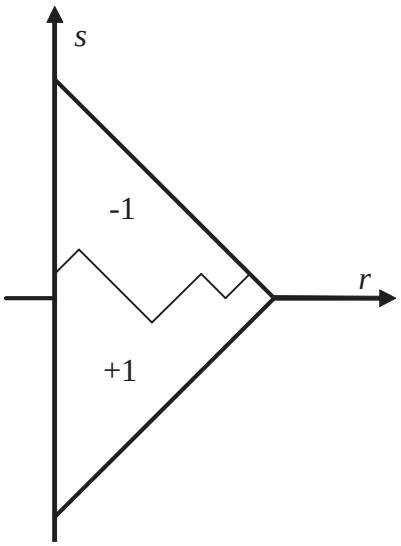

Figure 2-4: A typical Preisach plane boundary.

If the Preisach boundary is denoted by $s = \tau(t, r)$, the model output can be rewritten in terms of the boundary:

$$y(t) = \int_0^\infty \int_{-\infty}^{\tau(t,r)} \mu(r, s) ds dr - \int_0^\infty \int_{-\infty}^{\infty} \mu(r, s) ds dr. \tag{2.2}$$

Note that the Preisach boundary $\tau(t, r)$ and the vertical axis $r = 0$ in Figure 2-4 intersect at the current input value; that is,

$$\tau(t, 0) = u(t). \tag{2.3}$$

Consider the Preisach plane shown in Figure 2-5. Assume that the system state is initially represented by boundary 1 and the input is equal to u_1. If the input is reduced to u_2 the system state will change to boundary 2. The corners in boundary 1 no longer exist and it seems like the input is reduced from the positive saturation value monotonically. Since the system memory is stored in the corners of the Preisach boundary, the system effectively "forgets" the history of past extrema. This property of the Preisach model is called the "wiping-out property".

Another property of the Preisach model is the "congruent minor loop" property. Consider the Preisach boundaries shown in Figure 2-6 when for both systems, the input is oscillating between u_1 and u_2. Since the same area is swept, these systems experience the same change in the output. In this case, the minor loops generated by these systems will be similar in shape. In Figure 2-7, two congruent minor loops are shown. For more information about the Preisach model properties, see [33].

The wiping-out and congruent minor loop properties together form a necessary and sufficient condition for a Preisach representation [33]; that is, any Preisach model satisfies these properties and any hysteretic system satisfying these properties can be represented by a Preisach model.

The Preisach model is flexible, computationally fast and in most cases can represent the material hysteresis accurately, but it is relatively complex. Since its development, many mod-

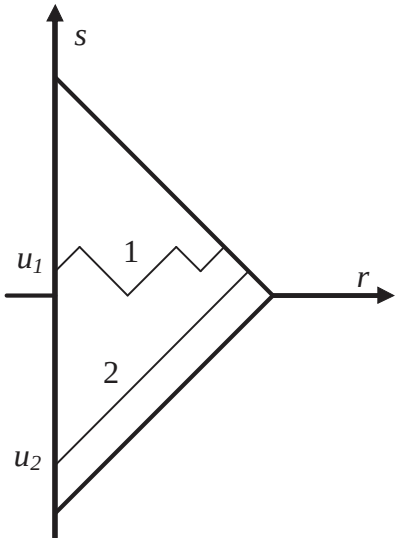

Figure 2-5: The wiping-out property.

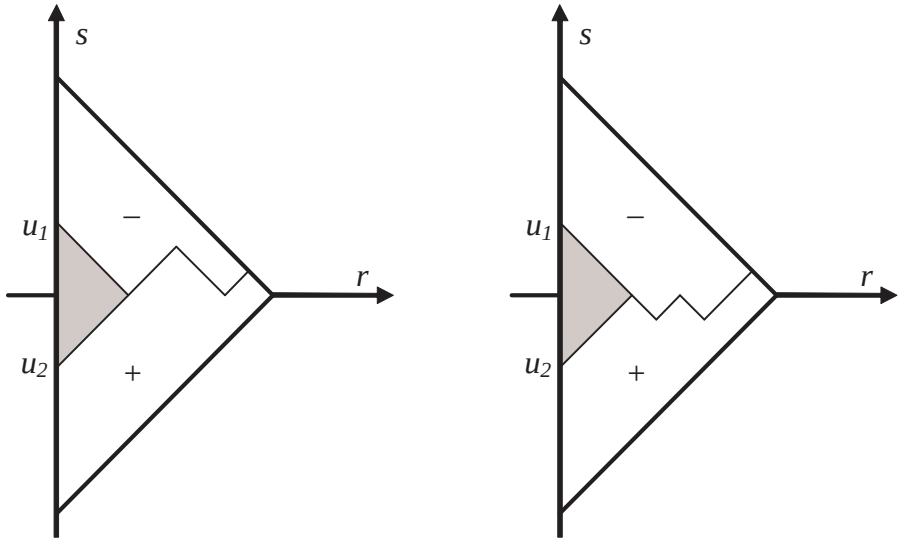

Figure 2-6: The congruent minor loops property.

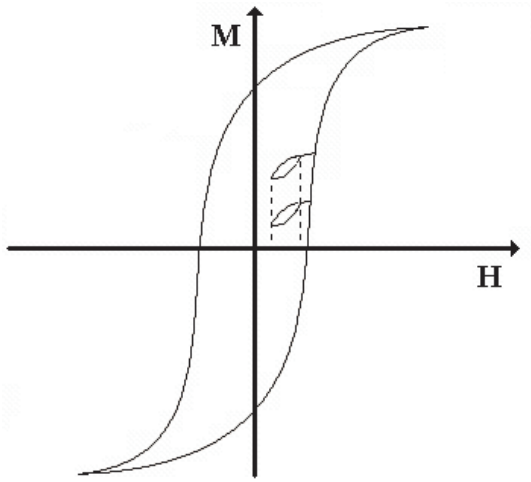

Figure 2-7: Congruent minor loops

ifications to this model have been made for improvement. In the following, some of these modifications are reviewed.

Modifications to Preisach model

There are many modified versions of the Preisach model. For example, in [43] an extension to the Preisach model is introduced to model magnetic materials in a broad temperature range.

In [48, 53, 54], a physical explanation for the Preisach model is introduced. The classical Preisach model is empirical and it is not directly based on any physical model of magnetic materials. In this explanation, a physical model of the material is introduced. Based on the Helmholtz free energy of a single dipole, a two-state magnetization is obtained. The bulk material is believed to have many of these dipoles so the macroscopic magnetization is found to be the average of magnetizations of a distribution of these dipoles. The result is similar to a Preisach model. This model is called the homogenized energy model and is fully discussed in Subsection 3.2.1 with reference to magnetostrictive materials.

A physical model similar to the Preisach model is presented in [5]. In this model, domain wall motion is the main magnetization mechanism. Here a single domain wall is modeled and

the magnetic behavior of the material is assumed to be the superposition of these domain wall models. This model proved to be efficient for commercial power ferrites [34].

2.2.2 Jiles-Atherton model

The Jiles-Atherton model [23, 24] is a physics-based model. In this model, domain wall motion is the mechanism for magnetization. The motion of a single domain wall is considered. Reversible and irreversible domain wall motions are introduced and based on them, two equations for reversible and irreversible magnetization are obtained. By combining them, the model is formulated. In this subsection, this model is briefly explained.

As stated before, there are a large number of magnetic dipoles in every magnetic material. Each of them has a very small contribution in the macroscopic magnetic properties of the matter. It is interesting to know that the magnetic direction of these dipoles are usually parallel to their neighbors. In fact, it is seen that these dipoles come in groups. In each group, almost all dipoles are parallel to each other. These groups are called the "magnetic domains". The border between different domains is called the "domain wall". In a demagnetized sample, domains are oriented randomly. If an external magnetic field is induced upon the material, domains that are parallel to the external magnetic field grow, and domains that are anti-parallel to the magnetic field shrink. This results in domain wall motion.

An irreversible domain wall motion happens when the entire domain wall is moved. The domain wall will not necessarily return to its previous position if the cause is removed. So this process is irreversible. The resulting magnetization is called the irreversible component of magnetization.

In the Jiles-Atherton model, the irreversible domain wall motion is modeled and a differential equation for the irreversible component of magnetization is obtained:

$$\frac{dM_{irr}}{dH} = \frac{(M_{an} - M_{irr})}{\delta k - \bar{\alpha}(M_{an} - M_{irr})} \tag{2.4}$$

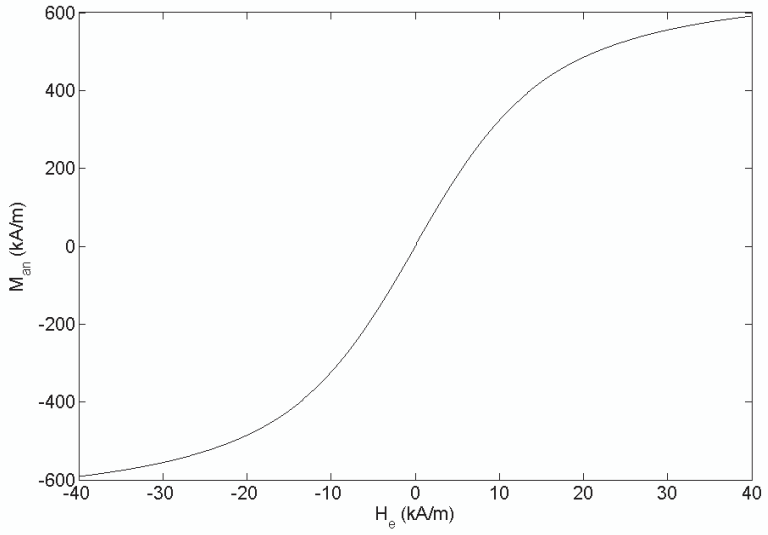

Figure 2-8: A plot of equation (2.5) for $a = 6.2\frac{\text{kA}}{\text{m}}$ and $M_s = 700\frac{\text{kA}}{\text{m}}$.

In this equation, M_{irr} is the irreversible component of magnetization. The parameters k, $\bar{\alpha}$ and μ_0 are constants. The parameter δ is $+1$ when H is increasing and -1 when it is decreasing. The parameter M_{an} is the anhysteretic magnetization, which is the magnetization for an ideal, pure and defect-less material with no hysteresis.

The form of anhysteretic curve depends on the material under discussion. For most cases the Langevin function can be used successfully for anhysteretic magnetization. This function was developed theoretically for paramagnetism [28], but it was extended to ferromagnetic materials by Weiss:

$$M_{an}(H_e) = M_s L\left(\frac{H_e}{a}\right) = M_s\left[\coth\left(\frac{H_e}{a}\right) - \frac{a}{H_e}\right] \tag{2.5}$$

In this equation, M_s is the saturation magnetization, a is a constant, $L(.)$ is the Langevin function and M_{an} is the anhysteretic magnetization. A plot of this equation is shown in Figure 2-8. The parameter H_e is the effective magnetic field defied by the following relation:

$$H_e = H + \bar{\alpha}M \tag{2.6}$$

A reversible domain wall motion is another source of magnetization. This happens when a domain wall bends. When the cause of bending is removed, the domain wall returns to its previous state, so this effect is reversible. The magnetization component produced when a domain wall is bent, is denoted by M_{rev}. In the Jiles-Atherton model, M_{rev} is given by the following relation:

$$M_{rev} = c(M_{an} - M) \tag{2.7}$$

where c is a constant. This equation and equation (2.4) are the equations which describe the Jiles-Atherton model. Note that $M = M_{irr} + M_{rev}$. An equation for anhysteretic magnetization, such as equation (2.5), is also needed.

This model is easy to implement and it has only a few parameters to adjust. This model was originally developed for hysteresis in magnetic materials, but it is shown that the idea of this model can be expanded to ferroelectric, ferroelastic and magnetostrictive materials [52]. This model, however, has some difficulties with minor loops. The model presented here does not produce closed minor loops. Since in most cases, the minor loops are closed, different modifications are proposed to close the loops. In [10], scaling is used to produce closed minor loops. In [21], equations (2.4) and (2.7) are modified to close the minor loops. For this modification, the input extrema should be known in advance. For applications in which the trajectory of the input is not predetermined, this approach cannot be used.

2.2.3 Stoner-Wohlfarth model

The Stoner-Wohlfarth model [55] is a physics-based model. The mechanism of magnetization in this model is the rotation of noninteracting dipoles. In this model, a single mechanism is used to explain both reversible and irreversible magnetization. Also it is a completely three

dimensional model. Unlike other models mentioned here, it does not need an extension to become a three-dimensional model. But, the effects of pinning sites (e.g. impurities) and dipole interactions are ignored in this model. Dipole interactions can be modeled by introduction of the effective magnetic field $H_e = H + \bar{\alpha}M$, where $\bar{\alpha}$ is a constant. If instead of H, H_e is used, a mean-field Stoner-Wohlfarth model [4] is obtained, which is supposed to be more accurate. It is shown that the mean-field Stoner-Wohlfarth model is useful for hard magnetic materials [4].

2.3 Models for magnetostrictive materials

Unlike magnetic materials, the study of magnetostrictive materials is relatively new, and hence, not much work is available in the literature. The hysteresis relation for magnetostrictive materials is coupled with mechanical variables (stress and strain). Also hysteresis curves for magnetostrictive materials are different from those of regular magnetic materials (Figure 2-9). Because of these differences, hysteresis models for magnetic materials cannot accurately model magnetostrictive materials. But still, most of the models for magnetostrictive materials are taken from the models for magnetic materials. Since the Preisach model is the most important hysteresis model for magnetic materials, it is more often used for magnetostrictive materials.

When the magnetic state (H and M) of magnetostrictive materials changes, it is seen that its mechanical state (strain and stress) is influenced. It is also seen that mechanical state can influence the magnetic state. For magnetostrictive materials, change of stress can cause change of magnetization. This effect is called the magnetomechanical effect. For more information see [22].

2.3.1 Preisach model for magnetostrictive materials

The Preisach model is frequently used for the modeling of magnetostrictive materials. Since magnetostrictive materials have four variables per axis (magnetic field H, magnetization M, stress and strain), different choices for input and output are used for the Preisach model. In [1], a two dimensional Preisach model is used for one-dimensional magnetostriction. Here the

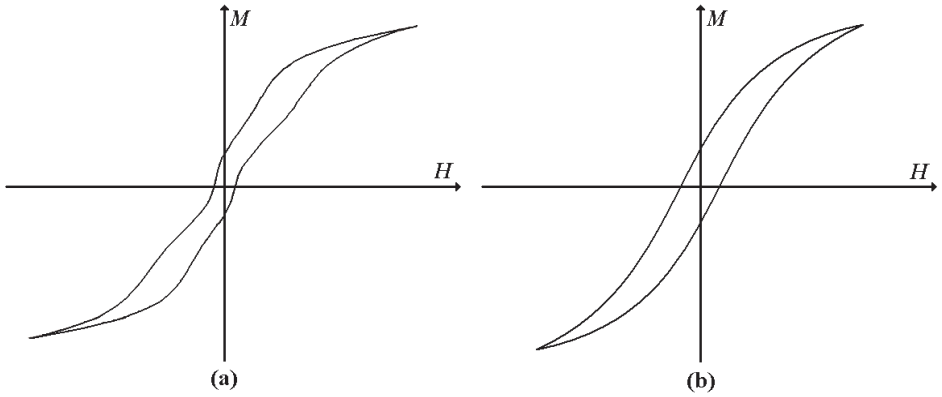

Figure 2-9: (a) Major hysteresis curve of Terfenol-D, (b) major hysteresis curve of a regular magnetic material.

inputs are H field and stress, while the outputs are B field and strain. In [15], M is chosen as the input and strain is chosen as the output. In this article, magnetostriction of soft iron alloys are studied. In [41], the classical choice of H as the input and M as the output is used for modeling Terfenol-D at audio frequencies. In [65], effective magnetic field H and effective stress are defined to extend the Preisach model to magnetostrictive materials. A Preisach model relates the effective magnetic field H to magnetization M and an algebraic relation is used to describe strain as a function of magnetization and stress. In all these articles, the model and experimental data were in a reasonable agreement. This comparison shows that the Preisach model is flexible enough to model the system properly, with different choices of inputs and outputs. The Preisach model can also represent Terfenol-D accurately for a constant stress [58, 62].

In [6], the Preisach model is modified to develop a stress-dependent hysteresis model. An effective magnetic field is defined by combining magnetic field H and stress. This effective magnetic field is the input for a Preisach model which determines the magnetization M. A different effective magnetic field H is used for each dipole. In [56], the Preisach model is used with a set of ordinary differential equations to develop a rate-dependent hysteresis model for magnetostrictive materials.

In [49], a physics based model for magnetostriction is developed. This article is the extension

of [53] to magnetostrictive materials. Here, the system equilibrium points are found by modeling the Helmholtz free energy for each dipole. The developed model is similar to a Preisach model. This model is fully discussed in Subsection 3.2.1.

In [47], the model in [49] is extended to a more accurate load-dependent hysteresis model. For this purpose, the model parameters in [49] are assumed to be functions of the load. Simple algebraic relations are used to represent the model parameters as functions of the load. Experimental data is used to find the coefficients of the algebraic relations.

2.3.2 Other models for magnetostrictive materials

In [44, 13], the Jiles-Atherton model is extended to include the effects of stress. It is suggested that the effects of stress can be represented by an additional magnetic field; that is, equation (2.6) is replaced by the following relation:

$$H_e = H + \bar{\alpha}M + H_\sigma \tag{2.8}$$

where H_σ represents the effects of the stress. In [44], using thermodynamics, H_σ is computed as:

$$H_\sigma = \frac{3}{2}\frac{\sigma}{\mu_0}\frac{\partial\lambda}{\partial M} \tag{2.9}$$

where σ is stress, λ is magnetostriction and μ_0 is a physical constant. In [13], the Jiles-Atherton model with quadratic magnetostriction is used. The law of approach to anhysteretic magnetization is used to model the magnetomechanical effect. This model was evaluated with experimental results from a Terfenol-D sample.

In [25, 26, 40], the Stoner-Wohlfarth model is modified for magnetostrictive materials. In this model, the rotation of non-interacting magnetic domains is the main mechanism. Magnetostriction is introduced by adding an energy term to the domain energy.

In this chapter, hysteresis models in general were reviewed. In the next chapter, load-dependent hysteresis models for magnetostrictive materials are discussed in detail.

Chapter 3

Load dependent hysteresis models for magnetostrictive materials

In the previous chapter, the hysteresis models in general were reviewed. In this chapter, hysteresis models for Terfenol-D in particular, are discussed. The homogenized energy model introduced in the previous chapter is examined in more detail. Since load dependence is one of the main features of Terfenol-D hysteresis, it is thoroughly covered in this chapter. A test rig is used to obtain experimental data under different conditions. The experimental results are used to identify and evaluate the hysteresis models. The test rig is explained in Chapter 5 in detail.

In the first section, the relation between magnetization and elongation for Terfenol-D is studied. Minor loop handling of different hysteresis models are examined in Section 2 for a constant load. In Section 3, load-dependent hysteresis of Terfenol-D is discussed. A new load-dependent model is proposed and compared with an existing load-dependent hysteresis model.

3.1 Magnetostriction of Terfenol-D

For magnetostrictive materials, there is an algebraic relation between magnetization and elongation that is independent of the system history [62, 22]. In modeling, it is usually preferred to compute magnetization M, and then derive the elongation using this relation. In this section,

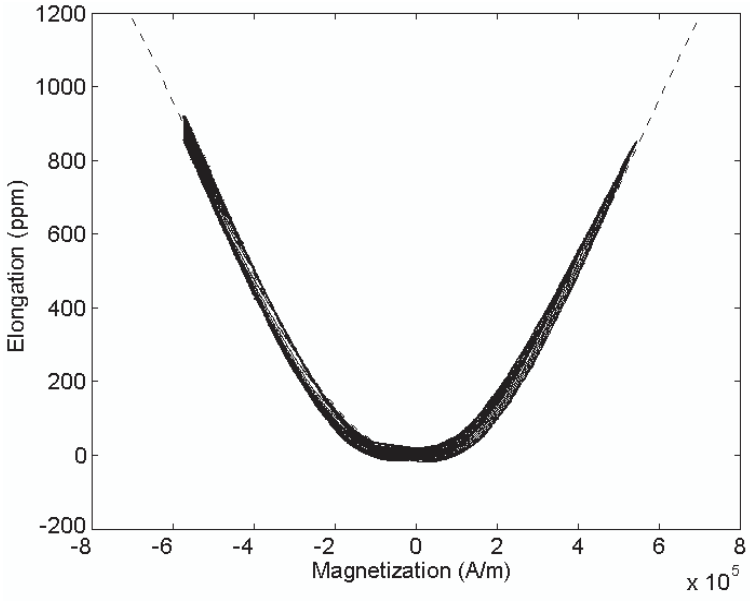

Figure 3-1: Elongation versus magnetization for multiple hysteresis loops for a constant stress (7.18 MPa).

this relation is studied. The relation between magnetic field H and magnetization M is studied in the next sections.

In Figure 3-1, the elongation is plotted versus magnetization for a set of hysteresis loops at a constant stress of 7.18 MPa. Ignoring experimental error, it is seen that the curves coincide. This confirms the existence of an algebraic relation between magnetization and elongation. Since the curves in Figure 3-1 are symmetric about the elongation axis, a polynomial function of even powers of M is proposed [22]:

$$\lambda = \gamma_1(\sigma)M^2 + \gamma_2(\sigma)M^4 + \cdots \tag{3.1}$$

where $\gamma_i(\sigma)$ are functions of stress and λ is the elongation caused by magnetization. Usually, terms higher than M^4 are not used:

$$\lambda(M, \sigma) = \gamma_1(\sigma)M^2 + \gamma_2(\sigma)M^4. \tag{3.2}$$

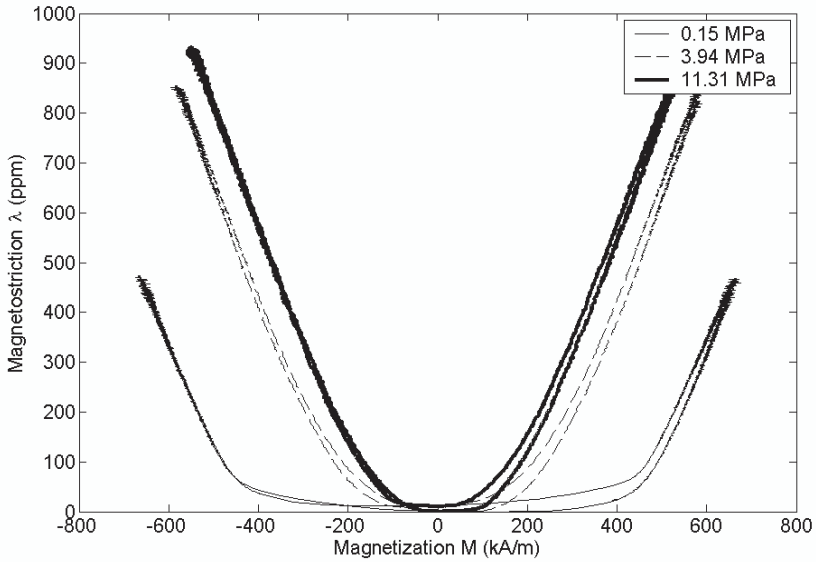

Figure 3-2: Magnetostriction versus magnetization at different loads.

Note that in this equation, only the elongation caused by magnetization is included. For total elongation ε, the mechanical strain $\frac{\sigma}{Y}$ should be added, where σ is the stress and Y is the Young's modulus.

In Figure 3-1, a plot of equation (3.2) is shown with a dashed line. This dashed line mostly lies within the experimental data and cannot be clearly seen, which shows a good agreement between equation (3.2) and the experimental data at this stress.

Figure 3-2 shows the magnetostriction versus magnetization at different loads. It is seen that the shape of curves changes significantly when the stress is changed. The parameters $\gamma_1(\sigma)$ and $\gamma_2(\sigma)$ determine how the curves change when the stress is changed. Consider a linear relationship between $\gamma_i(\sigma)$ and σ:

$$\begin{aligned} \gamma_1(\sigma) &= \gamma_1(0) + \sigma\gamma_1'(0) \\ \gamma_2(\sigma) &= \gamma_2(0) + \sigma\gamma_2'(0) \end{aligned} \tag{3.3}$$

Parameter	$\gamma_1(0)$	$\gamma_1'(0)$	$\gamma_2(0)$	$\gamma_2'(0)$
Unit	$(\frac{\mathrm{m}}{\mathrm{A}})^2$	$(\frac{\mathrm{m}}{\mathrm{A}})^2\,\mathrm{Pa}^{-1}$	$(\frac{\mathrm{m}}{\mathrm{A}})^4$	$(\frac{\mathrm{m}}{\mathrm{A}})^4\,\mathrm{Pa}^{-1}$
Value	2.07e-15	-1.13e-22	-2.23e-27	-2.67e-34

Table 3.1: Magnetostriction parameters for Terfenol-D

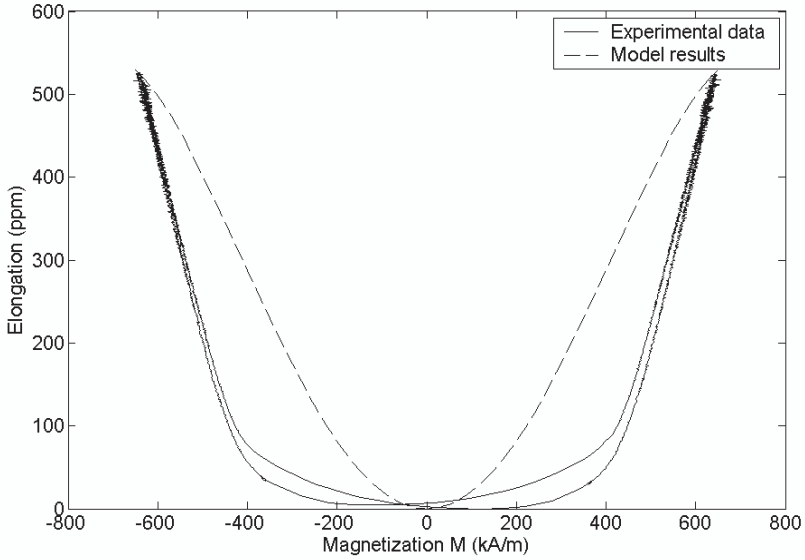

Figure 3-3: Elongation versus magnetization at 0.57 MPa.

The parameters $\gamma_1(0)$, $\gamma_1'(0)$, $\gamma_2(0)$ and $\gamma_2'(0)$ are constants that are determined by experimental data. For the Terfenol-D sample, elongation and magnetization are measured using the experimental setup at 21 different loads from 0.15 MPa to 11.31 MPa. The parameters in equation (3.3) are determined using a least-square fit to the data, minimizing the following error function:

$$J = \sum(\lambda_{ex} - \lambda_m)^2 \tag{3.4}$$

where λ_{ex} is the experimental elongation and λ_m is obtained from equation (3.2). The results are listed in Table 3.1.

In Figures 3-3 and 3-4, experimental data is compared with equations (3.2) and (3.3) for

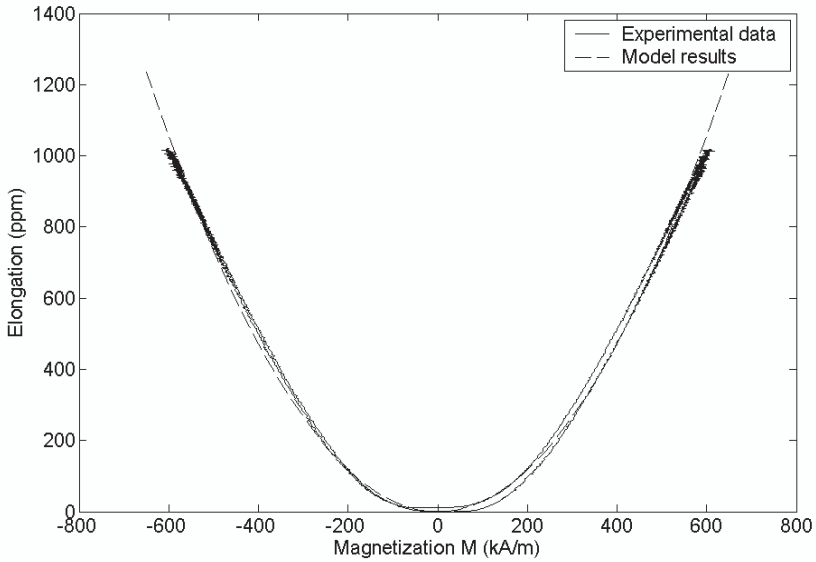

Figure 3-4: Elongation versus magnetization at 7.98 MPa.

the major hysteresis loop. For high stresses (Figure 3-4), a good fit is obtained since the experimental curves are very similar to a parabola. For low stresses (Figure 3-3), there is a considerable discrepancy. The reason is having too few terms in equation (3.2). To improve accuracy, more terms or a different function should be used. See Section 3.3.2.

3.2 Hysteresis models at a constant load

In this section, minor loop handling of different hysteresis models for magnetostrictive materials is examined for a constant load. The Preisach model, the homogenized energy model and the Jiles-Atherton models are used and identified for a Terfenol-D sample in the candidate's master's thesis [57]. In this section, a new experiment is performed and the accuracy of the models in predicting the response of the material is discussed.

The Preisach and Jiles-Atherton models were introduced in the previous chapter. The homogenized energy model includes the effects of strain. Since the homogenized energy model is frequently used in this thesis, it is explained in detail in the following subsection.

3.2.1 Homogenized energy model for magnetostrictive materials

In this model [49], a physical model for magnetostrictive materials is used to develop a hysteresis model similar to the Preisach model that is based on energy considerations. Here, the material is assumed to be composed of a large number of weakly interacting magnetic dipoles. Magnetic dipoles can be an atom or a molecule, having a constant magnetic "strength" like a small magnet. These dipoles can rotate in their place, and the magnetic field of the material is the aggregate of the magnetic fields of the dipoles. When the material is demagnetized, it is believed that these dipoles are oriented randomly so their magnetic fields cancel each other and no macroscopic magnetic field can be seen. When an external magnetic field is induced upon the material, the dipoles rotate in their place and become parallel to the external magnetic field. In that case, even if the external field is removed, a macroscopic magnetic field can be seen. When all dipoles are parallel to each other, the maximum magnetization is obtained and it is said that the material is saturated magnetically.

In this model, the equilibrium states of the dipoles are obtained by using the Helmholtz and Gibbs energies. The Helmholtz free energy ψ and the Gibbs energy G are defined as follows:

$$\psi = U - TS, \tag{3.5}$$

$$G = \psi - \mu_0 HM - \sigma\varepsilon, \tag{3.6}$$

where U is the internal energy, T is the temperature, S is the entropy of the system, μ_0 is a physical constant, σ is the stress, and ε is the strain. The following thermodynamical relations hold for the mentioned energy functions. The first relation is the first law of thermodynamics. The second relation defines the work done on the system and the third relation is the inequality of Clausius [67, page 205]:

$$\frac{dU}{dt} = \frac{dQ}{dt} + \frac{dW}{dt} \tag{3.7}$$

$$\frac{dW}{dt} = \mu_0 H \frac{dM}{dt} + \sigma \frac{d\varepsilon}{dt} \tag{3.8}$$

$$\frac{dS}{dt} \geq \frac{1}{T}\frac{dQ}{dt} \tag{3.9}$$

where Q and W are the amount of heat energy and mechanical/magnetic energy transferred to the system, respectively. For more information about the thermodynamical relations, see [67].

The Helmholtz free energy for a dipole can be computed theoretically [48]. It is a complex equation which is not used in practice. In this model, the Helmholtz free energy is approximated by three parabolas [49] (Figure 3-5):

$$\psi(M,\varepsilon) = \frac{1}{2}Y\varepsilon^2 - Y\gamma_1\varepsilon M^2 + \begin{cases} \frac{\mu_0\eta'}{2}(M+M_R)^2, & M \leq -M_I, \\ \frac{\mu_0\eta'}{2}(M-M_R)^2, & M \geq M_I, \\ \frac{\mu_0\eta'}{2}(M_R-M_I)(M_R-\frac{M^2}{M_I}), & |M| < M_I, \end{cases} \tag{3.10}$$

where the variable M is the magnetization for the dipole, the parameter η' is a constant, γ_1 is the magnetomechanical coupling constant and Y is Young's modulus. The parameter M_R is the remanence magnetization. In the absence of strain ε, ψ is minimized at $\pm M_R$. The parameter M_R is assumed to be the same for all dipoles. The parameter M_I is the inflection point where the second derivative of ψ changes sign. Unlike M_R, because of the nonhomogeneities and imperfections in the material, M_I is different for each dipole. For a valid Helmholtz free energy $M_R > M_I$. This ensures that the Helmholtz free energy has two distinct minima as shown in Figure 3-5.

Define H_0 to be the local magnetic field at a dipole. Because of the imperfections and nonhomogeneities in the material, the local magnetic field H_0 might not be equal to the external magnetic field H. It is assumed that the difference $s = H - H_0$ is constant over time for each dipole.

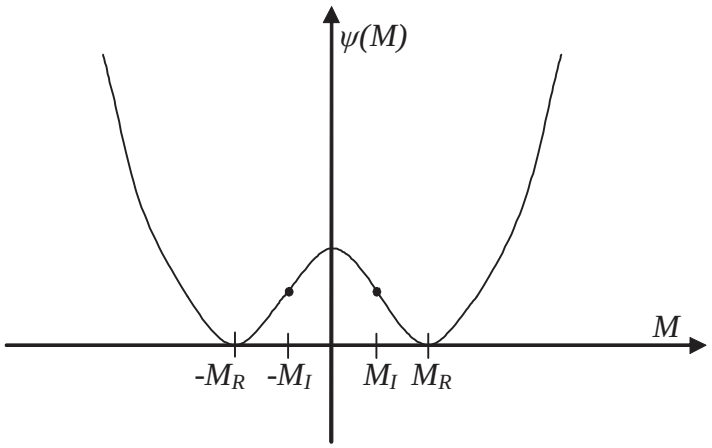

Figure 3-5: The Helmholtz free energy for $\varepsilon = 0$.

The parameters s and M_I describe each dipole. Define:

$$r = \eta'(M_R - M_I) + \frac{2}{\mu_0} Y \gamma_1 \varepsilon M_I. \tag{3.11}$$

It will be shown later that it is easier to use r as defined in equation (3.11) instead of M_I to describe each dipole. This definition of r is consistent with r for a Preisach relay, as shown in Figure 2-2.

For a dipole, the Gibbs energy is:

$$G_{r,s}(H_0, M_{r,s}, \sigma, \varepsilon) = \psi_{r,s}(M_{r,s}) - \mu_0 H_0 M_{r,s} - \sigma\varepsilon \tag{3.12}$$

as shown in Figure 3-6. In this equation, $M_{r,s}$ is the magnetization for the dipole as a function of r and s.

Consider a single dipole in a process in which the temperature, magnetic field H and stress are constant. By combining equations (3.5)-(3.9), we have:

$$\frac{dG_{r,s}}{dt} \leq 0. \tag{3.13}$$

This relation states that during this process, G has to either stay constant or decrease. At a stable equilibrium point, the Gibbs energy is minimized [46, pp. 65 and 184]. In this case, the derivative of Gibbs energy has to be zero with respect to unconstrained variables:

$$\left(\frac{\partial G_{r,s}(H_0, M_{r,s}, \sigma, \varepsilon)}{\partial M_{r,s}}\right)_{T,H_0,\sigma,\varepsilon} = 0, \tag{3.14}$$

$$\left(\frac{\partial G_{r,s}(H_0, M_{r,s}, \sigma, \varepsilon)}{\partial \varepsilon}\right)_{T,H_0,\sigma,M_{r,s}} = 0. \tag{3.15}$$

By combining (3.12) and (3.14), the following relation is obtained:

$$\mu_0 H_0 = \left(\frac{\partial \psi}{\partial M_{r,s}}\right)_{T,\varepsilon}. \tag{3.16}$$

In a magnetic system with many dipoles, the dipole dynamics is very fast. If the magnetic field is not very rapidly changing, the magnetic field appears to be almost constant for each dipole over the time constant of the dipole. The magnetization for a dipole is a minimum of the Gibbs energy.

By combining equations (3.10), (3.12), and (3.16), the equilibrium magnetization for a dipole is obtained:

$$M^*_{r,s} = \frac{H - s + R_{r,s}\eta' M_R}{\eta' - \frac{2Y\gamma_1\varepsilon}{\mu_0}}. \tag{3.17}$$

If the dipole is in the left minimum in Figure 3-6(a), $R_{r,s} = -1$, and if the dipole is in the right minimum, $R_{r,s} = +1$.

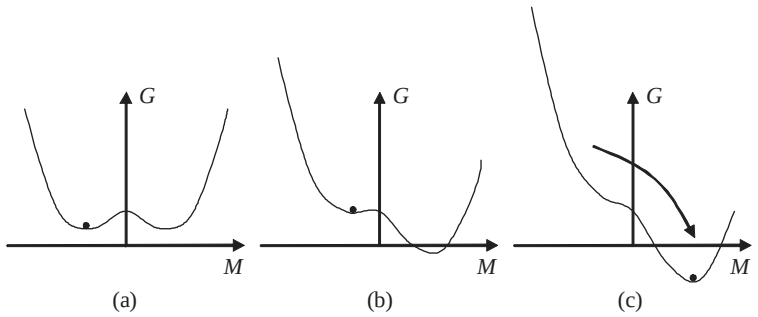

Figure 3-6: For a constant ε: (a): Gibbs energy when $H_0 = 0$, (b): Gibbs energy for a positive H_0, (c) if H_0 is further increased, at some point, only one minimum exists.

As seen in Figure 3-6(a), if $H_0 = 0$, two minima exist. For a small positive H_0 as shown in Figure 3-6(b), still two minima exist, but if H_0 is further increased, at some point, one disappears as shown in Figure 3-6(c). At this time, dipole magnetization moves to the new minimum. This transition is shown with an arrow in Figure 3-6(c).

Using equation (3.11), it can be shown that if $H \geq s + r$, the $R = -1$ minimum does not exist. Similarly, for $H \leq s - r$, the $R = +1$ minimum vanishes. For $s - r < H < s + r$, two minima exist, which means that both $R = -1$ and $R = +1$ are possible. Similarly, for the Preisach relay introduced in Figure 2-2, the output -1 is nonexistent if $H \geq s + r$, and $+1$ vanishes if $H \leq s - r$. For the values between $s - r$ and $s + r$, both outputs are possible.

With a distribution $\mu(r, s)$ for the dipoles, the overall magnetization can be obtained:

$$M_{Tot} = C \int_0^\infty \int_{-\infty}^\infty M^*_{r,s} \mu(r, s) ds dr. \tag{3.18}$$

Define $\mathcal{I}_n$ to be

$$\mathcal{I}_n = \int_0^\infty \int_{-\infty}^\infty s^n \mu(r, s) ds dr, \tag{3.19}$$

where $n = 0$, 1, or 2. Using (3.17), M_{Tot} can be rewritten:

$$M_{Tot} = \frac{C}{\eta' - \frac{2Y\gamma_1\varepsilon}{\mu_0}} \left[\mathcal{I}_0(H - M_R\eta') - \mathcal{I}_1 + 2M_R\eta' \int_0^{\infty} \int_{-\infty}^{\tau(t,r)} \mu(r,s) ds dr \right], \tag{3.20}$$

where C is a constant and $\tau(t,r)$ is the Preisach boundary for the relay configuration $R_{r,s}$. Experimental data is used to find the optimum weight function $\mu(r,s)$. A few common choices for the form of $\mu(r,s)$ can be found in [47, 51, 62].

Unlike the classic Preisach model, magnetization in this model depends on strain ε. In this model, stress σ and magnetic field H are the inputs. The Preisach plane boundary $\tau(t,r)$ and strain ε are the system state. The outputs are strain ε and magnetization M. The magnetization is determined by (3.20). Combining (3.10), (3.12), and (3.15), we obtain the strain:

$$\varepsilon = \frac{\sigma}{Y} + \gamma_1 M^2. \tag{3.21}$$

In this equation, $\frac{\sigma}{Y}$ is the strain caused by the stiffness of the material and $\gamma_1 M^2$ is the strain caused by magnetization. This equation is similar to equation (3.2) with $\gamma_2 = 0$.

As stated before, for a dipole with $s - r < H < s + r$, two equilibrium states are possible. In the presented model, a transition between these states cannot happen unless the magnetic field is changed. In general, such transitions may be possible due to thermal fluctuations. For example, the dipole shown in Figure 3-6(b) can have a transition to the right state if the thermal fluctuations are large enough. Such "thermal relaxations" can cause a change in the output even if the input is constant. Since such behaviour is not visible in the experimental data for Terfenol-D, this effect is not discussed here. For more information see [9].

The Preisach and homogenized energy models have similar structures. As a result, these models have many similar properties. Unlike the Preisach model, the homogenized energy model is physics based. Some features of the hysteresis such as temperature and load dependence and thermal relaxations are seen in the homogenized energy model because of its physical basis.

3.2.2 Models comparison

To evaluate and compare the hysteresis models for Terfenol-D, two sets of experimental data are obtained. The first set is used to identify the model parameters for the Preisach model, the homogenized energy model explained in the previous subsection, and the Jiles-Atherton model [57]. The second set is used to evaluate and compare the models.

Minor loops have a special importance in control applications. In a typical control system, usually the major loop is not experienced, and frequently the input is oscillating about an operating point. In this case, a minor loop is experienced. If the oscillation amplitude decays with time, complex nested loops may be produced. For this reason, it is important to have a hysteresis model capable of handling complex minor loops for control applications.

For the second experiment, in the beginning, the system input, magnetic field H, oscillates between negative and positive saturation values. The amplitude of the input is decreased gradually and finally the input settles down to zero. This input generates a few nested minor loops. In Figure 3-7, flux density B is plotted versus the magnetic field H for this experiment.

To produce hysteresis curves with the Preisach model, a general weight function is used. The weight function $\mu(r, s)$ in equation (2.1) is a piecewise-constant function over the Preisach plane. The Preisach plane is subdivided into 820 square-shaped regions. The weight function $\mu(r, s)$ is constant in each region. The weight function is identified using an equation which relates the weight in each region to the experimental data [57]. For weight function identification, the first set of experimental data is used.

Figure 3-8 shows the Preisach model output for the same input as the second experiment. It is seen that the experimental data and model results are very similar, which shows the accuracy of the Preisach model prediction. The special curvature of Terfenol-D hysteresis curve is completely captured and reproduced. The major loops of the first and second experimental data sets are not identical. Small variation of experimental parameters such as temperature, etc. is likely the reason for this difference. This is believed to be the main source of error.

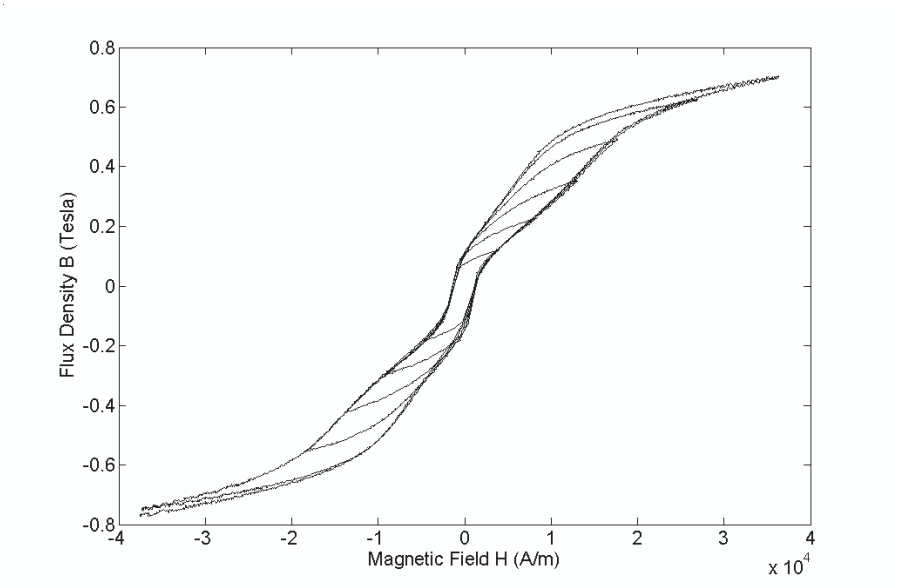

Figure 3-7: Hysteresis curves of the second experiment.

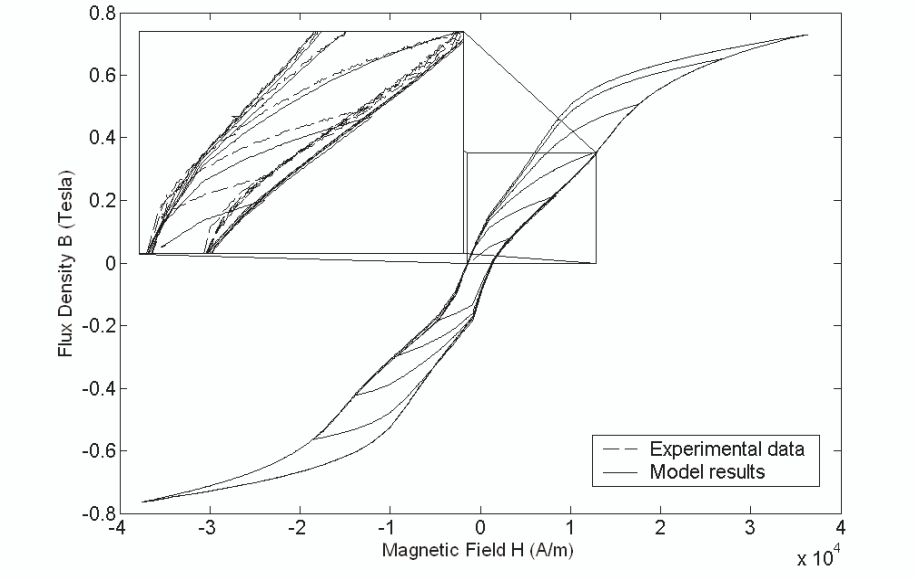

Figure 3-8: The Preisach model results.

Parameter	Gaussian distribution, equation (3.22)	Log-normal distribution, equation (3.23)
η'	17.766	0.47537
b	$1.1591 \times 10^9 \left(\frac{\mathrm{A}}{\mathrm{m}}\right)^2$	10.837
$\bar{b}$	$2.2540 \times 10^8 \left(\frac{\mathrm{A}}{\mathrm{m}}\right)^2$	$1.4567 \times 10^8 \left(\frac{\mathrm{A}}{\mathrm{m}}\right)^2$
$\bar{H}_c$	$-136030\frac{\mathrm{A}}{\mathrm{m}}$	$0.81725\frac{\mathrm{A}}{\mathrm{m}}$
M_R	$7417.7\frac{\mathrm{A}}{\mathrm{m}}$	$8.0029 \times 10^5 \frac{\mathrm{A}}{\mathrm{m}}$
C	$2.0996(\frac{\mathrm{m}}{\mathrm{A}})^2$	$5.5034 \times 10^{-7}(\frac{\mathrm{m}}{\mathrm{A}})^2$

Table 3.2: Model parameters for the homogenized energy model

Before the homogenized energy model can be used, a class of weight functions $\mu(r, s)$ should be chosen. In this thesis, the following weight functions are used:

$$\text{Gaussian:} \qquad \mu(r,s) = \exp\left(-\frac{(r-\bar{H}_c)^2}{b}\right)\exp\left(-\frac{s^2}{\bar{b}}\right), \tag{3.22}$$

$$\text{Log-normal:} \qquad \mu(r,s) = \exp\left(-\frac{\left(\ln\left(\frac{r}{\bar{H}_c}\right)\right)^2}{b}\right)\exp\left(-\frac{s^2}{\bar{b}}\right), \tag{3.23}$$

where b, $\bar{b}$, and $\bar{H}_c$ are constants. A general weight function can also be used for this model [51], which gives model results similar to that of the classic Preisach model.

Root-mean-square error was computed as follows: For each value of magnetic field H, error is computed by subtracting model results from experimental data. Total model error is computed by taking the root-mean-square of these errors.

As detailed in [57], for the Terfenol-D experimental data, the best model parameters are found by numerically minimizing the root-mean-square error using Nelder-Mead simplex direct search method for the first set of experimental data. Other methods can also be used [50]. The optimum values are in Table 3.2.

Figures 3-9 and 3-10 compare the model results and the second set of experimental data for a Gaussian distribution. It is seen that the model and experimental data are close, but the curvature in the middle is not accurately captured. In Figure 3-11, the model results and

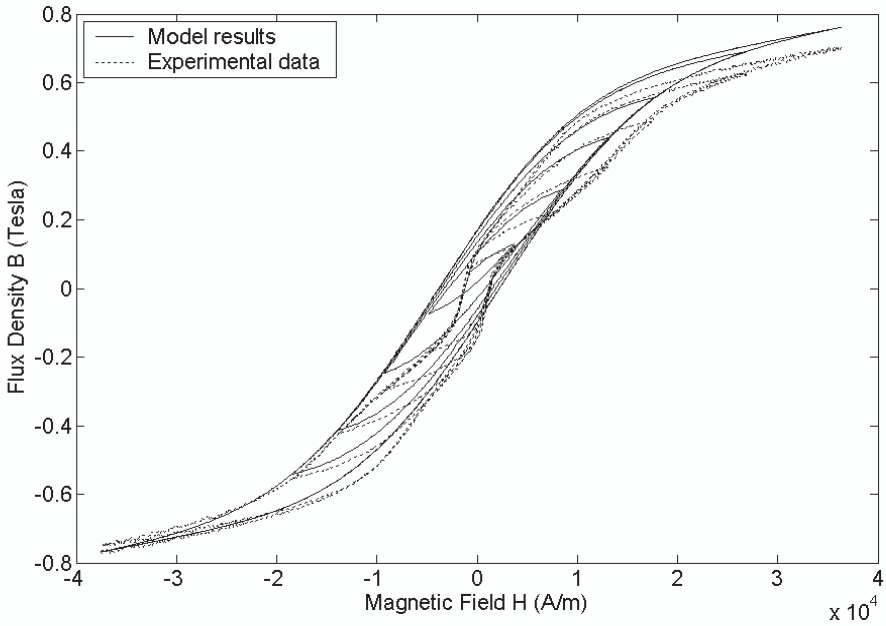

Figure 3-9: The experimental data and the homogenized energy model results with Gaussian distribution, equation (3.22).

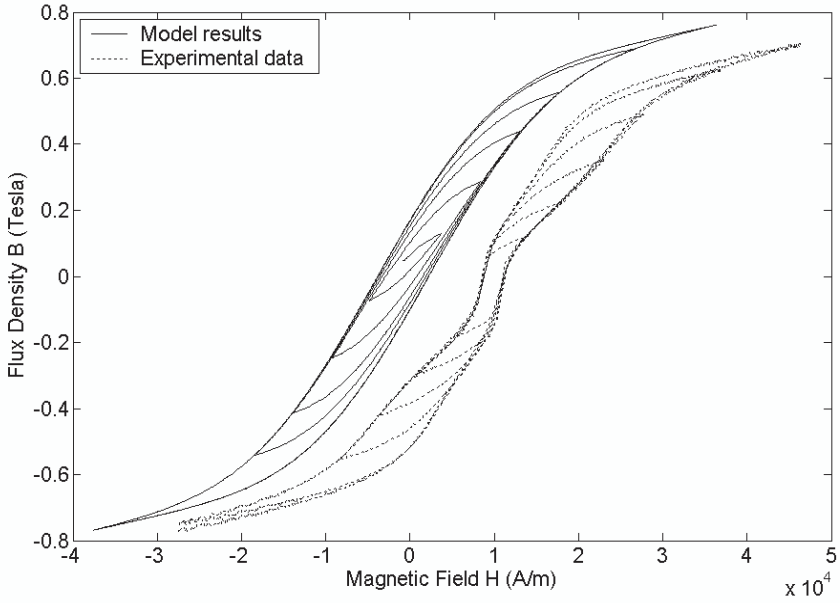

Figure 3-10: The experimental data and the homogenized energy model results with Gaussian distribution. The experimental results are shifted for easier comparison.

experimental data are compared for a log normal distribution. The result for a log normal distribution is very similar to that of the Gaussian distribution.

The Jiles-Atherton model was implemented and identified in the candidate's MS program [57]. By minimizing the root-mean-square error for the first set of experimental data, the optimum model parameters were found. The parameters are listed in Table 3.3.

The second set of experimental data and model results are compared in Figures 3-12 and 3-13. Similar to the homogenized energy model, it is seen that the model is close to experimental

Parameter	Unit	Value
$\bar{\alpha}$	1	1.9903×10^{-8}
a	$\frac{\mathrm{A}}{\mathrm{m}}$	6200.2
M_s	$\frac{\mathrm{A}}{\mathrm{m}}$	690380
k	$\frac{\mathrm{A}}{\mathrm{m}}$	2476.6
c	1	5.7080×10^{-4}

Table 3.3: Model parameters for the Jiles-Atherton model

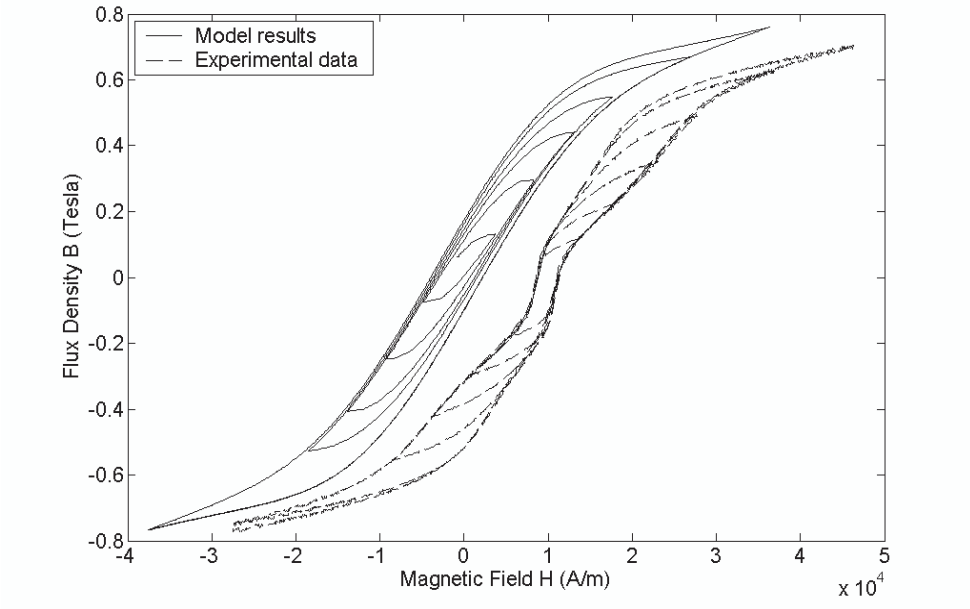

Figure 3-11: The experimental data and the homogenized energy model results with a log-normal distribution. The experimental results are shifted for easier comparison. The results are similar to that of the Gaussian distribution.

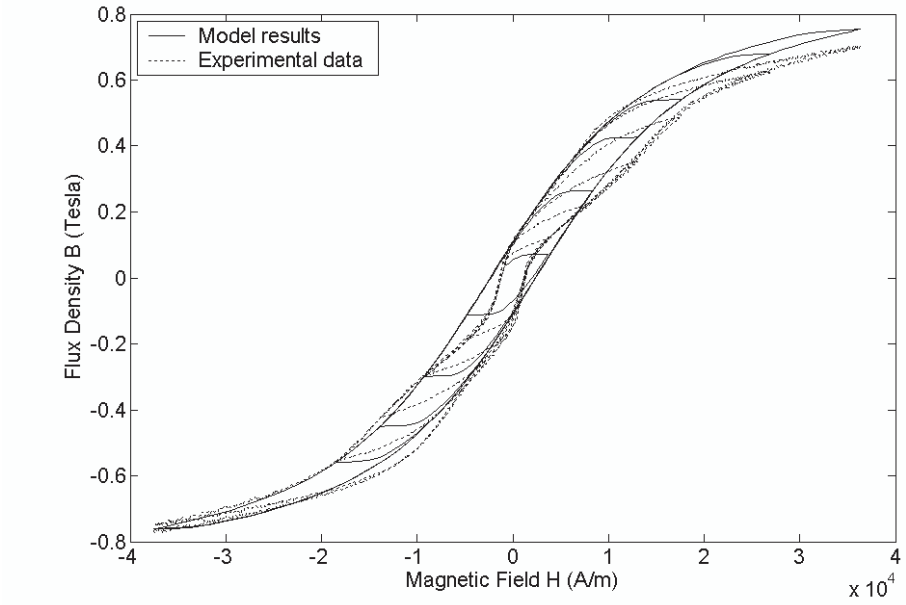

Figure 3-12: The experimental data and the Jiles-Atherton model results. The model was unable to reproduce the middle of the curve correctly.

data, but the twisted section of the experimental data is not captured.

The Preisach model could reproduce the experimental data with least error. The homogenized energy and Jiles-Atherton models had about the same accuracy; and could not capture the twisted section in the middle part of the hysteresis curve.

The Preisach and homogenized energy models can handle minor loops properly. The minor loop handling for the Jiles-Atherton model is not done correctly for control applications [48]. If Figures 3-8, 3-10, 3-11, and 3-13 are compared, it is seen that the minor loops for the Jiles-Atherton model join the major loop faster than the experimental data. In contrast, for the homogenized energy model, the minor loops join the major loop much slower than the experimental data. It can be said that the Jiles-Atherton model underestimates the amount of input variation required to forget past history and the homogenized energy model overestimates this amount. The Preisach model is the most accurate in this matter.

In Table 3.4, the model comparison is summarized. Fitting error is the best error found

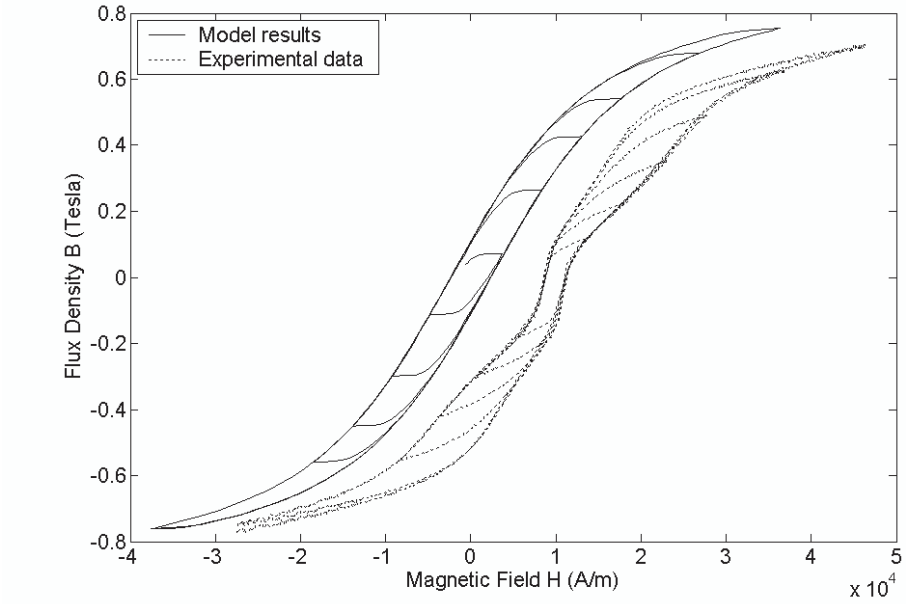

Figure 3-13: The experimental data and the Jiles-Atherton model results. The experimental results are shifted for easier comparison.

Parameter	The classic Preisach model	The homogenized energy model (Gaussian), eq. (3.22)	The homogenized energy model (log normal), eq. (3.23)	The Jiles-Atherton model
Fitting error (Tesla)	0	0.0356	0.0322	0.0254
Prediction error (Tesla)	0.0172	0.0569	0.0562	0.0426
No. of model parameters	820	6	6	5
Minor loop handling	$\surd$	$\surd$	$\surd$	$\times$

Table 3.4: Models comparison

during the model identification process for the first set of experimental data and prediction error is the accuracy of the predicted output for the second experiment.

The Preisach model has 820 parameters to describe the material. This number is six for the homogenized energy model and five for the Jiles-Atherton model. The accuracy of the Preisach model with a general weight function is partially due to the large number of parameters. Where high accuracy is crucial, a general weight function should be used. The Jiles-Atherton model and homogenized energy model had similar accuracy and required similar number of parameters. However, the Jiles-Atherton model does not handle minor loops properly. Furthermore, its use requires solving coupled nonlinear differential equations and is considered more computationally intensive than the Preisach or homogenized energy models. The homogenized energy model is preferable to Jiles-Atherton. Also, a general weight function can be used for the homogenized energy model [51] at the expense of higher number of parameters. In this case, the classic Preisach model and the homogenized energy model will have similar accuracies.

3.3 Load-dependent hysteresis models for magnetostrictive materials

For magnetostrictive materials, the shape of the hysteresis curve changes significantly if the load is changed. In Figure 3-14, the hysteresis curves of Terfenol-D are shown for different stresses. It is seen that for low loads, the hysteresis curve is very thin with a high slope in the middle. As the stress is increased, the hysteresis curve becomes thicker with less slope in the middle. For high stresses, an additional curvature is seen in the middle portion of the hysteresis curve. This new curvature is not visible for low loads. It is believed that this curvature is caused by the fact that the dipoles have more than two equilibrium states [3, 26].

The models mentioned in the previous section can represent the material accurately only for a constant load. Since the hysteresis curves are highly load-dependent, if the material is subjected to a variable load, a load-dependent hysteresis model is needed.

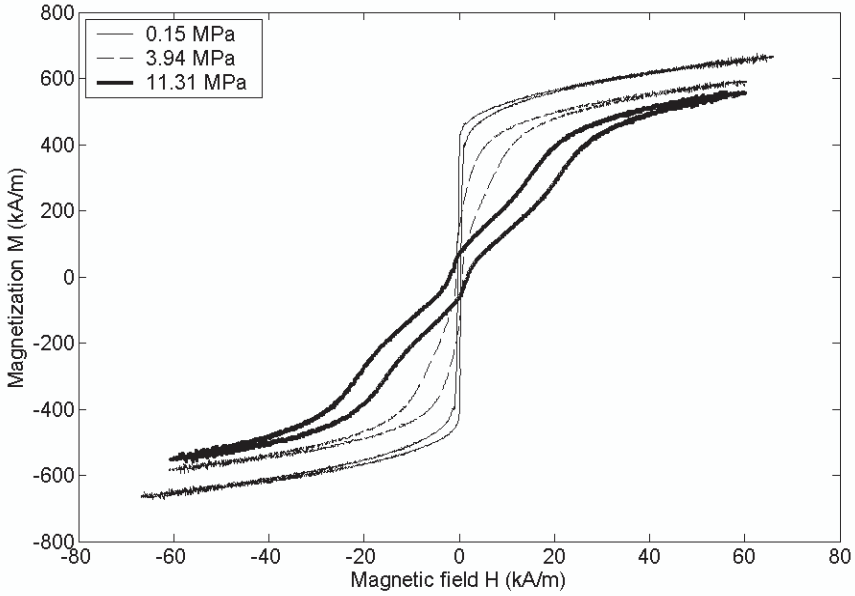

Figure 3-14: Hysteresis curves for different loads.

To incorporate the effects of load, the hysteresis models are extended. In this section, it is explained how the homogenized energy model can be modified to include load-dependence [47]. A new load-dependent hysteresis model is also developed by using a classic Preisach model with a general weight function.

3.3.1 Load-dependent homogenized energy model

In this subsection, the model discussed in Subsection 3.2.1 is extended to include better load-dependence [47].

By comparing equations (3.2) and (3.21), it is seen that for the hysteresis model in Subsection 3.2.1, $\gamma_2(\sigma) = 0$. To obtain a more accurate relation for the magnetostriction, the Gibbs energy given in equation (3.12) is modified as follows:

$$G(H_0, M, \sigma, \varepsilon) = \psi(M, \varepsilon) + \gamma_4 M^4 - \gamma_2(\sigma) Y \varepsilon M^4 - \mu_0 H_0 M - \sigma\varepsilon, \tag{3.24}$$

where $\psi(M, \varepsilon)$ is as defined in equation (3.10). The parameter γ_4 is a constant, Y is the Young's modulus at a constant magnetization, ε is strain, and σ is stress.

By combining equations (3.15) and (3.24), the following relation is obtained to replace equation (3.21):

$$\varepsilon = \frac{\sigma}{Y} + \gamma_1(\sigma)M^2 + \gamma_2(\sigma)M^4. \tag{3.25}$$

Both terms in equation (3.2) are included.

The new terms added to the Gibbs energy provide more accuracy, but the general shape of the Gibbs energy shown in Figure 3-6 still applies. Similar to Subsection 3.2.1, for no magnetic field, two distinct minima exist. For a small positive magnetic field, still two minima exist. At some point, one of the minima disappears and there is only one possible state for the dipole. The smallest magnetic field at which, only one stable equilibrium point exists is called the coercive force H_c which is similar to variable r for a Preisach relay (Figure 2-2).

By combining equations (3.14) and (3.24), the following relation is obtained for magnetization.

$$\left[4\gamma_4 - 4\gamma_2(\sigma)Y\varepsilon\right]M^3 + \left[\mu_0\eta' - 2\gamma_1(\sigma)Y\varepsilon\right]M + \left[-\mu_0 H_0 - \mu_0 R\eta' M_R\right] = 0 \tag{3.26}$$

where $R = +1$ denotes the right minimum in Figure 3-6 and $R = -1$ denotes the left one. By using equation (3.25), the strain ε can be eliminated.

$$\begin{aligned}&\left[-4\gamma_2^2 Y\right]M^7 + \left[-6\gamma_1\gamma_2 Y\right]M^5 + \left[4\left(\gamma_4 - \gamma_2\sigma\right) - 2\gamma_1^2 Y\right]M^3 + \\ &\left[\mu_0\eta' - 2\gamma_1\sigma\right]M + \left[-\mu_0\left(H_0 + R\eta' M_R\right)\right] = 0\end{aligned} \tag{3.27}$$

For a given stress σ, equation (3.27) can be used to find the magnetization. For each value of R, this equation gives seven solutions. Six of these solutions are either imaginary or not physical because they are too large.

The remaining solution is sometimes inadmissible; for example for $R = +1$, if the solution is in the middle or left section of Figure 3-5, it is not a valid solution. If the solution is valid, it is the location of the appropriate minimum in Figure 3-6. If $|H_0| < H_c$, there is one solution for $R = +1$ and one solution for $R = -1$. For $H_0 \geq H_c$, only one solution for $R = +1$ exists and for $H_0 \leq -H_c$, $R = -1$ gives the only solution.

As for the analysis in Subsection 3.2.1, because of the nonhomogeneities and imperfections in the material, the local magnetic field H_0 is not equal to the external magnetic field H. Define the interaction field to be $H_I = H_0 - H$. The interaction field is similar to variable s for a Preisach relay. It is assumed that the dipoles have the same η' and M_R but different values for H_c and H_I. If H_c is known, M_I can be computed. The variable r for a Preisach relay is similar to H_c.

Similar to equation (3.18), by assuming a distribution for H_I and H_c, the overall magnetization can be computed:

$$M_{Tot} = \frac{C}{I} \int_0^\infty \int_{-\infty}^\infty M_{H_c,H_I} \mu(H_c, H_I) dH_I dH_c \tag{3.28}$$

where M_{H_c,H_I} is obtained from equation (3.27). Parameter I is included to normalize the distribution:

$$I = \int_0^\infty \int_{-\infty}^\infty \mu(H_c, H_I) dH_I dH_c \tag{3.29}$$

For the distribution $\mu(H_c, H_I)$, a log-normal distribution similar to equation (3.23) is used [47]:

$$\mu(H_c, H_I) = \exp\left[-\left(\frac{\ln\left(\frac{H_c}{\bar{H}_c(\sigma)}\right)}{2c} \right)^2 \right] \exp\left[-\frac{H_I^2}{2b^2(\sigma)} \right] \tag{3.30}$$

where c is a constant and $b^2(\sigma)$ and $\bar{H}_c(\sigma)$ are functions of stress. The parameter $\bar{H}_c(\sigma)$ determines the mode for the coercive force distribution. For a constant stress

Parameter	Unit	The original model	The new modified model
γ_4	$\left(\frac{\mathrm{m}}{\mathrm{A}}\right)^4 \mathrm{Pa}$	1.29×10^{-17}	4.06×10^{-18}
η'	1	0.621	0.135
M_R	$\frac{\mathrm{kA}}{\mathrm{m}}$	216	489
$\hat{H}_c$	$\frac{\mathrm{A}}{\mathrm{m}}$	12.7	12.6
k_1	Pa^{-1}	1.81×10^{-7}	1.86×10^{-7}
c	1	1.20	1.21
C	1	4.12	2.97
b_0	$\left(\frac{\mathrm{A}}{\mathrm{m}}\right)^2$	1.34×10^6	8.71
b_1	$\left(\frac{\mathrm{A}}{\mathrm{m}}\right)^2 \mathrm{Pa}^{-1}$	3.96	-3.23×10^{-6}
b_2	$\left(\frac{\mathrm{A}}{\mathrm{m}}\right)^2 \mathrm{Pa}^{-2}$	2.82×10^{-6}	-3.59×10^{-13}
b_3	$\left(\frac{\mathrm{A}}{\mathrm{m}}\right)^2 \mathrm{Pa}^{-3}$	-2.32×10^{-14}	-1.43×10^{-20}
RMS error	$\frac{\mathrm{kA}}{\mathrm{m}}$	26.0 or 4.72%	23.1 or 4.20%

Table 3.5: The load-dependent homogenized energy model parameters

$$\bar{H}_c(\sigma) = \hat{H}_c e^{-k_1 \sigma} \tag{3.31}$$

where $\hat{H}_c$ and k_1 are constants. The function $b^2(\sigma)$ is the variance for the interaction field distribution. A polynomial is used for this function.

$$b^2(\sigma) = b_0 + b_1\sigma + b_2\sigma^2 + b_3\sigma^3 \tag{3.32}$$

The parameters b_0, b_1, b_2, and b_3 are constants that are chosen to fit the data.

This model is computationally intense if not implemented correctly. Different techniques for efficient programming, such as lookup tables, should be used. For a detailed discussion of efficient implementation techniques for this model, see [8].

The model parameters are listed in Table 3.5. To find them, experimental data is used. The hysteresis curves of Terfenol-D were obtained for 21 loads from 0.15 MPa to 11.31 MPa. Model parameters are determined by a nonlinear least-square method minimizing the cost function

$$J = \sum (M_{ex} - M_{sim})^2 \tag{3.33}$$

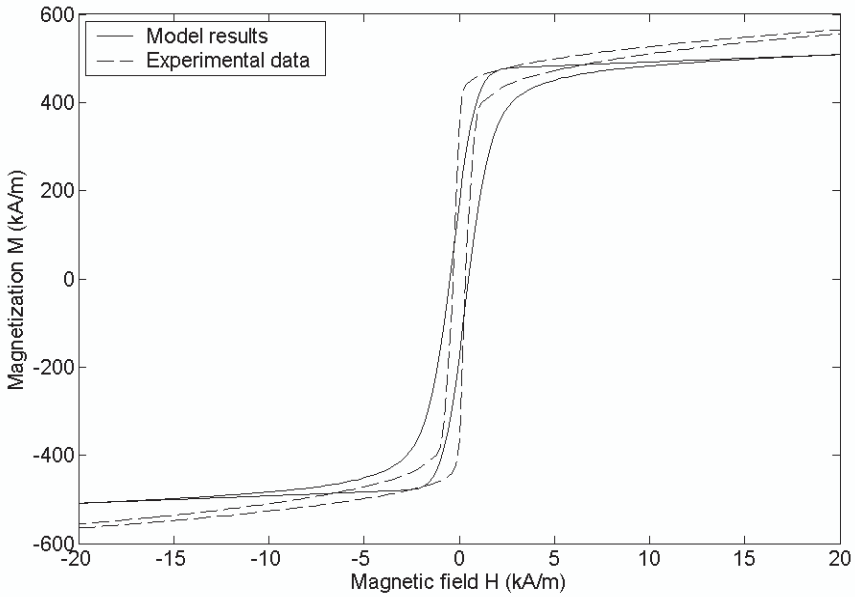

Figure 3-15: Modeled and experimental hysteresis curves for 0.15 MPa.

where M_{ex} is the magnetization from experimental data and M_{sim} is the simulated magnetization from the model. The summation is done over all data points. The results are shown in Table 3.5.

The modeled hysteresis curves are compared against the experimental data in Figures 3-15 and 3-16. The largest error is seen in Figure 3-15. The root-mean-square error is $53.9\frac{\text{kA}}{\text{m}}$ or 10% of the saturation magnetization. It is seen that the slope of the middle section is not reproduced correctly. The least error is seen in Figure 3-16; with an RMS error of $11.7\frac{\text{kA}}{\text{m}}$ or 2%. A very good agreement between the model and experimental results is seen. The average RMS error over all stresses is $26\frac{\text{kA}}{\text{m}}$ or 4.7%.

It is seen that for low stresses, the slope of the middle section is not reproduced correctly. This slope is controlled by the variance of the interaction field, $b^2(\sigma)$. To investigate this, a plot of the optimum value for $b^2(\sigma)$ is shown in Figure 3-17. These optimum values are obtained by performing numerical optimization on each load separately. For each load, all of the model parameters except $b^2(\sigma)$ are held constant and the optimum value of $b^2(\sigma)$ is found for each

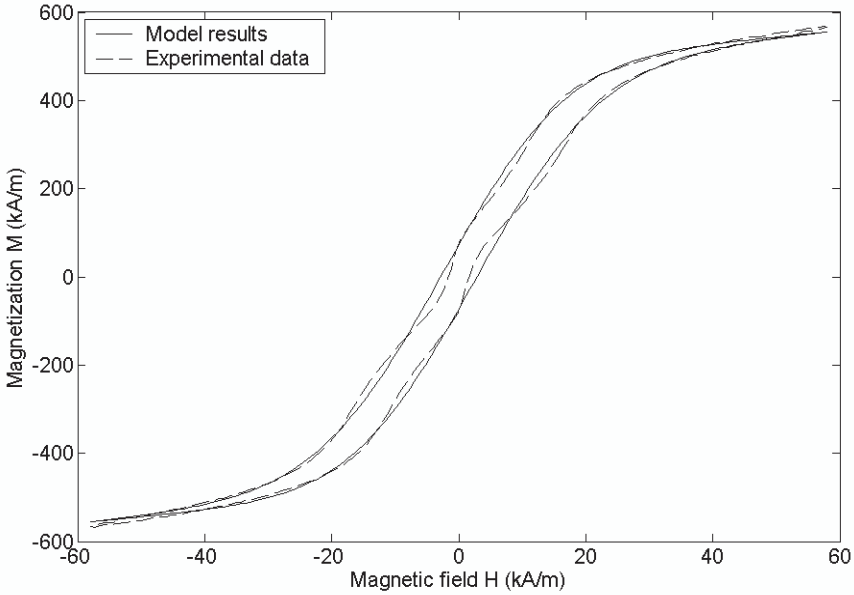

Figure 3-16: Modeled and experimental hysteresis curves for 9.07 MPa.

value of σ.

It is seen that for high compressive stresses, the data and original model agree closely. For lower stresses, the model deviates from optimum experimental values. To improve the model accuracy, the following new relation is proposed to replace equation (3.32):

$$b^2(\sigma) = \exp(b_0 + b_1\sigma + b_2\sigma^2 + b_3\sigma^3). \tag{3.34}$$

The simulation is repeated with the new modified model. The results are included in Table 3.5. The modified model is also shown in Figure 3-17. It is seen that this model follows experimental data more closely than the original model. As a result, the overall RMS error is reduced to $23.1\frac{\text{kA}}{\text{m}}$ or 4.2% from 4.7%.

In Figures 3-18 and 3-19, the hysteresis curves of the original model and the new modified model are compared. It is seen although the slope of the middle portion is not modeled accurately by the original model; the modified model provides better accuracy than that with the

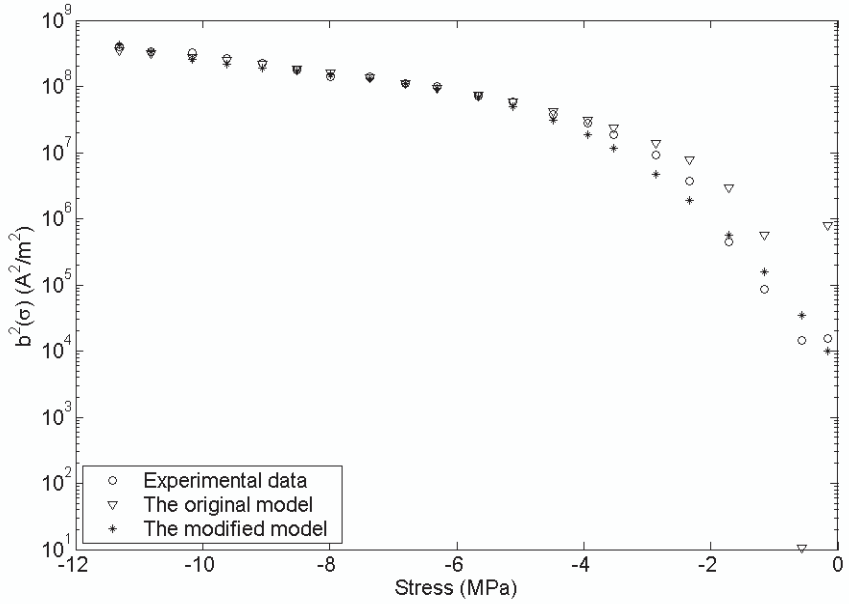

Figure 3-17: Model comparison for the variance of the interaction field.

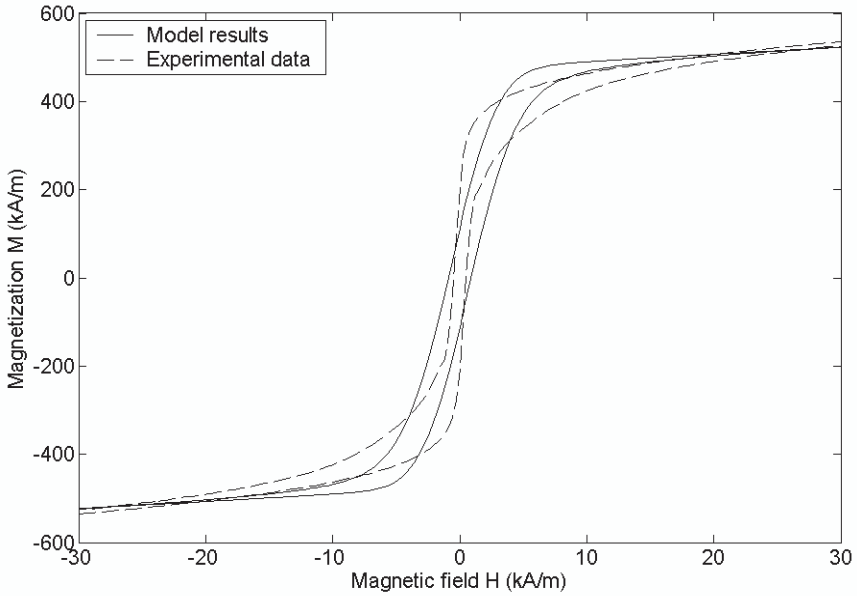

Figure 3-18: Hysteresis curves for 2.33 MPa for the original model.

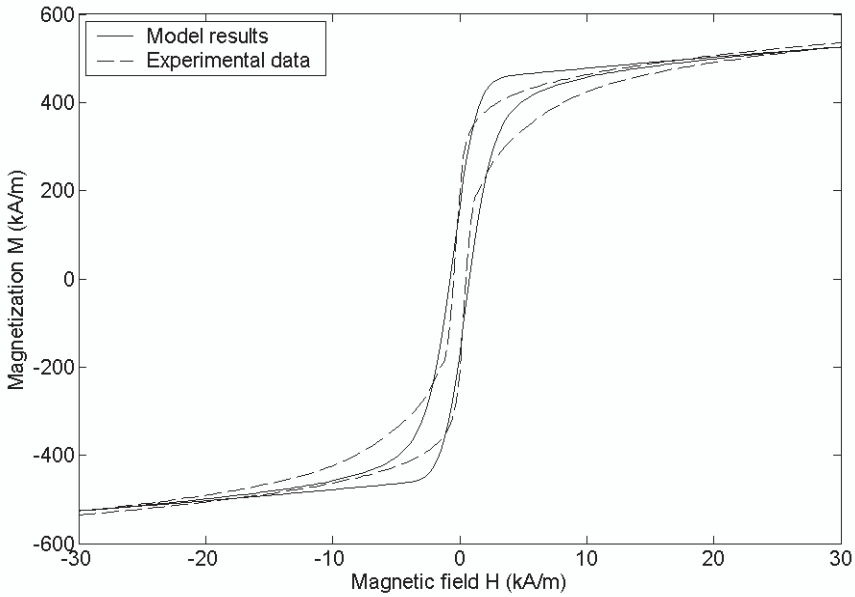

Figure 3-19: Hysteresis curves for 2.33 MPa for the modified model.

original form of $b^2(\sigma)$. For this stress, the RMS errors for the original and modified models are $37.5\frac{\text{kA}}{\text{m}}$ and $28.2\frac{\text{kA}}{\text{m}}$, respectively. The new modified model is 25% more accurate. For higher stresses, the models provide similar results. Note neither model correctly reproduces the twisted portion in the middle of the hysteresis curve.

3.3.2 Load-dependent Preisach model with a general weight function

In the previous subsection, it was noted that the twisted portion in the middle of the hysteresis curve was not reproduced. In Subsection 3.2.2, it was observed that only the model with a general weight function captures and reproduces the curvature. In this subsection, a general weight function is used to develop a new load-dependent model with improved accuracy.

The new model is constructed by analyzing the flow of energy for this system [59]. Suppose that a magnetostrictive sample undergoes a process in which the magnetization is changed by a rate $\dot{M}$. The magnetic power supplied to the material per unit volume is $\mu_0 H\dot{M}$. During this

process, some elongation is seen because of magnetostriction. The mechanical power generated by the material per unit volume is $-\sigma\dot{\varepsilon}$ where σ and ε are the stress and strain, respectively. The difference between the power supplied to the material and the power generated by the material is the amount of energy stored or dissipated as heat in the system.

In Figure 3-14, hysteresis curves at different stresses are shown. Consider a process in which, the magnetization is increased from zero to some value M_0. For a low stress, the magnetic field H is very small. As a result the magnetic power supplied to the system will be small. At the same time, since the stress σ is close to zero, the amount of work done by the system is also small. For a high compressive stress, σ is a large negative number. Unlike the previous case, H is large and considerable magnetic power is sent to the system. At the same time, considerable mechanical power is generated by the system since $-\sigma$ is large. It is suggested that the difference, the power stored or dissipated, has the same value for high and low stresses. This assumption will be verified later.

If the power stored or dissipated is denoted by P_d, we have:

$$P_d = \mu_0 H\dot{M} + \sigma\dot{\varepsilon}. \tag{3.35}$$

Similar to equations (3.21) and (3.25), the strain can be obtained by adding the mechanical and magnetostrictive parts:

$$\varepsilon = \frac{\sigma}{Y} + \lambda(M, \sigma). \tag{3.36}$$

If the stress is constant, $\dot{\varepsilon}$ can be obtained by differentiating both sides of the equation:

$$\dot{\varepsilon} = \frac{\partial\lambda(M,\sigma)}{\partial M}\dot{M}. \tag{3.37}$$

By combining equations (3.35) and (3.37), the following relation is obtained:

$$P_d = \left(\mu_0 H + \sigma \frac{\partial \lambda}{\partial M}\right) \dot{M}. \tag{3.38}$$

The power stored/dissipated is linearly proportional to $\dot{M}$. The quantity $\frac{P_d}{\mu_0 \dot{M}}$ has the same units as a magnetic field. Define:

$$H_d \equiv \frac{P_d}{\mu_0 \dot{M}} = H + \frac{\sigma}{\mu_0} \frac{\partial \lambda}{\partial M}. \tag{3.39}$$

The parameter H_d has magnetic field units, but does not represent a real magnetic field. This parameter represents the power stored/dissipated in the system. In Figure 3-20, a plot of magnetization versus H_d is shown for a few stresses. It is seen that compared to Figure 3-14, the hysteresis curves are more similar. This confirms the assumption of having the same stored/dissipated power for different stresses. It is suggested that the magnetic field H is replaced by H_d for modeling. Define H_σ to be

$$H_\sigma = H_d - H = \frac{\sigma}{\mu_0} \frac{\partial \lambda}{\partial M}. \tag{3.40}$$

In Subsection 2.3.2, it was stated that the load dependence for the Jiles-Atherton model is implemented by representing the load as an additional magnetic field. The results presented here are very similar to the Jiles-Atherton approach (equation 2.9); the only difference is a $\frac{3}{2}$ factor for H_σ. This new approach can be implemented for any hysteresis model. Here, a Preisach model with a general weight function is used when the effects of the load are represented by an additional magnetic field, as shown in equations (3.39) and (3.40).

Instead of including the effects of the load in the Preisach model, the system with load σ and magnetic field H can be regarded as equivalent to a system with no load and magnetic field $H + H_\sigma$. The Preisach model can be identified when there is no load. The generated hysteresis curve can be transformed for other stresses by using $H + H_\sigma$ instead of H. This approach can also be used when the Preisach model is identified at some load σ_1. The hysteresis curves for

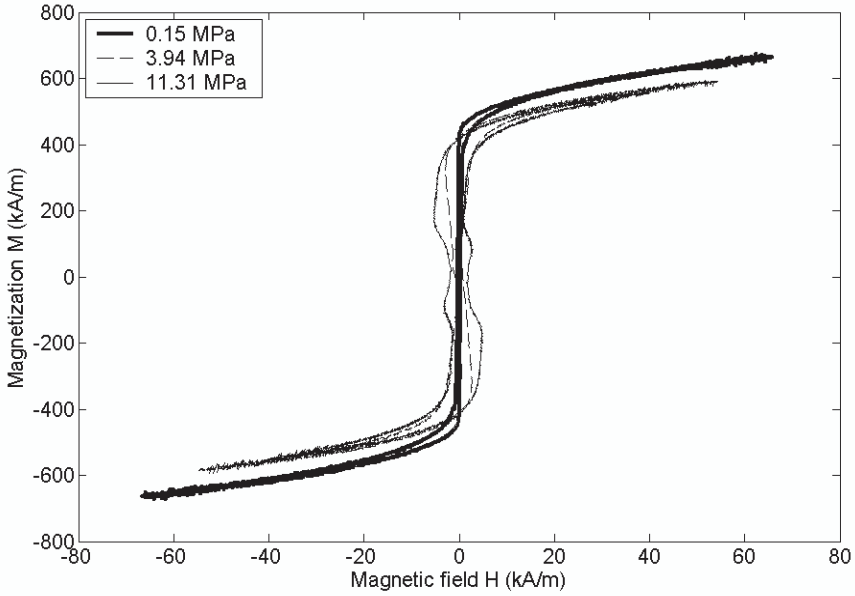

Figure 3-20: Magnetization versus H_d.

no load can be obtained by using $H - H_{\sigma_1}$ instead of H. In this case, the hysteresis curves at some other load σ_2 can be obtained by replacing H with $H - H_{\sigma_1} + H_{\sigma_2}$.

The derivative of elongation with respect to magnetization is needed in equation (3.40). Since the elongation is measured experimentally, obtaining such a derivative directly will result in numerical errors. To overcome this issue, a function is fitted to $\lambda(M, \sigma)$ and the derivative is obtained using the function. As shown in Figure 3-3, equation (3.2) does not provide satisfactory results for low stresses. The following new relation is used:

$$\lambda(M, \sigma) = a_1 M^2 + a_2 + \frac{a_5}{a_3} \ln \left[1 + \exp\left(a_3(M^2 - a_4^2 - a_6 M^4)\right)\right] \tag{3.41}$$

where a_1 to a_6 are constants for a constant stress. If the $\exp(\cdot)$ term is small this expression simplifies to $a_1 M^2 + a_2$, and if large, it simplifies to $(a_5 + a_1)M^2 + (a_2 - a_5 a_4^2) - a_5 a_6 M^4$. The former term is used to model the middle portion of Figure 3-3 while the latter term is used to model other parts. In Figure 3-21, a curve fitted by this function for a low stress is shown.

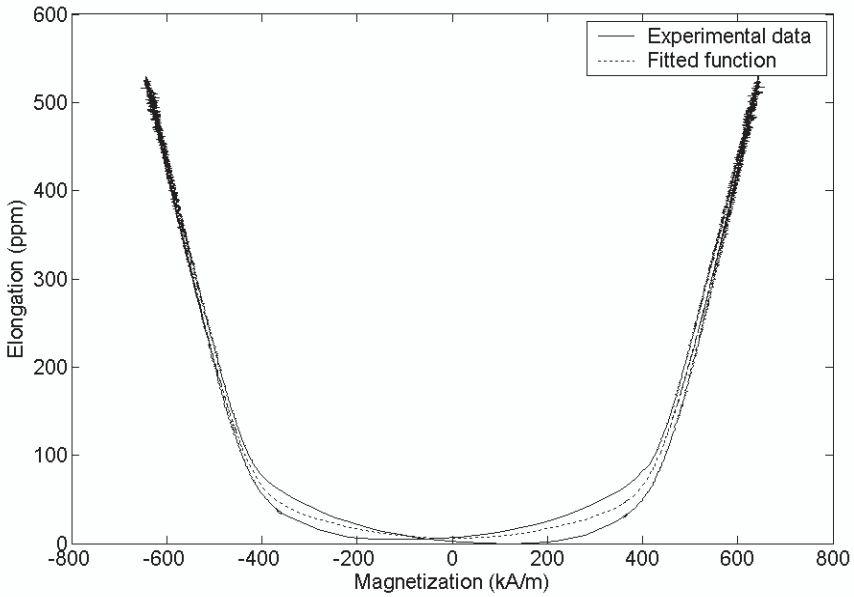

Figure 3-21: Elongation versus magnetization at 0.57 MPa. The fitted function matches the experimental data perfectly.

It was shown that the Preisach model with a general weight function can reproduce the major hysteresis curve with no error [58, 57]. Since in this subsection only major loops are discussed, instead of a curve generated by a Preisach model, the actual experimental data is used.

In Figure 3-22, the major loop at $\sigma_1 = -9.62\,\text{MPa}$ is transformed to $\sigma_2 = -9.07\,\text{MPa}$ by using the algorithm outlined. The transformed loop is compared with the experimental data. A very good agreement is seen. In Figure 3-23, the major loop at $\sigma_1 = -0.15\,\text{MPa}$ is transformed to $\sigma_2 = -11.31\,\text{MPa}$ and compared with experimental results. Since the stresses are very different, the curves do not agree closely. If the stress is not changing significantly, this approach provides accurate results.

As shown in Figure 3-14, the middle part of the hysteresis curve is not twisted at σ_1. In Figure 3-23, it is seen that the middle portion of the transformed curve is twisted similar to the experimental data at σ_2. The curvatures of the transformed loop and experimental data

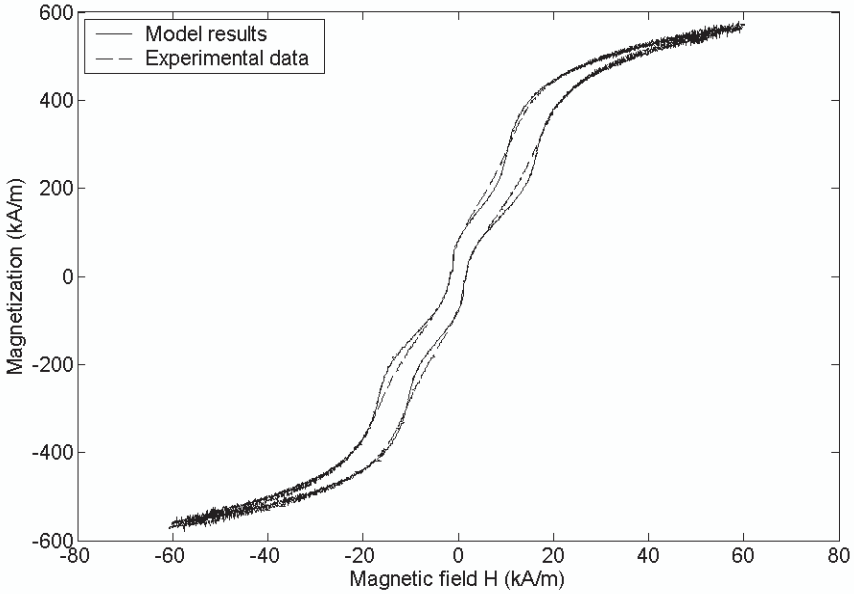

Figure 3-22: Experimental data and model results at 9.07 MPa.

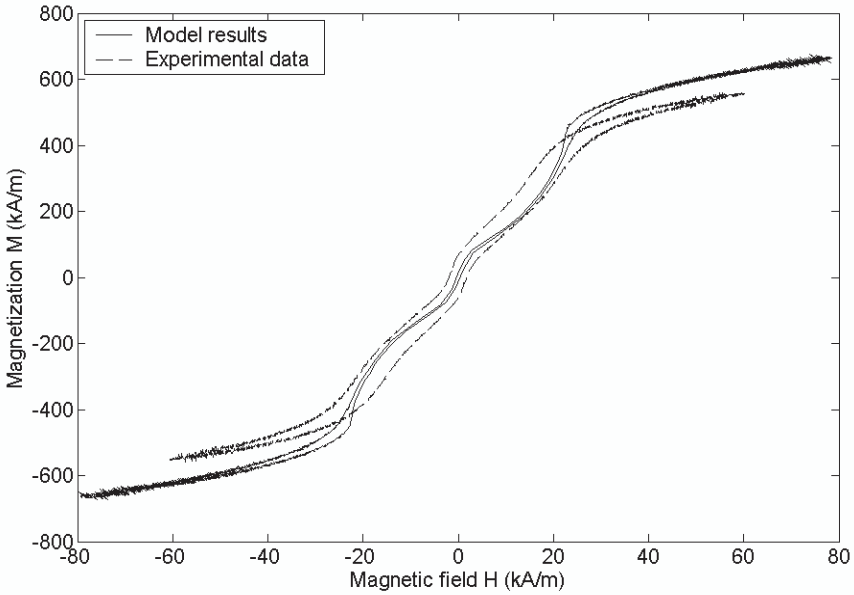

Figure 3-23: Experimental data and model results at 11.31 MPa.

agree qualitatively but not quantitatively. This can provide a possible new explanation for the unusual twisted hysteresis curve of Terfenol-D. Such curvature is not seen in regular non-magnetostrictive magnetic materials. If equation (3.2) is used to compute H_σ, the twisted portion is not regenerated. This establishes a link between the twisted portion of hysteresis curves in Figure 3-14 and the flat portion in the middle of magnetostriction curves in Figure 3-2. The reason for the flat portion in magnetostriction curves is likely causing the twist in hysteresis curves.

In Figure 3-20, it is seen that the curves are not exactly similar. It seems like for large stresses, the graph is stretched in the horizontal direction. To provide better accuracy for the new model, it is suggested that instead of H_d, $\frac{H_d}{S(M,\sigma)}$ is used in the Preisach model. The function $S(M,\sigma)$ is a scaling factor defined as follows:

$$S(M,\sigma) = d_1(\sigma) + d_2(\sigma)\left[1 - \tanh\left(d_3(\sigma)M^2\right)\right] \tag{3.42}$$

where $d_i(\sigma)$ are linear functions of the stress:

$$d_i(\sigma) = p_i + q_i\sigma. \tag{3.43}$$

Unlike the other results presented in this subsection, the introduction of $S(M,\sigma)$ is just a curve fitting attempt and has no physical reason. Using this approach a single hysteresis curve generated by the Preisach model is sufficient to produce hysteresis curves at all stresses with a reasonable accuracy. In this subsection, hysteresis curves at 4.48 MPa are chosen as the reference. The parameters p_i and q_i are determined by a least-square fit to the experimental data minimizing the following cost function:

$$J = \sum (H_m - H_{ex})^2 \tag{3.44}$$

where H_m and H_{ex} are the magnetic field from the model and experimental data, respectively. The parameter p_1 is set to 1 to restrain an extra degree of freedom when $S(M,\sigma)$ is multiplied

Parameter	Unit	Value
q_1	$\frac{1}{\text{MPa}}$	-0.1477
p_2	1	0.08247
q_2	$\frac{1}{\text{MPa}}$	-0.4477
p_3	$\left(\frac{\text{m}}{\text{A}}\right)^2$	-1.811×10^{-12}
q_3	$\frac{1}{\text{MPa}}\left(\frac{\text{m}}{\text{A}}\right)^2$	-9.892×10^{-13}

Table 3.6: The results of curve fitting

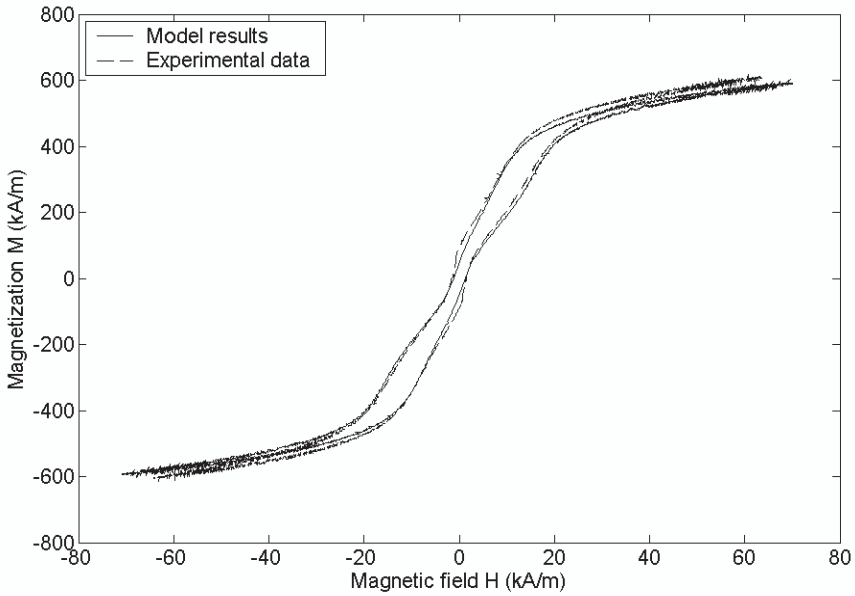

Figure 3-24: Experimental data and model results at 7.98 MPa.

by a constant value. Clearly, multiplying $S(M, \sigma)$ by a constant factor has no effect. The results are in Table 3.6.

In Figures 3-24, 3-25, and 3-26, the model results and experimental data are displayed and compared at different stresses. Good agreement is seen. To have a quantitative measure of modeling errors, root-mean-square error for the magnetization is computed. The maximum error of $18.1\frac{\text{kA}}{\text{m}}$ is seen at 7.98 MPa. The hysteresis curves at this stress are displayed in Figure 3-24. The average RMS error for all stresses is $11.7\frac{\text{kA}}{\text{m}}$.

In Figure 3-26, the hysteresis curves at 1.15 MPa are shown. It is seen that for parts of the

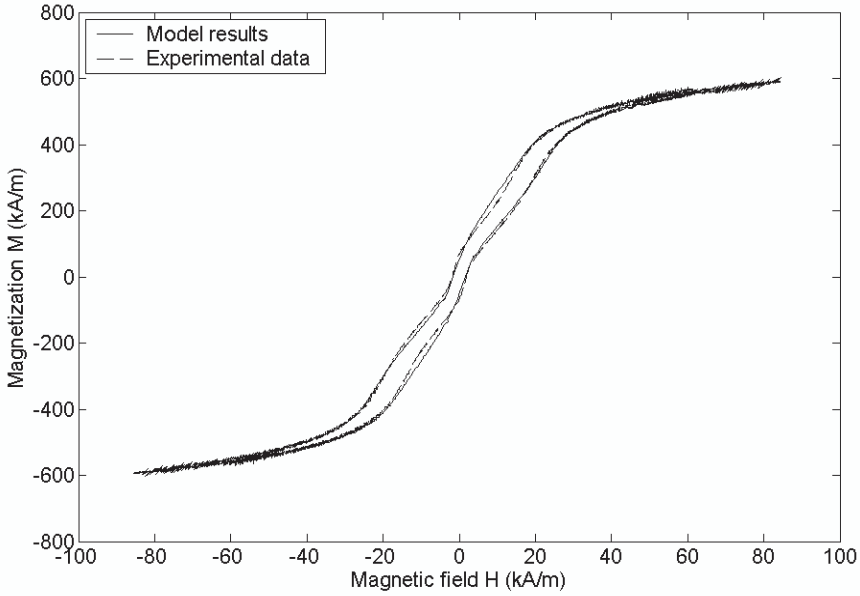

Figure 3-25: Experimental data and model results at 10.81 MPa.

middle portion of the hysteresis curve, the slope is negative. This feature is seen at some low stresses and is not physical. It is one of the model disadvantages. To resolve this issue, the reference stress at which the Preisach model is identified should be reduced. As stated before, the transformation discussed here is more accurate when the stresses are close. By lowering the stress at which the Preisach model is identified, more accuracy at lower stresses is obtained and the issue is resolved.

Since in this model, the magnetic field H is transformed monotonically, the new model is expected to handle minor loops properly. The new model inherits the wiping-out property from the Preisach model, but because of the nonlinearity of the transformation, the congruent minor loop property is lost.

This model is best implemented if an inverted hysteresis model is needed; that is when magnetization M is given and magnetic field H is requested. Using the Preisach model, $\frac{H_d}{S(M,\sigma)}$ can be computed. By using equations (3.39) and (3.42), magnetic field H is obtained. An inverted hysteresis model is useful for open-loop control strategies by linearization. (See Chapter

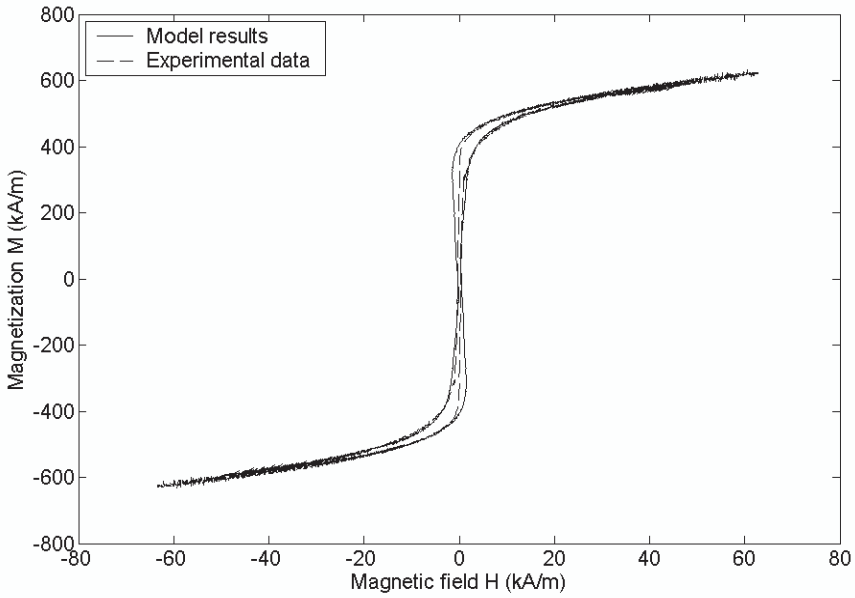

Figure 3-26: Experimental data and model results at 1.15 MPa.

4).

Since a Preisach model with a general weight function is used, the new model has many model parameters. The number of parameters for the homogenized energy model in the previous subsection is 11. The average RMS error for this model is $11.7\frac{\text{kA}}{\text{m}}$ and the average RMS errors for the homogenized energy model are in Table 3.5. The new model is this subsection is about twice more accurate. This accuracy is partially due to the large number of parameters. Since only algebraic transformations are used in the new model, it can be implemented efficiently.

In the next chapter, energy-based passivity and the properties of the Preisach model are used to develop closed-loop position and velocity controllers for the magnetostrictive actuator.

Chapter 4

Closed-loop control of magnetostrictive materials

In this chapter, closed-loop control of magnetostrictive actuators is examined. The first section reviews the literature related to passivity and control of hysteretic systems. In Section 2, energy-based passivity and velocity control of a magnetostrictive actuator are discussed. In Section 3, velocity and position control of hysteretic systems represented by the Preisach model are examined. Monotonicity of the model is established and used to derive several stability results.

4.1 Previous work

Energy-dissipating systems are frequently seen in engineering problems. For many of these systems, passivity can be established if the problem is properly formulated. In this case, the passivity theorem can be used to design a controller and establish stability for these systems. In [66], a few common passive systems are discussed.

Passivity-based controller design is frequently used for structural mechanical systems. In [12], passivity is established for a box-like structure with a few sensors and piezoceramic actuators. A LQG controller is designed based on passivity. The designed controller is verified by

simulation. In [11], passivity of a flexible beam is used to develop a fuzzy adaptive controller for the system that acts as a dynamic vibration absorber for a targeted frequency. In [2], passivity of a flexible beam is examined. An algorithm for controller design is proposed. The algorithm and the designed controller are verified by experimental data.

It has been shown that the Preisach model is a dynamical system with the Preisach boundary as the state [17]. In [18], passivity of a shape memory alloy actuator is shown. Passivity of the Preisach operator is established when the system output is the time-derivative of the traditional output. The associated storage function is also computed. This result is used to develop a velocity controller for shape memory alloys.

For magnetostrictive materials, many other approaches are also used for controller design. One popular approach is to linearize the system by adding the inverse of hysteresis before the actuator. This approach requires an accurate hysteresis model. If the model can be inverted, the system can be linearized. For this approach, the system needs to be accurately identified. Any inaccuracy in the model will affect the overall performance. In general, this approach leads to a complex controller because the hysteresis model inverse needs to be included in the controller. As a result, real-time implementation of this approach is difficult. In [56], the Preisach model is coupled to an ODE to model the magnetostrictive actuator. The model is inverted and used before the actuator to linearize the system. In [37, 38], the actuator is linearized by an inverse model and $\mathbb{H}_2$ and $\mathbb{H}_\infty$ optimal control is used to provide robust stability for the linearized system. In [39], a magnetostrictive actuator is controlled by a hybrid optimal controller. The actuator input is computed by a hysteresis model offline. A PI controller is added to compensate for unmodeled dynamics and provide robust position control.

In [45], the Jiles-Atherton model is used with optimal nonlinear control to provide stability. The model is numerically tested by simulation and shown to be robust. In [36], a model reference adaptive control based on the Preisach model is used for the controller.

In [31, 32], tracking and boundedness of the solution for hysteretic systems are studied using techniques for nonlinear dynamical systems. Because of the similarity to the results presented in this chapter, some of the results in [31, 32] are reviewed in Section 4.3 in detail.

4.2 Energy-based passivity and control of magnetostrictive materials

In this section, a model-independent passivity framework is developed for magnetostrictive actuators. The passivity results are used to identify a class of stabilizing velocity controllers. In the first subsection, definitions and background are included. The passivity for magnetostrictive materials is examined in Subsection 2. In Subsection 3, the homogenized energy model is used to identify the system storage function. The equilibrium state of the system is identified by minimizing the storage function. In Subsection 4, the passivity results are used to develop a velocity controller. For more information, see [61, 60].

4.2.1 Preliminary material

In this subsection, passivity is defined in a dynamical systems framework. This framework will be used later for magnetostrictive materials. Consider a system with input $u \in U$, output $y \in U$, and state $x \in X$. The following is a standard definition for dynamical systems [66].

Definition 1 *A dynamical system is defined through input, output and state spaces U and X, a readout operator r', and a state transition operator ϕ. The readout operator is a map from $U \times X$ to U. The state transition operator is a map from $\mathbb{R}^2 \times X \times U$ to X. The state transition operator must have the following properties for all $x_0 \in X$, t_0, t_1, $t_2 \in \mathbb{R}$, u, u_1, $u_2 \in U$:*

Consistency: $\phi(t_0, t_0, x_0, u) = x_0$.

Determinism: $\phi(t_1, t_0, x_0, u_1) = \phi(t_1, t_0, x_0, u_2)$ *for all* $t_1 \geq t_0$ *when* $u_1(t) = u_2(t)$ *for all* $t_0 \leq t \leq t_1$.

Semi-group: $\phi(t_2, t_0, x_0, u) = \phi(t_2, t_1, \phi(t_1, t_0, x_0, u), u)$ *when* $t_0 \leq t_1 \leq t_2$.

Stationarity: $\phi(t_1 + T, t_0 + T, x_0, u_T) = \phi(t_1, t_0, x_0, u)$ *for all* $t_1 \geq t_0$, $T \in \mathbb{R}$ *when* $u_T(t) = u(t + T)$ *for all* $t \in \mathbb{R}$.

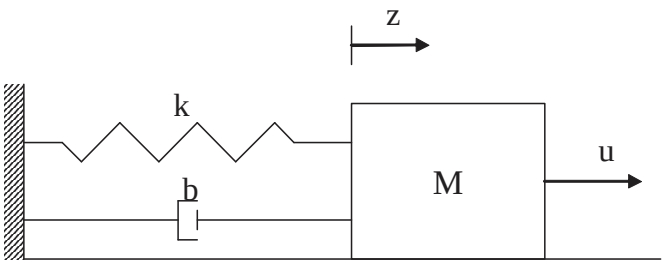

Figure 4-1: A spring-mass-dashpot system.

Definition 2 *[66] Consider a dynamical system with state variables x, an input u and output y. If there is a real-valued function $S(x)$ satisfying the following relation for any $t_i \leq t_f$ and if $S(x)$ is bounded from below, the dynamical system is called passive:*

$$S(x(t_i)) + \int_{t_i}^{t_f} \langle u, y \rangle \, dt \geq S(x(t_f)). \tag{4.1}$$

In this definition, $\langle ., . \rangle$ is the inner product on U. The variables u and y are vectors of the same dimension, so that $\langle u, y \rangle$ is defined. The scalar function $S(x)$ is called the storage function. Passive systems are frequently seen in engineering. The storage function is often the energy.

Example: Consider a spring-mass-dashpot system (Figure 4-1). The following equation describes this system:

$$M\frac{d^2z}{dt^2} + b\frac{dz}{dt} + kz = u, \tag{4.2}$$

where u is the external force applied. The velocity of the mass $\dot{z}$ is considered to be the system output: $y = \dot{z}$. The state variables are z and $\dot{z}$. If both sides of equation (4.2) are multiplied by $\dot{z}$ and integrated from t_i to t_f, it becomes:

$$\frac{M}{2}\left(\dot{z}^2(t_f) - \dot{z}^2(t_i)\right) + \int_{t_i}^{t_f} b\dot{z}^2 dt + \frac{k}{2}\left(z^2(t_f) - z^2(t_i)\right) = \int_{t_i}^{t_f} \langle u, y\rangle \, dt. \tag{4.3}$$

In this example, total energy is

$$E(z, \dot{z}) = \frac{1}{2}kz^2 + \frac{1}{2}M\dot{z}^2. \tag{4.4}$$

Using this definition and assuming $b \geq 0$, equation (4.3) can be rewritten as

$$E(z(t_i), \dot{z}(t_i)) + \int_{t_i}^{t_f} \langle u, y\rangle \, dt \geq E(z(t_f), \dot{z}(t_f)). \tag{4.5}$$

The storage function $E(z, \dot{z})$ is always non-negative and hence, bounded from below. As a result, this system is passive. When $u = 0$, as t approaches infinity, the system goes to a state which minimizes E. The energy E is minimized when $z = 0$, $\dot{z} = 0$. This is the global system equilibrium point.

When the force applied to the system includes a constant force, such as gravity, its effect can be included in the system storage function. If the force applied to the mass is $F_{const} + u$, the following storage function is minimized at the equilibrium point:

$$\bar{E} = E - F_{const}z. \tag{4.6}$$

In this case, the equilibrium point is $z = \frac{F_{const}}{k}$, $\dot{z} = 0$.

Define the set $\mathbb{R}_+$ and the operator $\|\cdot\|$ to be the set of non-negative real numbers and the Euclidean norm, respectively. The following definitions are used to establish stability for a dynamical system [63].

Definition 3 *The set L_2^n consists of all measurable functions $f : \mathbb{R}_+ \to \mathbb{R}^n$ such that*

$$\int_0^\infty \|f(t)\|^2 \, dt < \infty. \tag{4.7}$$

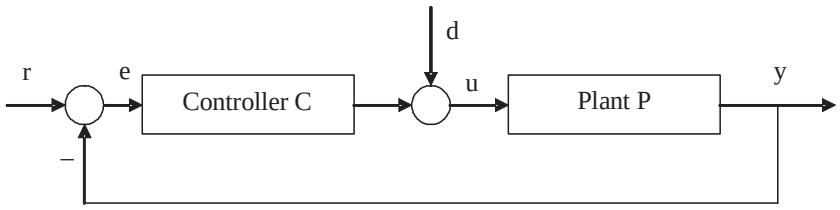

Figure 4-2: The standard feedback configuration.

Definition 4 *The L_2-norm of a function $f \in L_2^n$ is*

$$\|f(\cdot)\|_2 = \sqrt{\int_0^\infty \|f(t)\|^2 \, dt}. \tag{4.8}$$

Definition 5 *The set L_∞^n consists of all measurable functions $f : \mathbb{R}_+ \to \mathbb{R}^n$ that are bounded on $[0, \infty)$.*

Definition 6 *The L_∞-norm of a function $f \in L_\infty^n$ is*

$$\|f(\cdot)\|_\infty = \sup_{t \in \mathbb{R}_+} \|f(t)\| . \tag{4.9}$$

Definition 7 *Consider a function $f : \mathbb{R}_+ \to \mathbb{R}^n$. The truncation of f to the interval $[0, T]$ is*

$$f_T(t) = \begin{cases} f(t), & 0 \le t \le T \\ 0, & T < t \end{cases} . \tag{4.10}$$

Definition 8 *The set L_{pe}^n consists of all measurable functions $f : \mathbb{R}_+ \to \mathbb{R}^n$ with the property that $f_T \in L_p^n$ for all finite T when $p = 2$ or ∞.*

Definition 9 *A mapping $R : L_{pe}^n \to L_{pe}^m$ is said to be L_p-stable if $u \in L_p^n$ implies that $Ru \in L_p^m$.*

Suppose a given system P is passive. Consider the general feedback control configuration shown in Figure 4-2. If the controller C satisfies certain conditions, the following result can be used to show the stability of the controlled system.

Theorem 10 *[14, theorem 10, page 182] Consider the feedback system shown in Figure 4-2 where C and P map U to U. The set U is a subset of L_{2e}^m. Assume that for any r and d in L_2^m, there are solutions e and u in L_{2e}^m and there are constants α_1, α_2, α_3, β_1, β_2, and β_3 such that for every real T and $x \in L_{2e}^n$ the following conditions hold:*

$$\begin{array}{lrcl} \text{I} & \|(Cx)_T\|_2 & \leq & \alpha_1 \|x_T\|_2 + \beta_1, \\ \text{II} & \displaystyle\int_0^T \langle x, Cx\rangle \, dt & \geq & \alpha_2 \|x_T\|_2^2 + \beta_2, \\ \text{III} & \displaystyle\int_0^T \langle Px, x\rangle \, dt & \geq & \alpha_3 \|(Px)_T\|_2^2 + \beta_3. \end{array} \tag{4.11}$$

If $\alpha_2 + \alpha_3 > 0$, then r, $d \in L_2$ implies that e, u, Ce, $y \in L_2^m$.

A passive system satisfies the third condition with $\alpha_3 = 0$ and $\beta_3 = \inf S(x) - S(x(0))$. The second and third conditions are similar to requiring that plant and controller be passive, but slightly stronger since $\alpha_2 + \alpha_3$ has to be strictly positive. The last line of the theorem states that the closed loop is L_2-stable.

This theorem can be used to establish stability for a large class of nonlinear systems. For many systems this theorem is the only way to establish stability. The passivity results which will be shown later can be used with this theorem to show stability for a controlled magnetostrictive system.

4.2.2 Passivity for magnetostrictive materials

Since magnetostrictive materials dissipate energy, we expect them to be passive with some energy function as the storage function. In this section, the physical parameters of magnetostrictive materials are introduced. Three different energy functions for magnetostrictive materials and their suitability as a storage function are discussed. Finally, a proof of passivity is given.

For magnetostrictive materials, the magnetization M is not the only parameter affected by an external magnetic field H. The mechanical variables are also affected. For a material where the magnetic and mechanical responses are decoupled, the stress σ is usually considered

to be the input for the mechanical part, and the strain ε, the response. For magnetostrictive materials, a magnetic field affects both magnetization and strain, and similarly for the stress. For magnetostrictive materials, generalized force and displacement are defined as follows:

$$\begin{aligned} F &= \begin{pmatrix} \mu_0 H \\ \sigma \end{pmatrix}, \\ X &= \begin{pmatrix} M \\ \varepsilon \end{pmatrix}. \end{aligned} \tag{4.12}$$

Generalized force F is the system input and time-derivative of generalized displacement $\dot{X}$, the output. The constant μ_0 is a physical constant to ensure that $\mu_0 \langle H, M \rangle$ has the unit of energy per unit volume.

Various energy functions can be associated with magnetostrictive materials. Here these energy functions are introduced and their suitability as a storage function are discussed.

The internal energy

The internal energy U is the total potential energy stored in the material. The first law of thermodynamics holds for this energy function:

$$\frac{dU}{dt} = \frac{dQ}{dt} + \frac{dW}{dt}, \tag{4.13}$$

where $\frac{dQ}{dt}$ is the rate of thermal energy supplied to the material and $\frac{dW}{dt}$ is the rate of magnetic/mechanical work done on the system. The inequality of Clausius [67, page 205] states that for any process $\frac{dS}{dt} \geq \frac{1}{T}\frac{dQ}{dt}$ where T is the temperature and S is the entropy. Using this inequality, the first law can be written as

$$\frac{dU}{dt} \leq T\frac{dS}{dt} + \frac{dW}{dt}. \tag{4.14}$$

A relation similar to the passivity inequality can be obtained by integrating both sides of equation (4.14) from t_i to t_f:

$$U_i + \int_{t_i}^{t_f} \left(T\frac{dS}{dt} + \frac{dW}{dt} \right) dt \geq U_f. \tag{4.15}$$

In this relation, $\frac{dW}{dt} = \left\langle F, \frac{dX}{dt} \right\rangle$. It is seen that thermal terms should appear in the system input/output, i.e. u should be $\begin{pmatrix} \mu_0 H \\ \sigma \\ T \end{pmatrix}$ and y should be $\begin{pmatrix} \dot{M} \\ \dot{\varepsilon} \\ \dot{S} \end{pmatrix}$. Since the energy stored in the material is limited, the amount of energy which can be pulled out of the material is also limited. This means that the energy function U has a lower bound. As a result, the internal energy U can be used as a storage function.

However, thermal variables are usually difficult to work with. For magnetostrictive materials, they are difficult to measure. Extra thermal input and output are disadvantages to using internal energy as a storage function. For this reason, the internal energy is not chosen as the storage function.

The Gibbs energy

The following relation defines the Gibbs energy:

$$G = U - TS - \langle F, X \rangle . \tag{4.16}$$

In Subsection 3.2.1, the Gibbs energy for a dipole in a magnetostrictive system is obtained using the homogenized energy model. By combining equations (3.10), (3.12), and (3.17) and assuming $R_{r,s} = 1$, the Gibbs energy at a large magnetic field H is obtained.

$$G_{r,s} = \frac{1}{2} Y \varepsilon^2 + \frac{\mu_0}{2} \eta' M_R^2 - \frac{\mu_0 (H - s + \eta' M_R)^2}{2(\eta' - \frac{2Y\gamma_1 \varepsilon}{\mu_0})} - \sigma\varepsilon. \tag{4.17}$$

The overall Gibbs energy can be obtained by adding individual Gibbs energies for the dipoles. It is seen that the Gibbs energy is a function of H. This means that H has to be included in the system states. This is awkward for several reasons. First, in this application H is an input. Second, for situations in which $\varepsilon = 0$ and H has a large value, the Gibbs energy can be made arbitrarily small by increasing H. This means that the Gibbs energy does not have a lower bound, and hence it is not a suitable storage function.

The Helmholtz energy

The Helmholtz free energy ψ is defined as

$$\psi = U - TS, \tag{4.18}$$

where T and S are the temperature and total entropy, respectively, of the system. Using the inequality of Clausius, the first law of thermodynamics (4.14) can be written as

$$\frac{d\psi}{dt} \leq -S\frac{dT}{dt} + \frac{dW}{dt}. \tag{4.19}$$

Under constant temperature, this equation simplifies to

$$\frac{d\psi}{dt} \leq \frac{dW}{dt}. \tag{4.20}$$

This relation states that the rate of work provided is more that the rate at which Helmholtz free energy is increased. It can be said that part of the work energy provided is absorbed by the system and added to the stored energy, while the rest is wasted in energy dissipation. The Helmholtz free energy can be regarded as the energy actually stored in the system. In this respect, the Helmholtz energy is comparable to the energy storage function E in the mechanical example. Since the energy E is the storage function for the mechanical example, this comparison

suggests the Helmholtz energy as the storage function. In the next subsection, a detailed proof of passivity, with the Helmholtz free energy as the storage function, is given.

Proof of passivity

It is assumed that, during any process discussed here, no phase transition occurs. This guarantees the existence of partial derivatives. All of the processes are under constant air pressure and the work done by the air pressure is negligible. For simplicity, from now on, it is also assumed that the thermal connection between the material and the surrounding environment is such that the temperature of the material is always close to the room temperature T_0 and constant.

In a magnetic material, the ratio between the dipole magnetic energy and the energy of thermal fluctuations plays an important role. If the dipole magnetic energy is small compared to thermal fluctuations, the material is called *paramagnetic*. In this case, the dipoles are mostly affected by thermal fluctuations and the external magnetic field H. Dipole-dipole interaction is weak. Because of thermal fluctuations, paramagnetic materials are memoryless and have no hysteresis. On the other hand, if the dipole magnetic energy is large compared to thermal fluctuations, the material is called *ferromagnetic*. Dipoles in a ferromagnetic sample retain their state, and the material has memory. These materials are hysteretic. Because of strong dipole-dipole interactions in ferromagnetic materials, the models available for these materials are complex and difficult to use. The energy of thermal fluctuations depends linearly on temperature. For this reason if a ferromagnetic material is heated, in a certain temperature it becomes paramagnetic. This transition temperature is called the Curie temperature T_c. Curie temperature is fairly high for most of the ferromagnetic materials. For iron $T_c = 1043\,\mathrm{K}$.

When a ferromagnetic material is heated beyond T_c, it becomes paramagnetic and during this heating process, the entropy of the material is increased. In the following lemmas, this fact is used together with entropy relations for a paramagnetic material to show an upper bound for the entropy in a ferromagnetic material. The first lemma is used to show that the Helmholtz free energy has a lower-bound.

Lemma 11 *For a paramagnetic material at a constant temperature, the entropy S has an upper bound.*

Proof. The strength of a magnetic dipole is denoted by a constant positive half-integer J. This constant depends on the material under discussion. The following equations define entropy for a single dipole in a paramagnetic sample [42, pages 213, 215, and 259]:

$$\begin{aligned} \beta &= \frac{1}{kT}, \\ \eta &= c\beta \left\| H \right\|, \\ Z &= \frac{\sinh\left[(J+\frac{1}{2})\eta\right]}{\sinh\left[\frac{1}{2}\eta\right]}, \\ S &= k(\ln Z - \beta \frac{\partial \ln Z}{\partial \beta}), \end{aligned} \tag{4.21}$$

where c is a positive constant and k is the Boltzmann constant $k = 1.38e-23\frac{\mathrm{J}}{\mathrm{K}}$.

In a paramagnetic sample with N dipoles, total magnetic entropy is simply N times the entropy of a single dipole. Total magnetic entropy is maximized when $H = 0$. (See appendix A.) This result is consistent with physics since in the presence of an external magnetic field, dipoles become oriented and the overall system disorder is reduced. Thus,

$$S_{\max} = S_{H=0} = kN \ln(2J+1). \tag{4.22}$$

Thus, at a constant temperature, the magnetic portion of entropy has an upper-bound, $S_{\max}$.

The nonmagnetic portion of the entropy is a function of temperature and external load. At any temperature, this entropy is maximized for the highest possible (tensile) external load. This means that at any temperature, the nonmagnetic portion of the entropy has an upper bound. Thus at any temperature, the total entropy has an upper bound. ■

The paramagnetic state is usually obtained at a high temperature. In order to have an upper bound for entropy in normal working conditions of the material, the lemma above should be extended to ferromagnetic materials.

Lemma 12 *For any magnetic material at a constant temperature, the entropy S has an upper-bound.*

Proof. Lemma 11 states that the entropy has an upper bound for paramagnetic state. Here we are interested in the ferromagnetic state.

To obtain a relation for entropy in ferromagnetic state, consider a process in which the ferromagnetic material is heated from an arbitrary initial state to a paramagnetic state. The entropy and temperature for initial state are S_i and T_i, respectively. For the paramagnetic state, the entropy and temperature are S_p and T_p, respectively. From Lemma 11, it is known that S_p has an upper bound.

The entropy is a function of system states [67, page 217]. The difference between any two arbitrary states is only a function of the states. This difference is independent of the process which connects the two states. This fact holds for the process mentioned above. The difference $S_p - S_i$ does not depend on the process as long as the initial and final conditions remain the same. For simplicity, consider a process in which, the temperature is increased monotonically.

Since the temperature is always increasing during this process, there should be a non-negative heat flow to the material during the process:

$$\frac{dQ}{dt} \geq 0. \tag{4.23}$$

The inequality of Clausius states that for any process $\frac{dS}{dt} \geq \frac{1}{T}\frac{dQ}{dt}$. As a result, in this process $\frac{dS}{dt} \geq 0$ or $S_p - S_i \geq 0$. Since S_p has an upper bound, S_i is bounded from above. This concludes the proof. ■

The following is an immediate result of the lemma above.

Theorem 13 *For a constant temperature, the Helmholtz free energy $\psi = U - TS$ is bounded from below.*

Proof. Lemma 12 states that the entropy has an upper bound. This means that $-TS$ has a lower bound. The internal energy U has a lower bound. This results in ψ to be bounded from below. ■

Theorem 14 *At a constant temperature, the following passivity condition is satisfied when the storage function is the Helmholtz free energy ψ:*

$$\psi_i + \int_{t_i}^{t_f} \left\langle F, \frac{dX}{dt} \right\rangle dt \geq \psi_f. \tag{4.24}$$

Here, subscripts i and f denote initial and final conditions, respectively; F and X are the generalized force applied to the system and the generalized system output, respectively as defined in (4.12).

Proof. If the temperature is constant, equation (4.19) can be written as

$$\frac{d\psi}{dt} \leq \frac{dW}{dt}, \tag{4.25}$$

where $\frac{dW}{dt} = \left\langle F, \frac{dX}{dt} \right\rangle$ is the rate of magnetic/mechanical work done on the system.

If both sides are integrated from t_i to t_f, we obtain

$$\psi_f - \psi_i \leq \int_{t_i}^{t_f} \left\langle F, \frac{dX}{dt} \right\rangle dt, \tag{4.26}$$

or

$$\psi_i + \int_{t_i}^{t_f} \left\langle F, \frac{dX}{dt} \right\rangle dt \geq \psi_f. \tag{4.27}$$

Theorem 13 shows that the Helmholtz free energy is bounded from below, which means that it is a valid storage function. This concludes the proof. ■

The proof above shows the passivity of a magnetostrictive system with a three-dimensional magnetic field and a one-dimensional stress-strain. In this proof, no model for magnetostrictive material is assumed. Passivity is shown with fundamental laws of physics only. In fact, the theorem above can be applied to any model for magnetostrictive materials.

4.2.3 Helmholtz free energy using the homogenized energy model

In this subsection, the total Helmholtz free energy for a magnetostrictive material is calculated using the homogenized energy model introduced in Subsection 3.2.1. The model presented in

Subsection 3.3.1 is not used because a closed-form solution to equation (3.27) is not available. Since the Helmholtz free energy is the system storage function, it is written as a function of system states $\tau(t, r)$ and ε.

As stated in Subsection 3.2.1, the local magnetic field H_0 is the local magnetic field at a dipole and H is the external magnetic field at the macroscopic level which can be measured. It was stated that the local magnetic field H_0 might not be equal to the external magnetic field H. This difference between H and H_0 should have some effect on the energy functions. For example, consider a dipole with a negative $s = H - H_0$ when the dipole magnetization is increased by dM and the external magnetic field H is constant: Work done by the external magnetic source is HdM and work done on the dipole is $H_0 dM = HdM - sdM$. It is seen that the work done on the dipole is more that the work done by the external magnetic field. This extra work is not done by the external field. The imperfections and nonhomogeneities which are the source of the difference between H and H_0 should have done this work on the dipole. As a result, they need to be considered when the overall system Helmholtz free energy is computed.

From equation (3.12),

$$G_{r,s}(H_0, M_{r,s}) = \psi_{r,s}(M_{r,s}) - \mu_0 H_0 M_{r,s} - \sigma\varepsilon \tag{4.28}$$

where r is defined by equation (3.11). Define $\bar{\psi}_{r,s}(M_{r,s})$ and $\bar{G}_{r,s}(H, M_{r,s})$ to be the Helmholtz free energy and Gibbs energy respectively in terms of external variables. When the system is viewed from an external point of view, the combined effect of the dipole and the imperfections are seen. To find $\bar{\psi}_{r,s}(M_{r,s})$ and $\bar{G}_{r,s}(H, M_{r,s})$, an assumption for the imperfections and nonhomogeneities must be made and based on that, the contribution to the Helmholtz free energy computed. Another approach is to construct $\bar{\psi}_{r,s}(M_{r,s})$ by studying the equilibrium points of the system for a constant magnetic field.

The equilibrium points for a constant magnetic field in terms of the external variables (H,$M_{r,s}$) can be obtained from two methods:

1. The equilibrium condition can be written for $\bar{G}_{r,s}(H, M_{r,s})$.

2. The system parameters can be transformed to the local variables (H_0,$M_{r,s}$). The equilibrium condition is written for $G_{r,s}(H_0, M_{r,s})$, and the results are transformed back to the external variables.

These two methods must be equivalent.

The equilibrium conditions for $\bar{G}_{r,s}(H, M_{r,s})$ and $G_{r,s}(H_0, M_{r,s})$ are:

$$\left(\frac{\partial \bar{G}_{r,s}(H,M_{r,s})}{\partial M_{r,s}}\right)_{T,H} = 0, \quad \left(\frac{\partial G_{r,s}(H_0,M_{r,s})}{\partial M_{r,s}}\right)_{T,H_0} = 0, \tag{4.29}$$

where $H = H_0 + s$ and s is assumed constant. Further,

$$\begin{aligned} \left(\frac{\partial G(H_0, M_{r,s})}{\partial M_{r,s}}\right)_{T,H_0} &= \left(\frac{\partial}{\partial M_{r,s}}\right)_{T,H} (\psi(M_{r,s}) - \mu_0 H_0 M_{r,s} - \sigma\varepsilon) \\ &= \left(\frac{\partial}{\partial M_{r,s}}\right)_{T,H} (\psi(M_{r,s}) - \mu_0 H M_{r,s} + \mu_0 s M_{r,s} - \sigma\varepsilon) \\ &= 0. \end{aligned} \tag{4.30}$$

Now, $\bar{G}_{r,s}(H, M_{r,s})$ equals $G_{r,s}(H - s, M_{r,s})$ or

$$\bar{G}_{r,s}(H, M_{r,s}) = \psi(M_{r,s}) - \mu_0 H M_{r,s} + \mu_0 s M_{r,s} - \sigma\varepsilon. \tag{4.31}$$

It can be shown that the equilibrium conditions (4.29) are identical. Defining $\bar{\psi}_{r,s}(M_{r,s})$ so that $\bar{G}_{r,s}(H, M_{r,s}) = \bar{\psi}_{r,s} - \mu_0 H M_{r,s} - \sigma\varepsilon$, analogously with equation (3.12), we have

$$\bar{\psi}_{r,s}(M_{r,s}) = \psi(M_{r,s}) + \mu_0 s M_{r,s}. \tag{4.32}$$

Equation (3.17) gives the equilibrium magnetization for a dipole. By combining equations (3.10), (3.17), and (4.32), the equilibrium value of $\bar{\psi}_{r,s}$ for each dipole is obtained:

$$\bar{\psi}^*_{r,s} = \frac{1}{2}Y\varepsilon^2 + \frac{\frac{\mu_0}{2}(H^2 - s^2) - \eta' M_R(Y\gamma_1\varepsilon M_R - \mu_0 s R_{r,s})}{\eta' - \frac{2Y\gamma_1\varepsilon}{\mu_0}}. \tag{4.33}$$

Similar to equation (3.18), by assuming a distribution for r and s, the Helmholtz free energy for the entire system can be found using the superposition principle:

$$\psi_{Tot}(\tau(t,r),\varepsilon) = C\int_0^\infty \int_{-\infty}^\infty \bar{\psi}^*_{r,s}\mu(r,s)dsdr. \tag{4.34}$$

By combining equations (2.3), (4.33), and (4.34), the following equation is obtained:

$$\psi_{Tot}(\tau(t,r),\varepsilon) = \frac{C\mathcal{I}_0}{2}Y\varepsilon^2 + \frac{C}{\eta' - \frac{2Y\gamma_1\varepsilon}{\mu_0}} \left(\frac{\mu_0\mathcal{I}_0\tau^2(t,0)}{2} - \eta' Y\gamma_1\varepsilon M_R^2\mathcal{I}_0 + \eta' M_R\mu_0 A - \frac{\mu_0}{2}\mathcal{I}_2\right), \tag{4.35}$$

where the functions $\mathcal{I}_n$ are defined by equation (3.19) and $A = \int_0^\infty \int_{-\infty}^\infty R_{r,s}s\mu(r,s)dsdr = 2\int_0^\infty \int_{-\infty}^{\tau(t,r)} s\mu(r,s)dsdr - \mathcal{I}_1$.

This is the value of the Helmholtz free energy, the storage function for the magnetostrictive system, for any ε and Preisach boundary $\tau(t,r)$. The only nontrivial aspect of calculating $\psi_{Tot}(\tau(t,r),\varepsilon)$ is efficient computation of A. It is seen that the double integral of A is very similar to the double integral used for computing M (equations (2.1) or (3.18)). In fact, any efficient algorithm used for the computation of M can be used here, for example that on [33, p. 37]; only the weight function is slightly different.

Minimum of the storage function

As stated in page 29, the Preisach boundary $\tau(t,r)$ and strain ε are the system states. Here, the Preisach boundary that globally minimizes the storage function is obtained.

Suppose that when $\tau(t,r) = \tau^*(t,r)$ and $\varepsilon = \varepsilon^*$, $\psi_{Tot}(\tau(t,r),\varepsilon)$ is globally minimized. If ε is held fixed at $\varepsilon = \varepsilon^*$ and $\tau(t,r)$ is changed, $\psi_{Tot}(\tau(t,r),\varepsilon^*)$ is minimized when $\tau(t,r) = \tau^*(t,r)$. This means that $\tau^*(t,r)$ globally minimizes the following function:

$$\psi_{Tot}(\tau(t,r),\varepsilon^*) = \frac{C\mathcal{I}_0}{2}Y\varepsilon^{*2} + \frac{C}{\eta' - \frac{2Y\gamma_1\varepsilon^*}{\mu_0}} \qquad \left(\frac{\mu_0\mathcal{I}_0\tau^2(t,0)}{2} - \eta' Y\gamma_1\varepsilon^* M_R^2\mathcal{I}_0 \right. \\ \left. +\eta' M_R\mu_0 A - \frac{\mu_0}{2}\mathcal{I}_2\right). \tag{4.36}$$

The following terms are the only variable parts of the storage function:

$$\begin{aligned} F_1\left(\tau(t,r)\right) &= \frac{\mu_0\mathcal{I}_0\tau^2(t,0)}{2}, \\ F_2\left(\tau(t,r)\right) &= A. \end{aligned} \tag{4.37}$$

Assume that the weight function $\mu(r,s)$ is non-negative for all r and s. Since $\eta' - \frac{2Y\gamma_1\varepsilon^*}{\mu_0}$ is a positive quantity, if F_1 and F_2 are minimized at the same time, the storage function is minimized. Function F_1 is minimized when $\tau(t,0) = 0$. Function F_2 is minimized when A is minimized:

$$A = 2\int_0^\infty \int_{-\infty}^{\tau(t,r)} s\mu(r,s)dsdr - \mathcal{I}_1. \tag{4.38}$$

The sign of the integrand equals the sign of s. This integration is minimized when the region of integration is the subset of the Preisach plane on which the integrand is negative. This is the lower half of the Preisach plane. Thus, the integration is minimized when the boundary $\tau(t,r) = 0$. This Preisach plane boundary is shown in Figure 4-3.

Function F_2 is globally minimized with the boundary $\tau(t,r) = 0$. Since this boundary also globally minimizes F_1, this results in global minimization of the storage function.

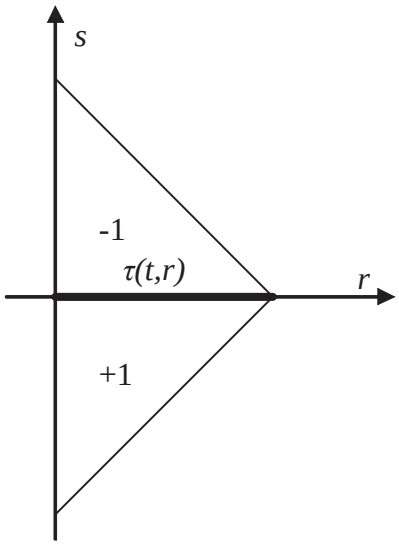

Figure 4-3: The global minimum Preisach boundary.

It is commonly seen that the weight function $\mu(r, s)$ is an even function of s; that is $\mu(r, s) = \mu(r, -s)$ for all r and s [62, 47]. If this condition holds, by substituting the Preisach boundary $\tau(t, r) = 0$ in equation (3.20), it is seen that the resulting magnetization is zero. In this case there is no magnetic field H, magnetization M, or flux density B. This state is called the demagnetized state and is the state of lowest "energy" for the system.

Storage function in presence of a constant input

When the stress and magnetic field applied to the system include a constant portion, the system can be simplified by redefining the input as $\bar{u} = \begin{pmatrix} \mu_0(H - H_{const}) \\ \sigma - \sigma_{const} \end{pmatrix}$, while the output is not changed. In this case, the system is passive with the following storage function:

$$\psi^F = \psi_{Tot} - \mu_0 \langle H_{const}, M_{Tot} \rangle - \sigma_{const}\varepsilon, \tag{4.39}$$

where ψ_{Tot} is the system Helmholtz free energy and M_{Tot} is the system magnetization. This situation is analogous to the example of a spring with a constant imposed force, such as gravity,

discussed in Subsection 4.2.1.

Theorem 15 *At a constant temperature, in the presence of a constant input, the following passivity condition is satisfied when the storage function is ψ^F:*

$$\psi_i^F + \int_{t_i}^{t_f} \left\langle \bar{u}, \frac{dX}{dt} \right\rangle dt \geq \psi_f^F . \tag{4.40}$$

Subscripts i and f denote initial and final conditions respectively and $X = \begin{pmatrix} M \\ \varepsilon \end{pmatrix}$ is the generalized displacement.

Proof. If the definition of $\bar{u}$ and ψ^F is substituted in the result of Theorem 14, the result is

$$\begin{aligned} \psi_i^F + \mu_0 \langle H_{const}, M_{Tot,i} \rangle + \sigma_{const}\varepsilon_i + \int_{t_i}^{t_f} \left\langle \bar{u} + \begin{pmatrix} \mu_0 H_{const} \\ \sigma_{const} \end{pmatrix}, \frac{dX}{dt} \right\rangle dt \\ \geq \psi_f^F + \mu_0 \langle H_{const}, M_{Tot,f} \rangle + \sigma_{const}\varepsilon_f . \end{aligned} \tag{4.41}$$

This simplifies to

$$\psi_i^F + \int_{t_i}^{t_f} \left\langle \bar{u}, \frac{dX}{dt} \right\rangle dt \geq \psi_f^F . \tag{4.42}$$

Since both M_{Tot} and ε have a lower bound and an upper bound, existence of a lower bound for ψ_{Tot} implies that ψ^F has a lower bound. The proof is complete. ■

The storage function ψ^F can be written as a function of the Preisach boundary $\tau(t,r)$ and ε by combining equations (4.35) and (4.39):

$$\begin{aligned} \psi^F(\tau(t,r),\varepsilon) = \frac{C\mathcal{I}_0}{2} Y\varepsilon^2 + \frac{C}{\eta' - \frac{2Y\gamma_1\varepsilon}{\mu_0}} \quad & \left(\frac{\mu_0\mathcal{I}_0 \left(\tau(t,0) - H_{const}\right)^2}{2} - \frac{\mu_0\mathcal{I}_0 H_{const}^2}{2} \right. \\ & -\eta' Y\gamma_1\varepsilon M_R^2\mathcal{I}_0 + \mu_0 H_{const} M_R \eta'\mathcal{I}_0 + \mu_0 H_{const}\mathcal{I}_1 \\ & \left. -\eta' M_R\mu_0\mathcal{I}_1 + \mu_0\eta' M_R\bar{A} - \frac{\mu_0}{2}\mathcal{I}_2 \right) - \sigma_{const}\varepsilon \end{aligned} \tag{4.43}$$

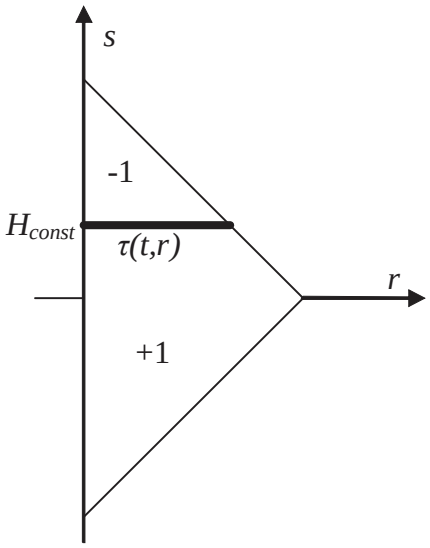

Figure 4-4: The global minimum Preisach boundary in the presence of a constant input.

where $\bar{A} = 2\int_0^\infty \int_{-\infty}^{\tau(t,r)} (s - H_{const})\mu(r,s)dsdr$. Using an argument similar to that for ψ_{Tot}, it can be shown that the following boundary minimizes the storage function:

$$\tau(t,r) = H_{const}. \tag{4.44}$$

This boundary is shown in Figure 4-4. For a constant input, this is the state of minimum energy. The magnetization in this state is the anhysteretic magnetization.

4.2.4 Energy-based velocity control of magnetostrictive materials

By comparing equations (4.1) and (4.24), the closed-loop output y is identified to be the time-derivative of the generalized displacement X. By using equation (4.12), we have

$$y = \begin{pmatrix} \dot{M} \\ \dot{\varepsilon} \end{pmatrix} \tag{4.45}$$

This relation implies that the closed loop in Figure 4-2 provides velocity control for the magnetostrictive actuator. In this subsection, a controller for this purpose is identified.

Any controller C satisfying conditions I and II with $\alpha_2 > 0$ in equation (4.11) provides a stable closed loop. For linear controllers, the following theorem can be used to prove condition II for positive real controllers:

Theorem 16 *[63, Lemma 91, page 353] Consider a linear controller C with transfer function $\hat{C}(s)$. Condition II is satisfied with $\beta_2 = 0$ and*

$$\alpha_2 = \inf_{\omega \in \mathbb{R}} \operatorname{Re} \hat{C}(j\omega). \tag{4.46}$$

In this thesis, a PID controller is used. PID controllers are simple, inexpensive and easy to build and implement. Using operational amplifiers (op-amps), inexpensive, high performance PID controllers with less than $1\,\mu$s response time can be built. In general, more sophisticated controllers need a PC-based control system. PC-based control systems are more flexible, but usually more expensive and difficult to set-up. The response time for a typical PC-based system is usually much higher than that of operational amplifiers.

An ideal PID controller does not satisfy condition I in equation (4.11). Consider a function $u(t)$ which is equal to $\cos \omega t$ for $0 \leq t \leq 1$ and zero elsewhere. The parameter ω is a positive real number. For every ω, $u(\cdot) \in L_2$ and $\|u\|_2$ is a finite number which is at most 1. For $\omega = 0$, if $u(t)$ is applied to an ideal integration denoted by transfer function $\frac{1}{s}$, the output will have infinite L_2 norm. For large values of ω, application of $u(t)$ to an ideal derivative with transfer function s will generate outputs with large L_2 norm. By increasing ω, the norm of the output can be made arbitrarily large. As a result, both integration and derivative terms violate condition I.

To overcome this problem, approximate integration and derivative with transfer functions $\frac{1}{s+\alpha}$ and $\frac{s}{\delta s+1}$, respectively, are used. The parameters α and δ are positive constants When α and δ are zero, ideal terms are obtained. For non-zero small values, the functions are close

to the ideal case, but the outputs will not have infinite L_2 norms. Approximate derivative has other advantages for numerical simulations and experimental implementations, such as more stability of the solutions and less noise level.

A PID controller with transfer function $\frac{K_I}{s+\alpha} + K_P + \frac{K_D s}{\delta s+1}$ satisfies condition I if α, $\delta > 0$. If K_I, K_P, $K_D > 0$, Theorem 16 can be used to show that condition II is also satisfied. In this subsection, such a PID controller is not used because it does not provide satisfactory performance.

The mentioned PID controller cannot provide zero steady-state error. To show this, assume that the steady-state error is zero. The controller output is almost a constant and hence, a constant input is applied to the actuator. This means zero output velocity. This implies that the reference input is zero. Thus, the PID controller cannot provide perfect tracking of non-zero velocities.

To provide better performance, the derivative term of the PID controller is replaced with an approximate double integration term. This gives the following controller for velocity control (See Figure 4-2):

$$\hat{C}e(s) = \begin{pmatrix} \left(\frac{K_I}{(s+\alpha)^2} + \frac{K_P}{s+\delta} + K_D\right)\dot{M}_e \\ 0 \end{pmatrix} \tag{4.47}$$

where K_P, K_I, K_D are the controller gains, α and δ are positive constants, $e = \begin{pmatrix} \dot{M}_e \\ -\dot{\varepsilon} \end{pmatrix} = r - y$, $r = \begin{pmatrix} \dot{M}_r \\ 0 \end{pmatrix}$ is the reference input, $d = \begin{pmatrix} \mu_0 H_{noise} \\ \sigma_{in} \end{pmatrix}$, H_{noise} is the controller noise, σ_{in} is the resultant stress from the external load applied to the actuator, and $\dot{M}_e = \dot{M}_r - \dot{M}$.

Theorem 17 *The controller proposed in (4.47) gives an L_2-stable closed loop for the magnetostrictive system if α and δ are positive and the controller transfer function $\hat{C}(s)$ satisfies the following inequality:*

$$\alpha_2 = \inf_{\omega \in \mathbb{R}} \operatorname{Re} \hat{C}(j\omega) > 0. \tag{4.48}$$

Proof. Since α and δ are positive, the controller satisfies condition I in equation (4.11) with $\beta_1 = 0$. Theorem 16 states that condition II is satisfied with $\alpha_2 > 0$. Theorem 14 proves that condition III is satisfied. Finally Theorem 10 implies L_2-stability for the closed-loop system. ■

It is difficult to use inequality (4.48) to develop a constraint on the controller gains for the general case. The following theorem can be used when $\alpha = \delta$.

Theorem 18 *Define*

$$N \triangleq \frac{(K_P\alpha + 3K_I)\alpha^2}{K_I - K_P\alpha}. \tag{4.49}$$

If $\alpha = \delta$, inequality (4.48) is satisfied if and only if the following inequalities are satisfied:

$$\begin{aligned} K_D &> 0, \\ \frac{K_I}{\alpha} + K_P &> 0, \end{aligned} \tag{4.50}$$

and at least one of

$$\begin{aligned} N &< 0, \\ K_I\frac{N-\alpha^2}{(N+\alpha^2)^2} &< K_P\frac{\alpha}{\alpha^2+N} + K_D. \end{aligned} \tag{4.51}$$

Thus, if the controller gains satisfy certain conditions, the closed-loop system is stable. In next chapter, the controller parameters are determined and the controller is evaluated experimentally.

4.3 Closed-loop control of hysteretic system represented by the Preisach model

In the previous section, an energy-based control approach for magnetostrictive materials was developed. In this section, a different approach to control the systems modeled by the Preisach

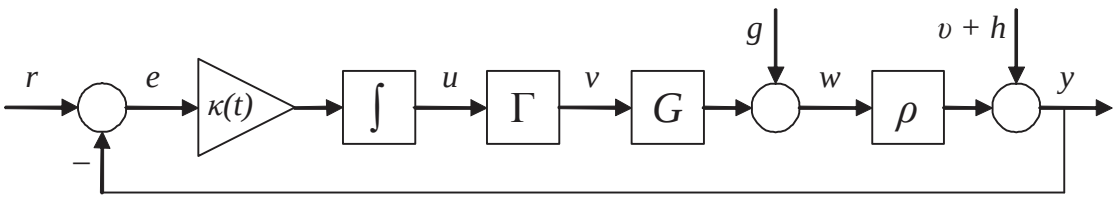

Figure 4-5: Integral control of a hysteretic system with input hysteresis [32].

model is used. Results on the performance of PI controllers are obtained. In Chapter 3, it was stated that magnetostrictive materials can be accurately represented by the Preisach model. The results in this section apply not only to magnetostrictive materials, but also to other hysteretic systems represented by the Preisach model.

In [31, 32], integral control of hysteretic systems is studied. Because of the similarity to the results presented here, some of the results in [31, 32] are reviewed in detail. Consider a hysteretic system controlled by an integrator as shown in Figure 4-5. In this figure, r is a constant reference signal, $\kappa(t)$ is a time-varying integration gain, Γ is a hysteresis operator, G is an L_2-stable linear bounded shift-invariant operator, $g \in L_2$ is included to model the effects of non-zero initial conditions, ρ is a static nonlinearity, υ is a constant, and h is a locally integrable function [32]. The following definitions are from [31, 32].

Define $\mathcal{C}(I)$ to be the set of continuous functions defined on $I \subset \mathbb{R}_+$. The numerical value set NVS Γ of a hysteresis operator Γ is defined as follows:

$$\text{NVS } \Gamma = \{(\Gamma u)(t) : u \in \mathcal{C}(\mathbb{R}_+), t \in \mathbb{R}_+\} \tag{4.52}$$

For a continuous function w defined on some interval $[0, a]$, define

$$\mathcal{D}(w,\delta,\gamma)=\left\{v\in\mathcal{C}([0,a+\gamma]):v(t)=w(t),\forall t\in[0,a],\sup_{t'\in[a,a+\gamma]}\left|v(t')-w(a)\right|\leq\delta\right\} \quad (4.53)$$

where γ and $\delta>0$ are real numbers.

Consider the following assumptions for the hysteresis operator Γ [32]:

(N1) Γ maps the set of real-valued locally absolutely continuous functions defined on $\mathbb{R}_+$ to itself.

(N2) For any locally absolutely continuous $u(t)$, $\left(\frac{d}{dt}\Gamma u\right)\left(\frac{d}{dt}u\right)\geq 0$ for all $t\in\mathbb{R}_+$.

(N3) There exists some $\lambda>0$ such that for all $a\geq 0$ and $w\in\mathcal{C}([0,a])$, there exists real numbers γ, $\delta>0$ such that for every u and v in $\mathcal{D}(w,\delta,\gamma)$

$$\max_{\tau\in[a,a+\gamma]}\left|(\Gamma u)(\tau)-(\Gamma v)(\tau)\right|\leq\lambda\max_{\tau\in[a,a+\gamma]}\left|u(\tau)-v(\tau)\right|. \quad (4.54)$$

(N4) For all $a>0$ and all $u\in\mathcal{C}([0,a))$, there exists $\beta>0$ such that for every $t\in[0,a)$

$$\max_{\tau\in[0,t]}\left|(\Gamma u)(\tau)\right|\leq\beta\left(1+\max_{\tau\in[0,t]}\left|u(\tau)\right|\right). \quad (4.55)$$

(N5) If $u\in\mathcal{C}(\mathbb{R}_+)$, $\lim_{t\to\infty}u(t)=\infty$, and for all $\varepsilon>0$, there exists $v\in\mathcal{C}(\mathbb{R}_+)$, such that

- for some $\tau\in\mathbb{R}_+$, v is non-decreasing on $[\tau,\infty)$
- $|u(t)-v(t)|<\varepsilon$, for all t

then $(\Gamma u)(t)$ and $(\Gamma(-u))(t)$ converge, as $t\to\infty$, to sup NVS Γ and inf NVS Γ, respectively.

(N6) If, for $u\in\mathcal{C}(\mathbb{R}_+)$, $\lim_{t\to\infty}(\Gamma u)(t)\in$ int NVS Γ, then u is bounded.

The assumption (N2) states that the hysteretic system is monotonic. The third assumption is similar to Lipschitz continuity for the hysteresis model.

Define $\hat{G}(s)$ to be the transfer function for G. Define $\hat{G}(0)$ as follows

$$\hat{G}(0) = \lim_{s \to 0, \mathrm{Re}\, s > 0} \hat{G}(s). \tag{4.56}$$

Assume that $\hat{G}(0)$ exists, $\hat{G}(0) > 0$ and

$$\limsup_{s \to 0, \mathrm{Re}\, s > 0} \left| \frac{\hat{G}(s) - \hat{G}(0)}{s} \right| < \infty. \tag{4.57}$$

Define $\mathcal{R}(G, \Gamma, \rho)$ as follows

$$\mathcal{R}(G, \Gamma, \rho) = \left\{ \rho\left(\hat{G}(0)v\right) : v \in \text{ NVS } \Gamma \right\}. \tag{4.58}$$

The following theorem is used to show tracking of a constant input.

Theorem 19 *[32] Assume that the following hold:*

(a) *The operator G is an L_2-stable linear bounded shift-invariant operator satisfying equation (4.57).*

(b) $g \in L_2$.

(c) *Assumptions (N1) - (N6) hold, where λ_1 is the constant associated with (N3).*

(d) *The function $\rho : \mathbb{R} \to \mathbb{R}$ is non-decreasing and globally Lipschitz with Lipschitz constant λ_2.*

(e) $r - \upsilon \in \mathcal{R}(G, \Gamma, \rho)$.

(f) $h \in L_2$ *and* $\int_0^\infty |h(t)|\, dt < \infty$ *and the function* $\int_t^\infty |h(\tau)|\, d\tau$ *is in* L_2.

(g) $\kappa : \mathbb{R}_+ \to \mathbb{R}_+$ *is measurable and bounded, satisfying the following relation*

$$\limsup_{t \to \infty} \kappa(t) < \frac{1}{\lambda_1 \lambda_2 \left(\underset{\omega \in \mathbb{R}}{ess\ inf} \mathrm{Re}\left(\frac{\hat{G}(i\omega)}{i\omega} \right) \right)} \tag{4.59}$$

In this relation, if the denominator is zero, we consider the inequality satisfied.

Then the closed loop has a unique solution u which is locally absolutely continuous on $\mathbb{R}_+$ and the following statements hold:

(i) $\frac{d}{dt}\Gamma u \in L_2$ *and the limit* $\Gamma^\infty = \lim_{t\to\infty}(\Gamma u)(t)$ *exists and is finite.*

(ii) *The signals* w *and* y *(see Figure 4-5) can be decomposed as* $w = w_1 + w_2$ *and* $y = y_1 + y_2$ *where* w_1, y_1 *are continuous and have finite limits*

$$w_1^\infty = \lim_{t\to\infty} w_1(t) = \hat{G}(0)\Gamma^\infty, \quad y_1^\infty = \lim_{t\to\infty} y_1(t) = \rho(\hat{G}(0)\Gamma^\infty) + \upsilon, \tag{4.60}$$

and w_2, $y_2 \in L_2$. *Under the additional assumption that*

$$\lim_{t\to\infty}\left[g(t) + (\Gamma u)(0)\left((G\theta)(t) - \hat{G}(0)\right)\right] = 0 \tag{4.61}$$

where $\theta(t) = 1$ *for all* $t \in \mathbb{R}_+$ *and*

$$\lim_{t\to\infty} h(t) = 0, \tag{4.62}$$

we have

$$\lim_{t\to\infty} w_2(t) = 0, \quad \lim_{t\to\infty} y_2(t) = 0. \tag{4.63}$$

(iii) *If the integral* $\int_0^\infty |k(t)|\,dt$ *diverges, then* $y_1^\infty = \lim_{t\to\infty} y_1(t) = r$ *and the error signal* $e = r - y$ *can be decomposed as* $e = e_1 + e_2$, *where* e_1 *is continuous with* $\lim_{t\to\infty} e_1(t) = 0$ *and* $e_2 \in L_2$. *If, (4.61) and (4.62) hold, then* $\lim_{t\to\infty} e(t) = 0$.

(iv) *if* $r - \upsilon$ *is an interior point of the set* $\mathcal{R}(G, \Gamma, \rho)$, *then* u *is bounded.*

It is seen that if certain assumptions are satisfied, for a constant input, the error $e = r - y$ goes to zero as $t \to \infty$. In [32], similar results for output hysteresis, that is when G precedes Γ in Figure 4-5, are presented.

Consider the closed-loop feedback system in Figure 4-6. The signals r_1 and r_2 are the reference input and controller noise, respectively. The operators G and Γ are defined previously. The following theorem considers a variable input.

Theorem 20 *[31] Assume that* G *is an* L_2*-stable linear shift invariant operator satisfying equation (4.57),* Γ *satisfies (N1) - (N5) with* $\lambda > 0$ *as the constant associated with (N3), and*

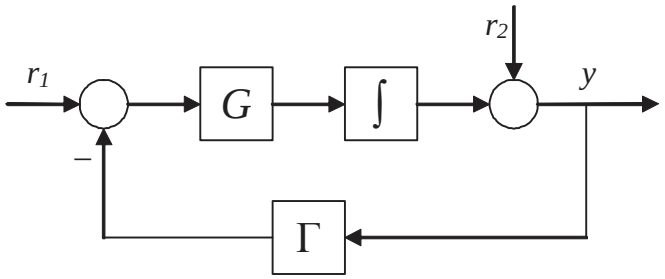

Figure 4-6: Integral control of a hysteretic system [31].

$0 \in$ *clos NVS* Γ. *Further assume that*

$$\inf_{w \in \mathbb{R}^*} \operatorname{Re} \frac{\hat{G}(i\omega)}{i\omega} > -\frac{1}{\lambda}, \tag{4.64}$$

where $\mathbb{R}^*$ *is the set of real numbers when 0 is excluded. Then for all* $r_1 \in L_2$ *and locally absolutely continuous* r_2 *with* $\frac{d}{dt} r_2 \in L_2$, $r_2(0) = y(0)$, *there exists a unique solution for the closed loop which is locally absolutely continuous on* $\mathbb{R}_+$. *Furthermore,* $\lim_{t \to \infty} (\Gamma y)(t) = 0$ *and there exists a constant* $\gamma > 0$ *(depending only on* G *and* λ, *but not on* r_1, r_2, *and the initial conditions for the closed loop) such that*

$$\|\Gamma y\|_\infty + \left\| \frac{d}{dt} \Gamma y \right\|_2 \leq \gamma \left(\|r_1\|_2 + \left\| \frac{d}{dt} r_2 \right\|_2 + |(\Gamma y)(0)| \right). \tag{4.65}$$

Under the additional assumption that (N6) holds and $0 \in$ *int NVS* Γ, y *is bounded.*

This theorem states that if certain conditions are held, the hysteretic system output is in some sense, bounded. Unfortunately, since mixed norms are used in equation (4.65), the results do not show any form of stability for the closed-loop system.

In the following subsection, a different approach is used to show tracking and establish stability of the closed loop. In the first subsection, assumptions are defined and discussed. In Subsection 4.3.2, the monotonicity results are used to develop an alternative passivity-based

velocity controller. Tracking of a constant input is covered in Subsection 4.3.3, and in Subsection 4.3.4, L_∞-stability of the closed loop is discussed.

4.3.1 Assumptions for the hysteretic system

Consider the closed-loop feedback system shown in Figure 4-2, where the plant is represented by a hysteresis model Γ. The hysteresis model input and output are denoted by u and y, respectively. The following assumptions are used:

(A1) For every continuous function $u(t)$, $y(t)$ is continuous.

(A2) (monotonicity) For all t, $\dot{u}(t)\dot{y}(t) \geq 0$.

(A3) (saturation) There exists some $u_{sat} > 0$ such that $\Gamma(u) = \Gamma(u_{sat})$ and $\Gamma(-u) = \Gamma(-u_{sat})$ for every $u \geq u_{sat}$.

(A4) Consider an arbitrary interval $[t_i, t_f]$. If for every $t \in [t_i, t_f]$, $u(t_i) \geq u(t)$, then $y(t_i) \geq y(t_f)$. Alternatively, if for every $t \in [t_i, t_f]$, $u(t_i) \leq u(t)$, then $y(t_i) \leq y(t_f)$.

Assumptions (A1) and (A2) are similar to assumptions (N1) and (N2), respectively. Define $\mathcal{C}^0$ to be the set of continuous functions on $\mathbb{R}$ and define $\mathcal{C}^1$ to be the set of continuously differentiable functions on $\mathbb{R}$ which have a continuous derivative. The following theorem shows that assumption (A4) is a stronger version of assumption (A2) for plants with differentiable input and output.

Theorem 21 *Consider a hysteresis model with input u and output $y = \Gamma u$. Assume that u, $y \in \mathcal{C}^1$. If assumption (A4) is satisfied, then assumption (A2) is satisfied.*

Proof. Assume that for some t, assumption (A2) is violated. This means that for this t,

$$\dot{u}(t)\dot{y}(t) < 0. \tag{4.66}$$

Assume that $\dot{u}(t) < 0$ and $\dot{y}(t) > 0$. (For the opposite case, the proof is similar.) Since u, $y \in \mathcal{C}^1$, we have $\dot{u}$, $\dot{y} \in \mathcal{C}^0$. Since $\dot{u}(t) < 0$, there exists a positive number $\delta_u(t)$ such that, for

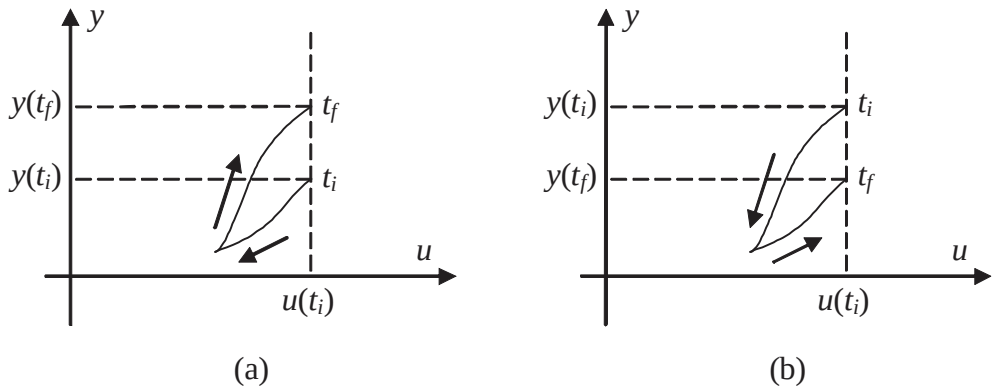

Figure 4-7: (a) A clockwise hysteresis loop, and (b) a counter-clockwise hysteresis loop.

every $\tau \in [t - \delta_u, t + \delta_u]$, $\dot{u}(\tau) < 0$. Similarly, there exists a positive number δ_y such that, for every $\tau \in [t - \delta_y, t + \delta_y]$, $\dot{y}(\tau) > 0$.

Define δ_m to be

$$\delta_m = \min(\delta_u, \delta_y). \tag{4.67}$$

Define $t_i = t - \delta_m$ and $t_f = t + \delta_m$. Clearly, for every $\tau \in [t_i, t_f]$, $\dot{u}(\tau) < 0$ and $\dot{y}(\tau) > 0$. In this interval, u is strictly decreasing. As a result, for every $\tau \in [t_i, t_f]$, $u(t_i)$ is greater than or equal to $u(t)$; but since in this interval, $\dot{y}(\tau) > 0$, we have $y(t_i) < y(t_f)$. This shows that assumption (A4) is violated. ■

The converse of Theorem 21 is not true. In Figure 4-7(a), a hysteretic system with a clockwise hysteresis loop is shown. This plant satisfies assumption (A2), but not (A4). In Figure 4-7(b), a plant with a counter-clockwise hysteresis loop is shown. Both assumptions (A2) and (A4) are satisfied.

The following theorems show that the Preisach model satisfies the assumptions under certain conditions:

Theorem 22 *[16] If the Preisach weight function $\mu(r,s)$ in equation (2.1) is bounded and piecewise continuous, then assumption (A1) holds.*

Theorem 23 *Assume that u, $y \in \mathcal{C}^1$. If the weight function $\mu(r,s)$ is nonnegative, assumption (A2) holds.*

Proof. Assume that at some arbitrary t, $\dot{u}(t) > 0$. (If $\dot{u}(t) < 0$, the proof is similar.)

Since $u \in \mathcal{C}^1$, $\dot{u}(\cdot)$ is a continuous function. Since $\dot{u}(t) > 0$, there exists a positive number $\delta_u(t)$ such that, for every $\tau \in [t - \delta_u, t + \delta_u]$, $\dot{u}(\tau) > 0$. In this interval, u is strictly increasing.

Consider a Preisach relay as shown in Figure 2-2. Since u is strictly increasing, no Preisach relay goes from $+1$ state to -1 state. Some Preisach relays might go from -1 state to $+1$ state.

Pick $\gamma < \delta_u$ to be an arbitrary positive real number. Define Ω_+ to be the set of Preisach relays which are in -1 state at time t and $+1$ state at time $t + \gamma$. From the definition of the Preisach model we have

$$y(t+\gamma) = y(t) + 2 \int \int_{\Omega_+} \mu(r,s) dr ds. \tag{4.68}$$

Since $\mu(r,s) \geq 0$, we have

$$y(t+\gamma) \geq y(t). \tag{4.69}$$

Since $\gamma > 0$,

$$\frac{y(t+\gamma) - y(t)}{\gamma} \geq 0. \tag{4.70}$$

Taking the limit $\gamma \to 0$,

$$\lim_{\gamma \to 0^+} \frac{y(t+\gamma) - y(t)}{\gamma} = \dot{y}(t) \geq 0. \tag{4.71}$$

If $\dot{y}(t) \geq 0$, then $\dot{u}(t)\dot{y}(t) \geq 0$. A similar proof can be used when $\dot{u}(t) < 0$. ■

Theorem 24 *If the weight function $\mu(r,s)$ is zero when $r+s$ or $r-s$ is larger than some value $u_{sat} > 0$, then assumption (A3) holds.*

Proof. Assume that

$$u(t) \geq u_{sat}. \tag{4.72}$$

Any Preisach relay (r, s) with a non-zero weight function $\mu(r, s)$ satisfies

$$s + r < u_{sat}, \tag{4.73}$$

and

$$s - r > -u_{sat}. \tag{4.74}$$

By combining equations (4.72) and (4.73), we have

$$s + r < u(t). \tag{4.75}$$

By comparing with Figure 2-2, it is seen that all relays with non-zero weight function are in $+1$ state. If $u = u_{sat}$, by using equation (4.73) and Figure 2-2, the same result is obtained and

$$\Gamma(u_{sat}) = \Gamma(u), \tag{4.76}$$

for any $u \geq u_{sat}$. Using a similar argument and equation (4.74), it can be shown that $\Gamma(-u_{sat}) = \Gamma(-u)$. This concludes the proof. ■

Theorem 25 *If the weight function $\mu(r, s)$ is nonnegative, assumption (A4) holds.*

Proof. Assume that for every $t \in [t_i, t_f]$, $u(t_i)$ is greater than or equal to $u(t)$. Define Ω_+ to be the set of Preisach relays that are in -1 state at t_i and $+1$ state at t_f. Define Ω_- to be the set of Preisach relays that are in $+1$ state at t_i and -1 state at t_f. From the definition of the Preisach model,

$$y(t_f) - y(t_i) = 2 \int \int_{\Omega_+} \mu(r, s) dr ds - 2 \int \int_{\Omega_-} \mu(r, s) dr ds. \tag{4.77}$$

From t_i to t_f:

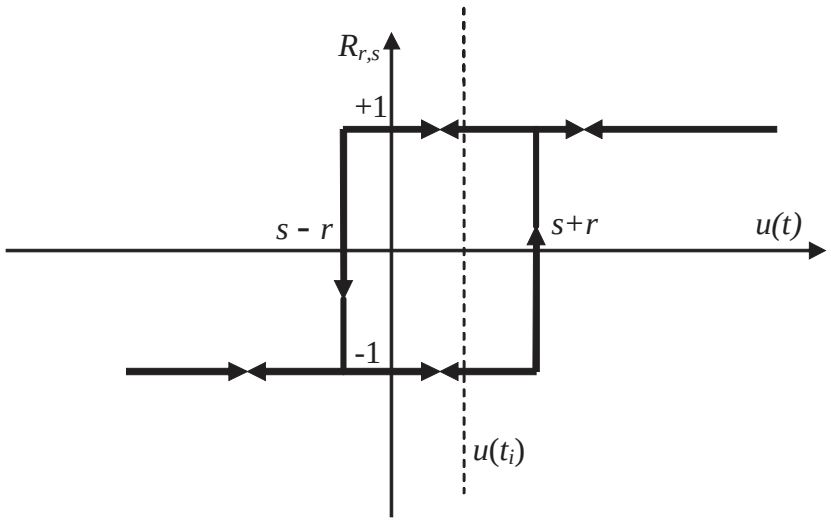

Figure 4-8: Preisach relays with $s + r > u(t_i)$.

- For relays with $s + r > u(t_i)$: as seen in Figure 4-8, a transition from -1 to $+1$ cannot happen because for no t, $s + r = u(t)$. These relays cannot be in Ω_+.
- For relays with $s + r < u(t_i)$: as seen in Figure 4-9, at $t = t_i$, all of these relays are in $+1$ state. None of these relays can be in Ω_+.

Thus, Ω_+ is an empty set. Since $\mu(r, s) \geq 0$, the integrals in equation (4.77) are non-negative.

$$y(t_f) - y(t_i) = -2 \int \int_{\Omega_-} \mu(r, s) dr ds \leq 0. \tag{4.78}$$

It means that

$$y(t_i) \geq y(t_f). \tag{4.79}$$

If for every $t \in [t_i, t_f]$, $u(t_i)$ is less than or equal to $u(t)$, using a similar argument, it can be shown that $y(t_i)$ is less than or equal to $y(t_f)$. ■

For many hysteretic systems, the weight function $\mu(r, s)$ is nonnegative [18, 49, 62]. Most

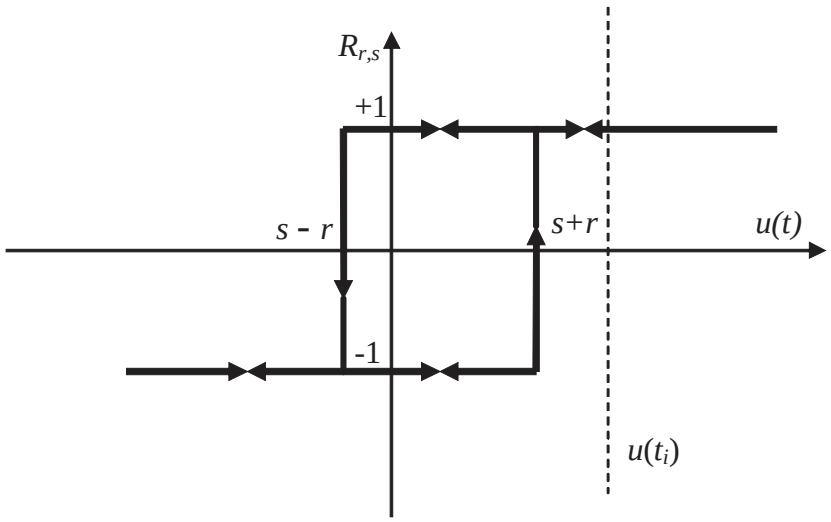

Figure 4-9: Preisach relays with $s + r < u(t_i)$.

smart materials also exhibit saturation [18, 49, 62] and hence, assumptions (A1) – (A4) hold.

4.3.2 Monotonicity-based passivity of the systems represented by the Preisach model

In this subsection, an alternative passivity-based velocity controller is proposed. This passivity result is based on the monotonicity of the Preisach model and can be used for any system represented by this model.

Consider a Preisach model with input $v(t)$ and output $w(t)$. In the previous subsection, it was shown that for all t, $\dot{v}(t)\dot{w}(t) \geq 0$. By comparing this result with the definition of passivity in equation (4.1), it can be seen that the system is passive with the following choice of input and output:

$$\begin{aligned} u &= \dot{v} \\ y &= \dot{w} \end{aligned} \tag{4.80}$$

when the storage function $S(x) = 0$. Consequently, condition III in Theorem 10 is satisfied with $\alpha_3 = 0$ and $\beta_3 = 0$.

Similar to the previous velocity controller, any controller satisfying conditions I and II in Theorem 10 with $\alpha_2 > 0$ provides a stable closed loop. As stated before, PID controllers have many advantages. Consider the following PID controller:

$$\hat{C}(s) = \frac{K_I}{s+\alpha} + K_P + \frac{K_D s}{\delta s + 1}. \tag{4.81}$$

Approximate derivative and integration are used to satisfy condition I. As stated before, if K_I, K_P, K_D, α, and $\delta > 0$, condition II is satisfied with $\alpha_2 = K_P$. Theorem 10 states that this controller provides an L_2-stable closed loop.

Using equation (4.80), the Preisach model input $v(t)$ can be obtained.

$$v(t) = \left(\frac{K_I}{s(s+\alpha)} + \frac{K_P}{s} + \frac{K_D}{\delta s + 1} \right) e(s), \tag{4.82}$$

where $e = r - y$. By comparing with equation (4.47), it can be seen that the controllers are similar. From e to the hysteresis model input, both controllers have a double integration term and no derivative term. The only difference is the stability conditions. For the previous controller, equations (4.48), (4.50), and (4.51) should be satisfied. For this controller, any positive K_I, K_P, K_D, α, and δ provides stability. Since the stability conditions are more relaxed, better controllers are expected from the new velocity control approach. In the next chapter, controller parameters are determined and the controller is examined experimentally.

The monotonicity assumption (A2) is satisfied by many hysteretic systems [30]. As a result, the velocity controller developed here is not limited to the Preisach model.

4.3.3 Tracking properties of position controllers for the Preisach model

In this subsection, a PI controller is shown to provide position control for a hysteretic system represented by the Preisach model. Tracking properties of the closed loop are examined for a constant input.

Consider a Preisach model Γ with input u and output y as the plant in Figure 4-2. The following PI controller is used for position control:

$$\hat{C}(s) = \frac{K_I}{s} + K_P \tag{4.83}$$

where K_I and K_P are constants. Consider the following assumptions:

(B1) For the controller in (4.83), $K_P \geq 0$ and $K_I > 0$.

(B2) The plant input $u(t)$ and the reference signal $r(t)$ are continuous functions of time.

Continuity of $u(t)$ is needed for the Preisach model. Continuity of $r(t)$ is included to ensure continuity of $u(t)$.

For position control, the controller noise d in Figure 4-2 is not considered ($d = 0$). The closed-loop system shown in Figure 4-2 is described by the following equations:

$$\begin{aligned} e(t) &= r(t) - y(t) && (4.84)\\ f(t) &= \int_0^t e(t')dt' && (4.85)\\ u(t) &= K_P e(t) + K_I f(t) && (4.86)\\ y(t) &= \Gamma\left[u(\cdot)\right](t) && (4.87) \end{aligned}$$

The following theorems establish tracking properties of the proposed controller for a constant input:

Theorem 26 *Assume that r is a constant and assumptions (A1), (A2), (B1) and (B2) hold. If for some t_0 and ρ, $|r - y(t_0)| \leq \rho$, then $|r - y(t)| \leq \rho$ for all $t \geq t_0$.*

Proof. Consider the function

$$V = (r - y)^2. \tag{4.88}$$

The state of the system is implicitly included in y. Note that $V \geq 0$. The time-derivative of V is

$$\begin{aligned} \dot{V} &= 2(r - y)(-\dot{y}) \\ &= -2e\dot{y}. \end{aligned} \tag{4.89}$$

By taking time-derivative of equation (4.86), we have

$$\dot{u} = K_P\dot{e} + K_I e. \tag{4.90}$$

Since $K_I \neq 0$, by combining equations (4.89) and (4.90), the following result is obtained:

$$\begin{aligned} \dot{V} &= -2\dot{y}\frac{\dot{u} - K_P\dot{e}}{K_I} \\ &= -\frac{2}{K_I}\dot{u}\dot{y} + \frac{2K_P}{K_I}\dot{y}\dot{e}. \end{aligned} \tag{4.91}$$

Equation (4.84) implies $\dot{e} = -\dot{y}$ and so

$$\begin{aligned} \dot{V} &= -\frac{2}{K_I}\dot{u}\dot{y} - \frac{2K_P}{K_I}\dot{e}^2 \\ &\leq -\frac{2}{K_I}\dot{u}\dot{y} \end{aligned} \tag{4.92}$$

since K_P and K_I are non-negative. Assumption (A2) states that $\dot{u}\dot{y} \geq 0$. As a result, $\dot{V} \leq 0$.

Since $\dot{V} \leq 0$, the function $V = (r - y)^2$ is non-increasing. Consequently, $|r - y|$ is non-

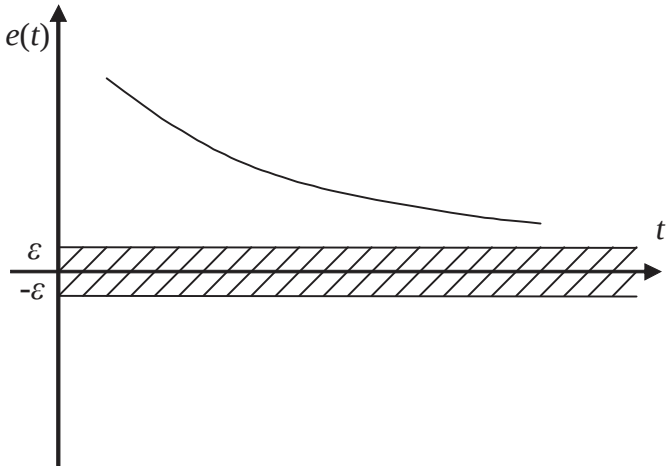

Figure 4-10: The error $e(t)$ versus time.

increasing. If $|r - y(t)| \leq \rho$ at some point $t = t_0$, $|r - y(t)| \leq \rho$ for all $t \geq t_0$. ■

Theorem 26 states that the absolute value of the error is never increased. The following theorem proves that under certain conditions, the error can be made arbitrarily small.

Theorem 27 *Let t_0 be a non-negative real number. Assume that $r(t)$ is a constant in $[t_0, \infty)$ and assumptions (A1), (A2), (A3), (B1), and (B2) hold. If $\Gamma(-u_{sat}) \leq r \leq \Gamma(u_{sat})$, then for every $\varepsilon > 0$,*

$$|r - y(t)| \leq \varepsilon, \forall t \geq \bar{t} + t_0, \tag{4.93}$$

where

$$\bar{t} = \frac{\frac{u_{sat}}{K_I} + |f(t_0)|}{\varepsilon}. \tag{4.94}$$

Proof. Assume that for some ε and t, $r - y(t) > \varepsilon$ when $t \geq \bar{t} + t_0$. (For $y(t) - r > \varepsilon$, the proof is similar.)

Theorem 26 implies that for all $t' \in [t_0, t]$,

$$\left|r - y(t')\right| = \left|e(t')\right| > \varepsilon. \tag{4.95}$$

From assumptions (A1) and (B2), $y(t)$ is continuous. Since r is constant, $e(\cdot)$ is continuous in $[t_0, \infty)$. As illustrated in Figure 4-10, a region around zero is excluded by equation (4.95) in $[t_0, t]$. Since $e(\cdot)$ is continuous and $e(t) = r - y(t) > \varepsilon$, $e(\cdot)$ has to be larger than ε in $[t_0, t]$:

$$e(t') > \varepsilon, \forall t' \in [t_0, t]. \tag{4.96}$$

By integrating from t_0 to $t_0 + \bar{t}$, where $t \geq t_0 + \bar{t}$, we have

$$\int_{t_0}^{t_0+\bar{t}} e(t')dt' \geq \varepsilon\bar{t}. \tag{4.97}$$

By using equation (4.85), the following result is obtained:

$$f(t_0 + \bar{t}) \geq f(t_0) + \varepsilon\bar{t}. \tag{4.98}$$

Equation (4.94) implies that

$$\varepsilon\bar{t} \geq \frac{u_{sat}}{K_I} - f(t_0). \tag{4.99}$$

Using equation (4.98), we have

$$f(t_0 + \bar{t}) \geq \frac{u_{sat}}{K_I}. \tag{4.100}$$

Since $t \geq \bar{t} + t_0$, equation (4.96) states that

$$e(t_0 + \bar{t}) > \varepsilon. \tag{4.101}$$

By using equation (4.86), a bound on $u(t_0 + \bar{t})$ can be obtained:

$$u(t_0 + \bar{t}) \geq K_P\varepsilon + u_{sat} \geq u_{sat}. \tag{4.102}$$

Using assumption (A3), $y(t_0+\bar{t}) = \Gamma(u_{sat})$. From equation (4.101), $e(t_0+\bar{t}) = r-y(t_0+\bar{t}) > 0$ or,

$$r > \Gamma(u_{sat}). \tag{4.103}$$

Similarly, if $y(t) - r > \varepsilon$, then $r < \Gamma(-u_{sat})$. Hence, $|r - y(t)| \leq \varepsilon$ as to be shown. ■

Theorem 27 gives an upper limit for the time required to achieve any accuracy ε. The following is an immediate result of Theorem 27.

Corollary 28 *Assume that r is a constant and assumptions (A1), (A2), (A3), (B1) and (B2) hold. If $\Gamma(-u_{sat}) \leq r \leq \Gamma(u_{sat})$ then $\lim_{t\to\infty} y(t) = r$.*

Proof. Let t_0 be zero. Theorem 27 states that for every $\varepsilon > 0$, there is a $\bar{t}$ such that $|r - y(t)| \leq \varepsilon$ for all $t \geq \bar{t}$. This is the definition of limit. Thus, $\lim_{t\to\infty} y(t) = r$. ■

Corollary 28 states that if the input to the closed loop is reasonable, zero steady-state error is guaranteed.

Unlike the results in [32], the results here do not include a linear portion denoted by G. Instead of an integral controller in [32], a PI controller is used. Here, fewer, simpler, and less strict assumptions are required for tracking. Also, some information about the trajectories of the solutions are given, and an upper bound for the time required for achieving any desired accuracy was obtained.

4.3.4 L_∞-stability of the closed-loop system for position control

In the previous subsection, a constant reference input is studied. Here, a variable input is considered and L_∞-stability of the closed loop is established when the controller is described by equation (4.83).

The following theorem is used to establish L_∞-stability of the closed loop:

Theorem 29 *Assume that assumptions (A1), (A4), (B1) and (B2) hold and* $r \in L_\infty$. *Further, assume that* $u(0) = 0$. *If* $|y(0)| \leq \|r\|_\infty$, *then* $\|y\|_\infty \leq \|r\|_\infty$.

Proof. This is for $K_P > 0$. The case $K_P = 0$ is similar and is in Appendix B. Define L to be

$$L = \|r\|_\infty . \tag{4.104}$$

Assume that for some t_f,

$$y(t_f) > L. \tag{4.105}$$

Define $t_{\max u}$ to be the time at which $u(t)$ is maximized on $[0, t_f]$:

$$u(t_{\max u}) \geq u(t), \forall t \in [0, t_f]. \tag{4.106}$$

Define $t_{\max f}$ to be the time at which $f(t)$ defined in equation (4.85) is maximized on $[0, t_f]$:

$$f(t_{\max f}) \geq f(t), \forall t \in [0, t_f]. \tag{4.107}$$

Using assumption (A4) and equation (4.106), we have:

$$y(t_{\max u}) \geq y(t_f). \tag{4.108}$$

Using equation (4.105), we have:

$$e(t_{\max u}) = r(t_{\max u}) - y(t_{\max u}) < 0. \tag{4.109}$$

Using assumptions (A1) and (B2), $y(t)$ is continuous. By using assumption (B2) again, it is found that $e(t)$ is continuous. Equations (4.104) and (4.105) imply that $e(t_f) < 0$. Using continuity of $e(t)$, there is a neighborhood around t_f at which, $e(t) < 0$. Since $\dot{f}(t) = e(t)$, f is strictly decreasing in this neighborhood. As a result, $f(t)$ is not maximized at t_f:

$$t_{\max f} \neq t_f. \tag{4.110}$$

Since $e(t)$ is continuous and $\dot{f}(t) = e(t)$, $f(t)$ is continuously differentiable. If $t_{\max f} \neq 0$, maximization of $f(t)$ at $t_{\max f}$ implies that $\dot{f}(t_{\max f}) = 0$ or,

$$e(t_{\max f}) = 0, \text{ if } t_{\max f} \neq 0 \tag{4.111}$$

or

$$t_{\max f} = 0, \text{ if } e(t_{\max f}) \neq 0. \tag{4.112}$$

By definition of $t_{\max u}$,

$$u(t_{\max u}) \geq u(t_{\max f}). \tag{4.113}$$

Using equation (4.86),

$$K_I f(t_{\max u}) + K_P e(t_{\max u}) \geq K_I f(t_{\max f}) + K_P e(t_{\max f}). \tag{4.114}$$

By definition of $t_{\max f}$,

$$f(t_{\max f}) \geq f(t_{\max u}). \tag{4.115}$$

Since K_I, $K_P > 0$, using equation (4.114) we have:

$$e(t_{\max u}) \geq e(t_{\max f}). \tag{4.116}$$

By comparing with equation (4.109), we have

$$e(t_{\max f}) < 0. \tag{4.117}$$

Using equation (4.112),

$$t_{\max f} = 0. \tag{4.118}$$

From equation (4.85), $f(0) = 0$. By using equation (4.86), we have

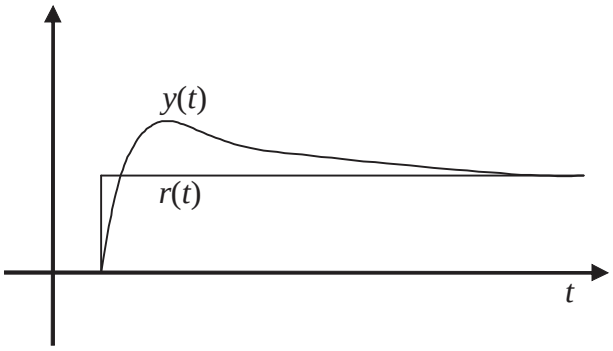

Figure 4-11: An example of an overshoot.

$$u(0) = K_P e(0) < 0. \tag{4.119}$$

Similarly, if $y(t_f) < -L$, $u(0) > 0$. Thus $u(0) = 0$ implies that $\|y\|_\infty \leq \|r\|_\infty$. ■

Theorem 29 implies that an overshoot, like the one shown in Figure 4-11, cannot be seen in the closed-loop response of the system. In Figure 4-11, clearly the L_∞ norm of y is more than that of r. This response violates Theorem 29 and hence, cannot exist.

Corollary 30 *Assume that assumptions (A1), (A4), (B1) and (B2) hold. The closed loop system is L_∞-stable.*

Proof. Assume that $r \in L_\infty$. For a zero initial condition, Theorem 29 states that $\|y\|_\infty \leq \|r\|_\infty$. It means that y has a bounded L_∞ norm and hence, is a member of L_∞. The closed loop is L_∞-stable. ■

Corollary 30 can be used to design a controller for position control. The controller must satisfy assumption (B1). In the next chapter, a position controller is obtained and evaluated experimentally.

The results presented here and in [31] assume similar structures for the plant. Here, a PI controller is chosen while in [31], a linear transfer function in series with an integrator is used. Similar to the previous subsection, the results presented here have fewer, simpler, and less strict assumptions. L_∞-stability of the closed loop is shown. Also, some information about the trajectories of the solutions is obtained. In particular, there is no overshoot.

In the next chapter, the experimental apparatus used in this thesis is explained. The overall structure, different components and sensors are discussed and the controllers proposed here are evaluated experimentally.

Chapter 5

Experimental evaluation of controllers for magnetostrictive actuators

To obtain experimental hysteresis curves for Terfenol-D and to evaluate the controllers presented in the previous chapter experimentally, a test rig has been designed and built. In this chapter, the design of its different parts is briefly explained. This test rig was originally developed in the candidate's master's thesis [57]. Several upgrades and additional experiments have been done with this setup and the results are included in this thesis.

In this chapter, the controllers from the previous chapter are optimized, tested in practice and discussed. In the first section, an overview of the test rig is presented. Different components of the setup are explained in Section 2. In Section 3, the optimization and evaluation process is discussed. Section 4 covers energy-based velocity controllers. The monotonicity-based velocity controller is included in Section 5, and in Section 6, position control is discussed.

5.1 Test rig overview

A test rig (Figure 5-1) is designed to measure different parameters of a Terfenol-D rod under different stresses and magnetic conditions. For this purpose, a rod made of Terfenol-D is put under compression. This compression is supplied by a set of washer springs. The springs are soft enough that it can be assumed that the compression force is constant when the Terfenol-D rod changes size. The force of the springs can be adjusted by a bolt on top of the test rig. The test rig and all its components are installed on a heavy granite table. This table ensures that the setup is not affected by external vibrations. The Terfenol-D rod is surrounded by a magnetic coil which supplies the desired magnetic field. Different sensors are included to measure elongation, force, flux density and temperature.

Figure 5-2 shows the block diagram of the setup. The measurements made by the sensors are fed to a data acquisition card after being amplified by an electronic circuit. The data acquisition card is installed on a computer running Simulink, with which the measurements are recorded. The simulink model can also send commands to the power supply unit through the data acquisition card. The power supply feeds the magnet surrounding the Terfenol-D rod. For more information see [57].

Since the candidate's master's thesis, the following upgrades have been done on the spring assembly and power supply unit. The spring assembly has been modified to have less friction by eliminating rubbing parts. Friction in the spring assembly causes fluctuations in the force applied to the actuation unit. The new design has a lower friction which is almost negligible. It is shown that this upgrade decreased the fluctuations by 90%.

It was observed that the original power supply unit had an internal delay of about 30 ms. For high performance control applications, this delay can cause instability. For these experiments, the power supply was replaced by a unipolar power supply with less delay. The new power supply has a switching frequency of 125 kHz, which is much higher that that of the old power supply (22 kHz). Improved closed-loop stability was observed with the new power supply.

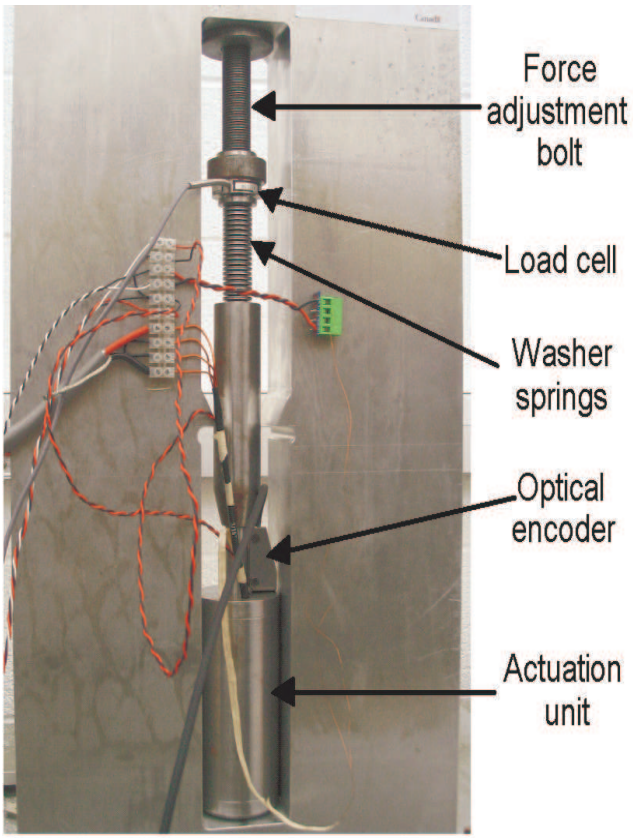

Figure 5-1: The test rig.

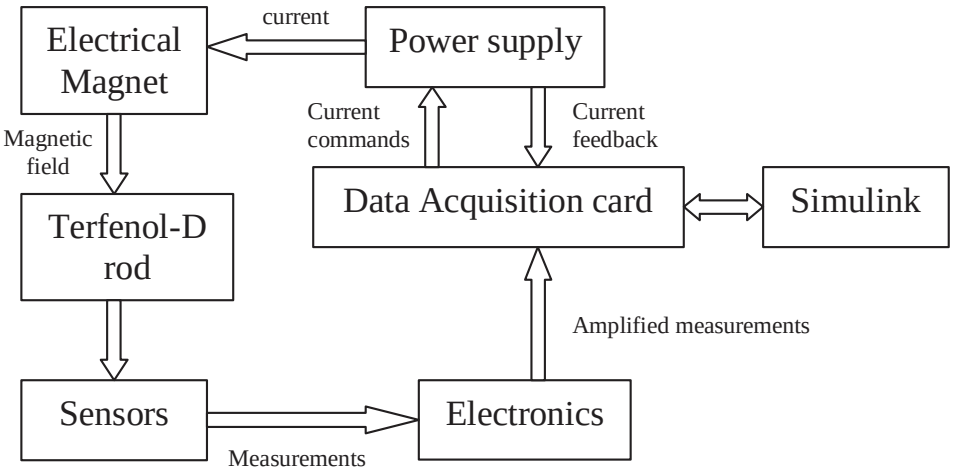

Figure 5-2: The block diagram of the test rig

5.2 Test setup design

5.2.1 Actuation unit

The actuation unit consists of the Terfenol-D rod and the excitation electrical magnet. There are many different shapes of Terfenol-D commercially available for different purposes. In this setup, a round rod with a length of 10 cm and a diameter of 10 mm is used.

The simplest way to apply a magnetic field to the Terfenol-D sample is to use the rod in a solenoid as shown in Figure 5-3. Here, the magnetic field path is shown with a dashed line. For the electrical magnet winding, 940 turns of insulated magnet wire size 18 is chosen. Since a strong magnetic field is required to saturate Terfenol-D, high electrical current may be used in the electrical magnet. In this case heat generated by this current might become important. The wire has a diameter of 1.12 mm and can withstand temperatures up to 180 °C. This wire is wound on a tube made of phenolic. The Terfenol-D rod lies inside this tube as seen in Figure 5-3. Phenolic is chosen because of its neutral magnetic properties and its ability to resist high temperature. The electrical magnet has an electrical resistance of 1.87 Ω. It is shown that this

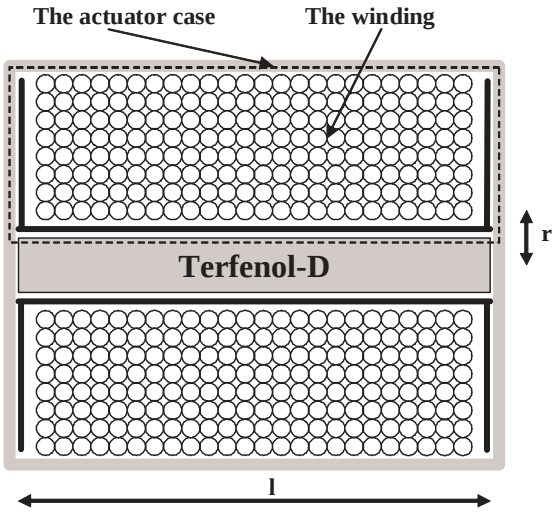

Figure 5-3: Cross-section of the solenoid.

electrical magnet can hold Terfenol-D in its saturated state with a flux density of 0.8 T and current of 19.1 A for about 20 seconds. This period of time is long enough for most experiments.

If the magnet is used with alternating current, its inductance is important. The inductance is measured to be 7.04 mH. Using the resistance of the magnet coil, the time constant is computed to be 3.52 milliseconds. This time constant is negligible in this application. In Figure 5-4, the magnet is shown in its final state.

It is obvious from Figure 5-3 that some part of the magnetic path goes through the case

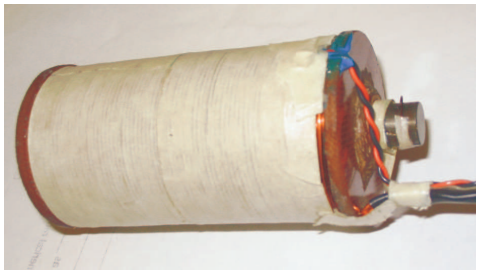

Figure 5-4: The main magnet with the Terfenol-D rod inside.

of the solenoid. The case is made of an iron alloy. Residual flux density could be a concern since almost all iron alloys are permanent magnets to some extent. This residual flux density is imposed on the Terfenol-D rod even when there is no current in the wire winding; and it can make the analysis and control of the system more complicated. However, residual flux density linearly depends on the coercive force of the material used. To have a minimal residual flux density, pure iron is chosen for the solenoid case. Pure iron has a small coercive force that results in a negligible residual flux density.

Unfortunately, pure iron is not commercially available in any shape. For this setup, pure iron powder was used to make a block of pure iron by powder metallurgy. This block was cut and machined to produce the desired parts. A small part of this block was shaped like a small ring. The magnetic properties of this ring was evaluated by the Rowland ring experiment [35]. The coercive force was measured to be $250\frac{\mathrm{A}}{\mathrm{m}}$, which is about half of the coercive force of commercially available iron ($550\frac{\mathrm{A}}{\mathrm{m}}$). The coercive force is much higher than its expected value for pure iron ($4\frac{\mathrm{A}}{\mathrm{m}}$). A possible cause of this would be the presence of carbon contents, possibly from the resin used in the powder metallurgy process.

5.2.2 The frame

The frame holds all pieces of the setup together and provides the compressive force for the Terfenol-D rod. The frame is made of aluminum. Iron might be a better choice for the frame because it is stronger, but it could not be used because of its magnetic interference with the actuation unit. A part of the magnetic flux lines could go through the frame and other components such as the load cell, etc. The frame is made out of a 6.5 cm thick aluminum plate.

Since total displacement of the actuator unit is quite small, it is very important that different components are held firmly in their places during the experiment; otherwise, no displacement might be seen by the sensors. The frame is designed rigid enough that the elongation of the frame is reasonably small. To verify this design, the frame was simulated using the finite element method. Finite element simulations were done in FEMLAB. It was shown that this frame could provide the requested rigidity under different loading conditions [57].

5.2.3 Power supply unit

The core of the power supply unit is a servo-amplifier from Advanced Motion Controls, brush type, model 25A20. This servo-amplifier, when correctly configured, can act like a programmable current source. Since controlling the magnetic field is desired, current should be controlled. A programmable current source is the best choice. This servo-amplifier is a pulse width modulation (PWM) amplifier with switching frequency of 22 kHz. This amplifier is the most important source of noise in this setup. Generating high frequency noise is an intrinsic property of any PWM amplifier, but because of their efficiency and low price, most existing amplifiers are PWM type. This amplifier is directly controlled by a computer. Output current of this amplifier is measured inside the amplifier and the result is sent back to the computer.

For control applications where the delay introduced by the power supply is important, this power supply unit was replaced by a programmable power supply, model XPD33-16 from Xantrex Technology Inc. The power supply is programmed as a current source. The desired current is sent from the data acquisition card to the power supply directly. The actual current in the circuit is measured inside the power supply and sent back to the data acquisition card.

5.2.4 Sensors and amplifiers

An optical encoder measures the displacement of the actuator, a flux density sensor measures the flux density B inside Terfenol-D rod, two temperature sensors measure the temperature of the Terfenol-D rod and the magnet windings, a load cell measures the force applied to the Terfenol-D rod and finally, an electronic circuit inside the power supply unit measures the current.

The displacement sensor is an optical encoder from Renishaw Inc. The encoder consists of two parts: the readhead and the interpolator unit. The readhead should be held against a gold tape which has a fringe pattern on it. The relative motion between the readhead and the gold tape is measured. The interpolator unit converts analog signals from the readhead to a digital RS-422 signal. The data acquisition card used in this setup has inputs for RS422 signals. A

few control signals are also sent from the interpolator to the data acquisition card. The encoder has a resolution of 10 nm.

Measuring the flux density inside Terfenol-D rod was a challenging task. Most existing flux density sensors need to be placed inside the field. i.e. the magnetic field flux lines should go through the sensor. It is practically impossible to install such a sensor inside the Terfenol-D rod. The flux density sensor could be installed somewhere else inside the magnetic circuit. In this case, the flux density inside Terfenol-D rod is measured indirectly. But this solution is not practical because of the high magnetic reluctance of the sensor. If the sensor is installed inside the magnetic circuit, the ability of having strong magnetic fields inside Terfenol-D rod is severely limited.

In this setup, a secondary coil is wound around the Terfenol-D rod. The winding should be as close as possible to the Terfenol-D rod. In this case, the flux density inside the rod can be measured if the voltage difference across the secondary coil is available [57]. This method seems to be the only solution, but it has one major disadvantage. The flux density is not directly measured; the rate of change of flux density is measured. In order to find the flux density, one has to integrate the voltage measured across the secondary coil. For this purpose, an electronic integrator circuit was used. This sensor is calibrated as explained in [57].

Two temperature sensors are installed. One of them is installed on the main coil. Since the current in the main coil is high, it is desirable to have its temperature measured, so the operator could be notified if the coil is too hot. The other temperature sensor is installed on the Terfenol-D rod. Since the displacement is in range of a few nanometers, thermal expansion plays an important role. If the temperature of the Terfenol-D rod is available, the effects of thermal expansion can be compensated. The outputs of temperature sensors are amplified by two instrumentational amplifiers and sent to the computer.

The load cell is a compression-only load cell from Transducer Techniques Inc. This load cell is capable of measuring up to 250 lbf. Load cell output is also amplified by an instrumentation amplifier. Amplified results are sent to the computer.

5.3 Optimization of the controllers

From the previous chapter, for each controller, a transfer function with a few free parameters, and a set of inequalities for the parameters are available. Any set of parameters that satisfy the inequalities provide a stable closed loop.

In this chapter, a set of parameters for each controller is obtained. The parameters satisfy the stability inequalities and provide an optimal performance. Several definitions for performance are available. In this chapter, tracking performance is used; that is, an optimal set of controller parameters should minimize the following cost function subject to the stability constraints:

$$J = \int_{t_1}^{t_2} (y - r)^2 dt, \tag{5.1}$$

where r is the reference input, y is the closed-loop output and $[t_1, t_2]$ is the time range of interest. The reference signal r is a step signal. A smaller J means a closer match between the actual and desired outputs.

Because of the nonlinearity and complex structure of the system, the only method for minimizing J is numerical optimization. For this purpose, the closed-loop is simulated by using a Preisach model with a general weight function. The model is identified in [62, 57]. Using the Preisach model, y is computed as a function of controller parameters. The cost function J is numerically minimized using Nelder-Mead simplex direct search method [7]. The optimal model parameters are tested experimentally for different reference signals and the results are discussed.

5.4 Energy-based velocity control

In the previous chapter, the stability of the closed-loop system was established when $\dot{M}$ is being controlled. In most applications the control of mechanical variables is requested. For this reason, the relation between magnetization and elongation of Terfenol-D is examined here.

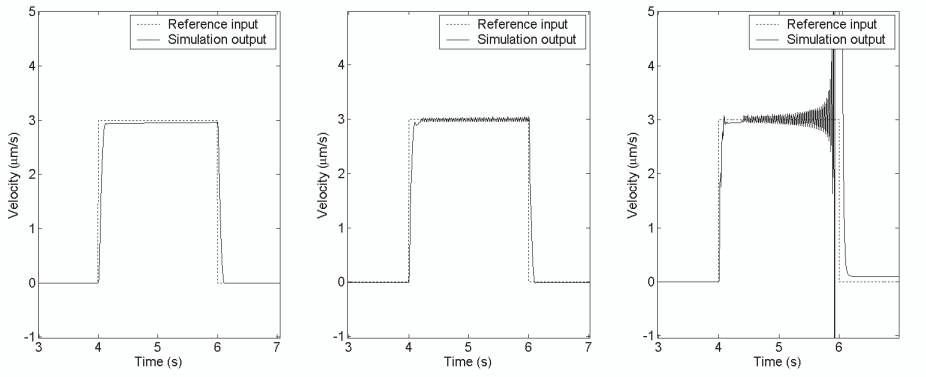

Figure 5-5: The controlled system response for $K_P = K_c$ (left), $K_P = 2K_c$ (middle) and $K_P = 3K_c$ (right). $K_c = 1,580,200$.

Figure 3-2 shows magnetostriction versus magnetization at different stress levels for Terfenol-D. At each stress level, there exists an algebraic relation between elongation and magnetization. It is also seen that except a dead-zone in the middle, a linear relation is seen between elongation and magnetization, and the slope is almost stress independent. This behaviour can be used to make a connection between $\dot{M}$ and $\dot{\varepsilon}$.

As seen in Figure 3-2, when the operating point is chosen out of the middle dead-zone, a linear relation between magnetization and elongation can be assumed. In this case $\dot{M} \propto \dot{\varepsilon}$ and by measuring $\dot{\varepsilon}$, $\dot{M}$ can be obtained and the stability results can be extended to velocity control.

The cost J is a nonlinear function of controller parameters and numerical minimization of J should be employed for optimum performance. Numerical optimization methods can be used to find a local minimum of a given function. There is no guarantee that the minimum found is the global minimum. If the initial condition for optimization is set too far from the global minimum, it is very likely that only a local minimum is found. For this reason, the following analysis was used to obtain an initial condition close to the optimum solution:

If a given controller C with transfer function $\hat{C}(s)$ satisfies equation (4.48), $\xi\hat{C}(s)$ satisfies the same inequality for any $\xi > 0$. However, poor performance was observed for large K_P or K_D experimentally. Similar behaviour was seen in the simulations. Figure 5-5 shows the simulated

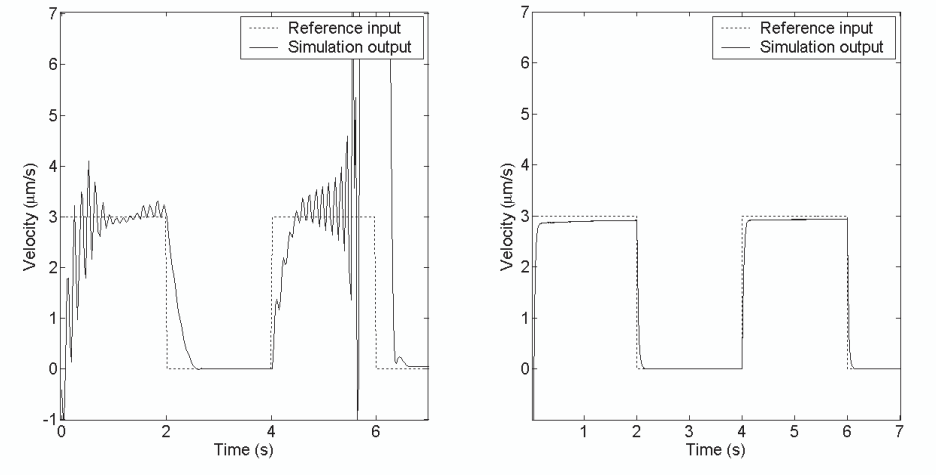

Figure 5-6: The controlled system response for $K_D = 20,000$ (left). Same simulation when the time step is 15 times smaller. (right).

system response for different values of K_P. Poor performance was experimentally observed for controllers with K_D higher than ~ 10000. Simulated system response for $K_D = 20,000$ is shown in Figure 5-6. The performance was significantly improved for a smaller time step. A higher upper-limit for K_D is expected if the sampling frequency is increased for the experiment.

Since typical values for K_P and K_I are much higher than $10,000$, for stabilizing controllers the effect of K_D term is negligible. Figure 5-7 shows steady-state error versus K_D for a typical controller. Less than 0.1% difference in steady-state error is seen when K_D goes from zero to the maximum. For simplicity, it is assumed that $K_D \approx 0$. It is obvious that multiplying both K_I and K_P by a constant number does not affect the closed-loop stability. The individual values of K_I and K_P do not affect stability; only the ratio $\frac{K_I}{K_P}$ is important.

As stated in Section 2, a PID controller cannot provide satisfactory performance. So intuitively, the double integration term $\frac{K_I}{(s+\alpha)^2}$ is responsible for driving the error to zero. It is expected that when K_I is large, this term is dominant and better performance is seen. The simulation results shown in Figure 5-8 verify this prediction. It was experimentally confirmed that controllers with higher K_I have better tracking performance.

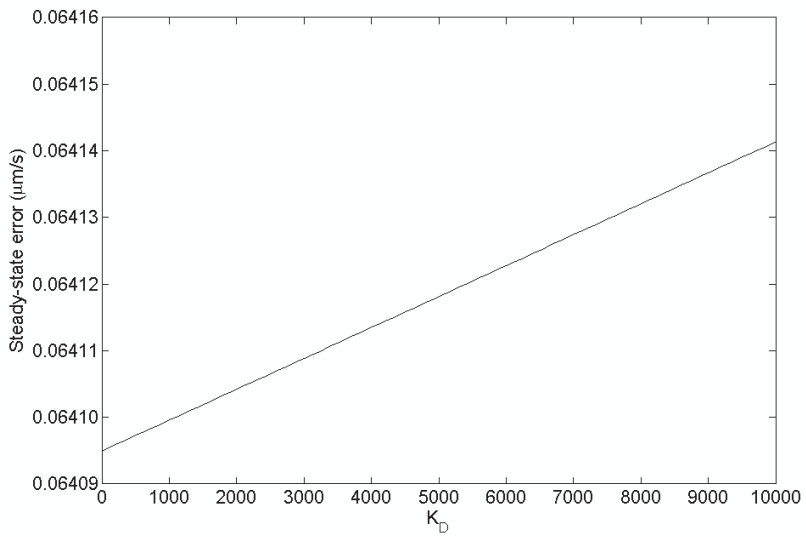

Figure 5-7: Steady-state error versus K_D; other parameters are constant.

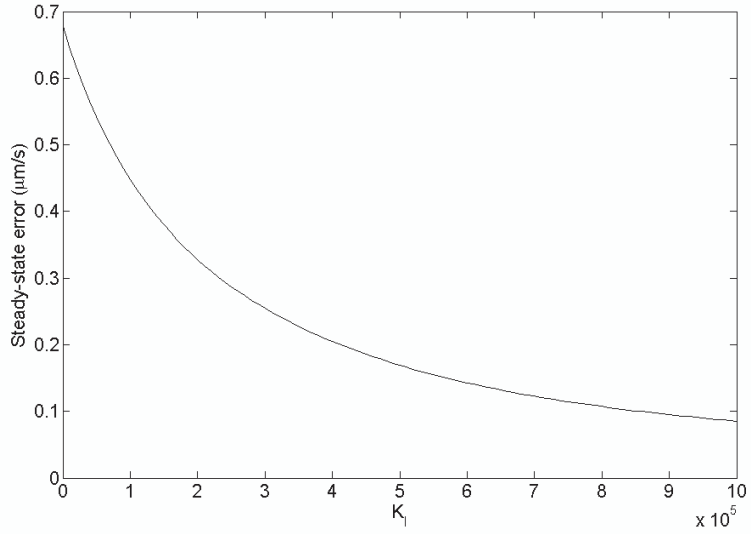

Figure 5-8: Steady-state error versus K_I when other parameters are constant.

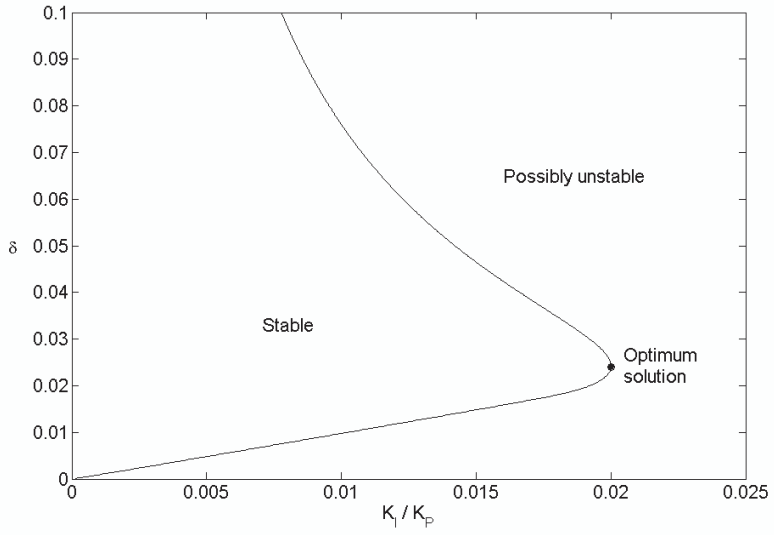

Figure 5-9: Phase plane of the system for $\alpha = 0.01$.

Setting $\alpha = 0.01$ and using inequality (4.48), values of δ and $\frac{K_I}{K_P}$ that stabilize the system are shown in Figure 5-9. Similar results are seen for other values of α. It is observed that the highest K_I can be achieved if $\delta = 0.024$. By choosing the largest K_P for which the controller is stable and using the value of $\frac{K_I}{K_P}$, K_I can be determined.

This process was repeated for different values of α. Figure 5-10 shows the steady-state error versus α obtained using simulation. Better performance is seen when α is reduced up to about 0.01. For smaller values of α, no noticeable difference is observed.

For $K_D \leq 10,000$, controlled system performance is almost independent of K_D. A large value for K_D increases α_2 in inequality (4.48). This makes the stability inequality stronger. For simplified inequality (4.51), it is also seen that larger K_D helps. For this reason the maximum value for K_D is chosen. The initial condition for optimization is chosen as follows: $\alpha = 0.01\frac{\text{rad}}{\text{s}}$, $\delta = 0.024\frac{\text{rad}}{\text{s}}$, $K_I = 32008\frac{\text{A rad}^2}{\text{m s}}$, $K_P = 1,600,000\frac{\text{A rad}}{\text{m}}$ and $K_D = 10,000\frac{\text{A s}}{\text{m}}$.

The function $J(K_P, K_I, K_D, \varepsilon_I, \varepsilon_D)$ is numerically minimized. The optimization is subjected to the stability condition (4.48). The optimum solution was found to be: $\alpha = 0.0106$, $\delta = 0.0231$,

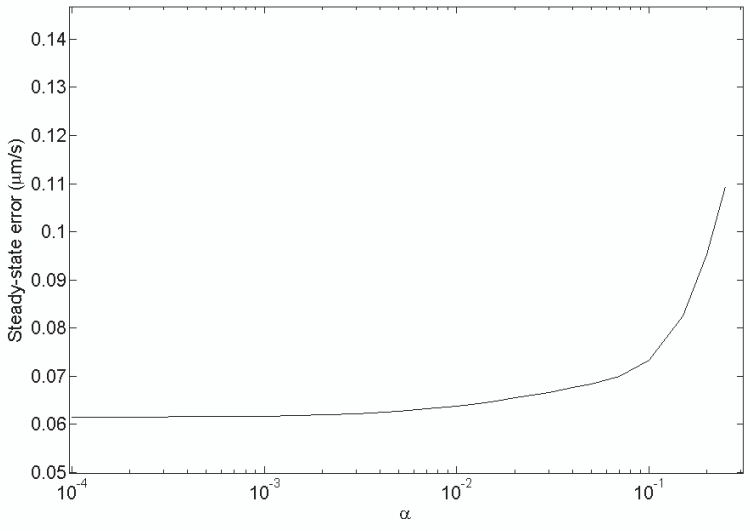

Figure 5-10: Steady-state error versus α when other parameters are optimized.

$K_I = 31788$, $K_P = 1,580,200$ and $K_D = 9904$. Since $\alpha \neq \delta$, relations (4.50) and (4.51) cannot be used. This controller satisfies inequality (4.48) with $\alpha_2 = 9904$.

Figure 5-11 displays the closed loop performance when the designed controller is implemented and the reference signal is a step. Good tracking is observed. The system settled within about 0.08s after the step, with a steady-state error of $0.09\frac{\mu\text{m}}{\text{s}}$ or 3% error. It was also observed that the current applied to the actuation unit was not large and the current amplifier did not reach the maximum current during the experiment.

Figure 5-12 compares the reference signal and measured velocity for the closed-loop system when the reference signal is sinusoidal with varying amplitude. Excellent tracking is seen. The RMS tracking errors is $0.71\frac{\mu\text{m}}{\text{s}}$, a relative RMS error of about 3.5%.

5.5 Monotonicity-based velocity control

Similar to the previous section, in the previous chapter, stability was established when $\dot{M}$ was being controlled. The approach used in the previous section is used here to provide velocity

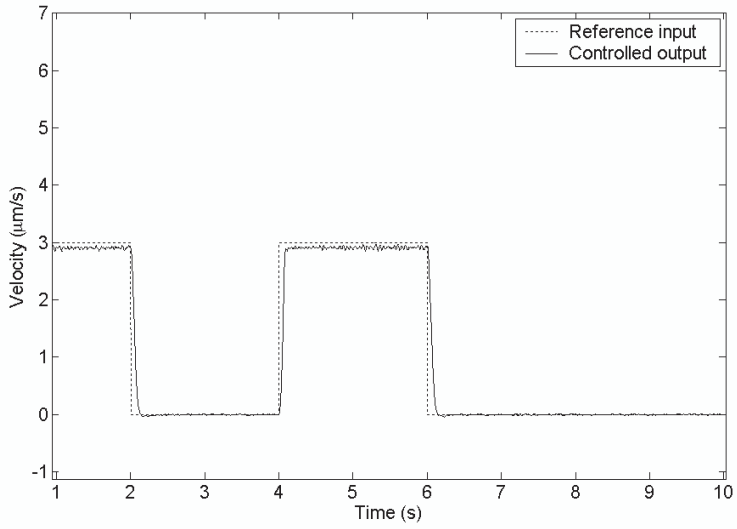

Figure 5-11: Experimental results for a step signal when velocity is being controlled.

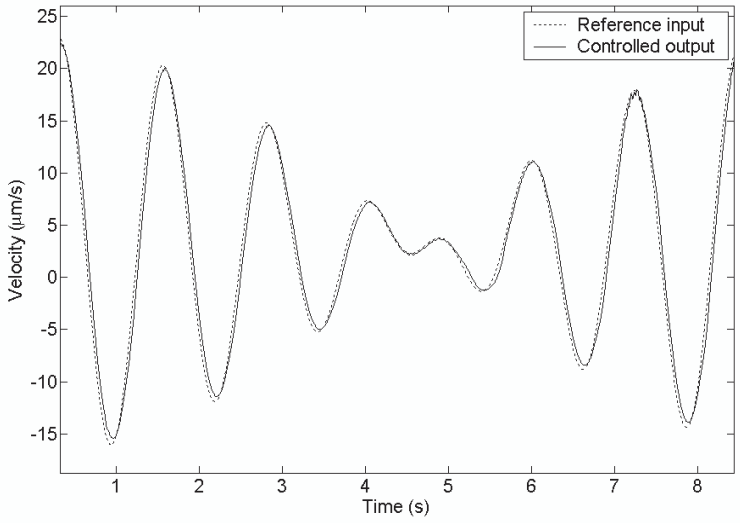

Figure 5-12: Experimental results for velocity control when the reference signal is sinusoidal with varying amplitude.

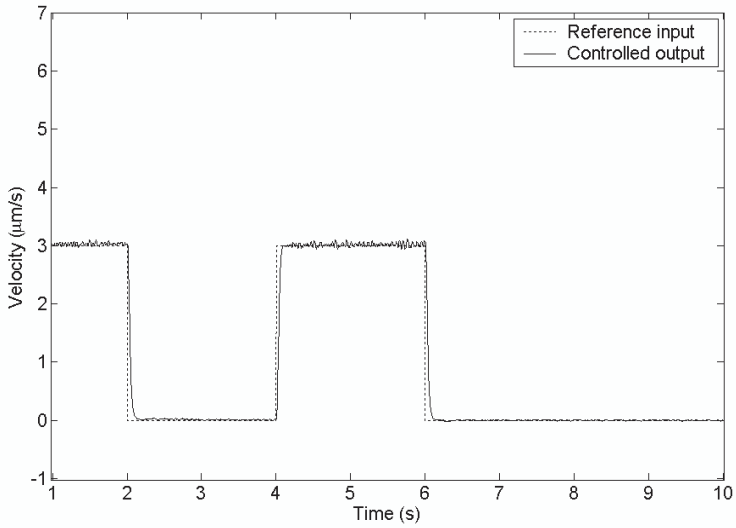

Figure 5-13: Experimental results for the step response of the monotonicity-based velocity controller.

control.

Since the stability conditions for this controller are more relaxed, the procedure used in the previous section is not required and direct optimization can be used. The controller parameters are found by numerical minimization of the cost function J. To provide consistency between the simulation and the experiment, a 10 ms delay is added to the simulation to model the power supply response time. The optimal controller parameters are: $\alpha = 9.3985 \times 10^{-10} \frac{\text{rad}}{\text{s}}$, $\delta = 2.0270 \times 10^{-3} \frac{\text{rad}}{\text{s}}$, $K_I = 1,875,900 \frac{\text{A rad}^2}{\text{m s}}$, $K_P = 1,734,100 \frac{\text{A rad}}{\text{m}}$ and $K_D = 10,153 \frac{\text{A s}}{\text{m}}$.

In Figure 5-13, the closed-loop response to step functions are displayed when the controller is tested experimentally. The results are slightly better than that of the energy-based velocity controller. The system settled within 0.06 s of the steps with no steady-state error. Because the stability inequalities for this controller are more relaxed, a better controller is obtained.

Figure 5-14 shows the closed-loop response when the input is a sinusoidal signal with varying amplitude. Compared to the previous section, more oscillations about the reference signal are seen. The root-mean-square error is $0.73 \frac{\mu\text{m}}{\text{s}}$ or about 3.6%, which is slightly higher than

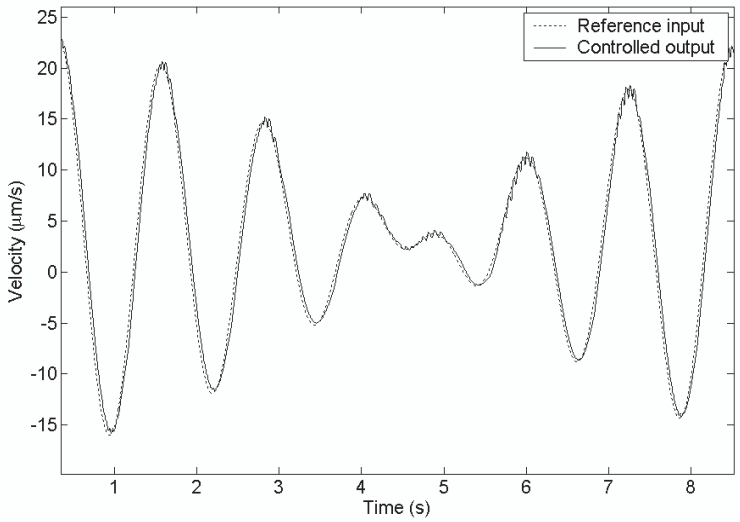

Figure 5-14: Tracking of the monotonicity-based velocity controller when the reference signal is sinusoidal with varying amplitude.

the previous controller. The oscillations shown in Figure 5-14 imply that the system is close to marginal stability. For the previous section, conservative stability inequalities caused the closed-loop system to be far from instability.

5.6 Position control of magnetostrictive actuators

In the previous chapter, the position control of a Preisach model was discussed. Since the Preisach model can accurately represent the relation between the magnetic field H and magnetization M for magnetostrictive materials, the result from the previous chapter can be used to control the magnetization. Similar to the previous sections, in most applications, the control of mechanical variables is desired. In this section, the elongation produced by the magnetostrictive actuator is controlled.

The relation between magnetization and elongation is given by equation (3.2). Using this relation, position control can be achieved by controlling the magnetization M.

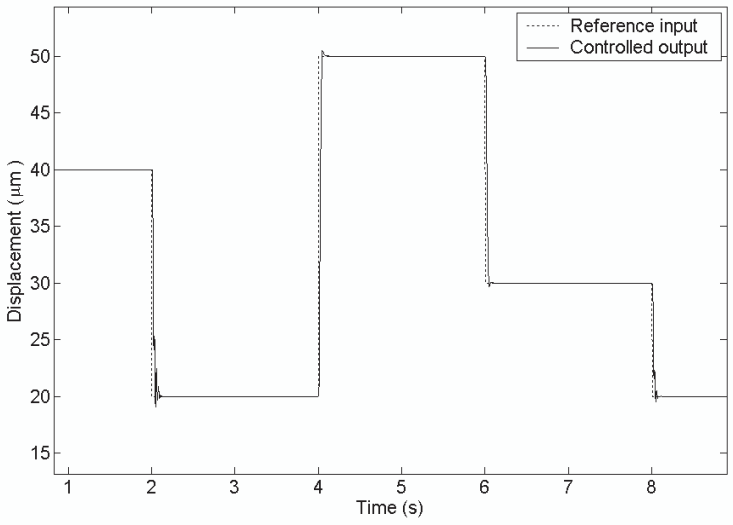

Figure 5-15: The closed-loop response to various steps.

To obtain the magnetization in the actuator, output displacement is measured by an optical encoder and (3.2) is used to compute magnetization. Since the same relation is used to compute the desired magnetization, errors introduced by (3.2) do not affect the closed-loop performance.

The controller parameters are found by numerical minimization of the cost function J subject to the stability inequalities. (assumption (B1).) The optimum values for the controller gains are: $K_I = 38.02\,\mathrm{s}^{-1}$ and $K_P = 0.0785$.

Figure 5-15 displays the closed-loop response of the system to step input for optimized controller. Excellent tracking is observed. Portions of this figure are magnified in Figures 5-16 and 5-17. There is no steady-state error as predicted by Theorem 28 in the previous chapter. A small overshoot is seen in Figures 5-16 and 5-17. Theorem 29 implies that there is no overshoot in the closed-loop system. This overshoot may be caused by some unmodeled mass in the system and possibly discontinuities in the reference signal.

In Figure 5-16, simulation results and experimental data are compared. Reasonable agreement is seen. The experimental curve follows the simulation with an initial delay and some vibration. It is believed that these differences are caused by a moving mass and stiffness of the

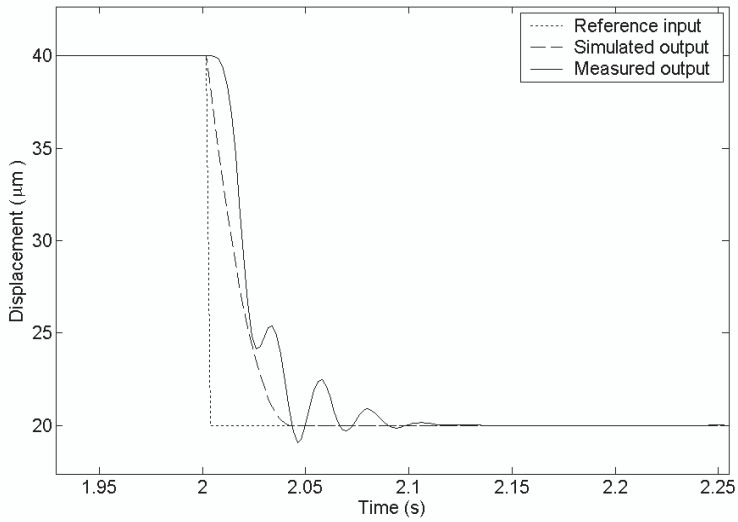

Figure 5-16: Transient response after a step. The effects of a moving mass are seen.

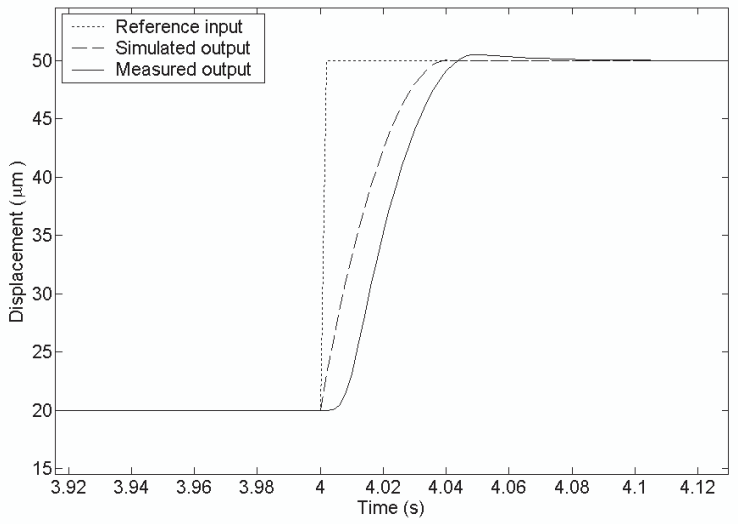

Figure 5-17: Transient response after a step. No vibration is seen.

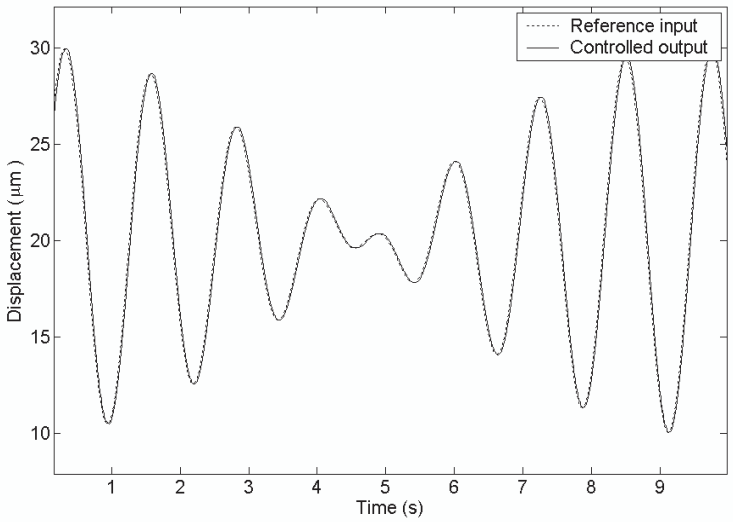

Figure 5-18: Tracking response of the closed loop.

system. In Figure 5-17, similar comparison is done for another step. The initial delay is seen but no vibration can be observed. The nonlinear nature of the system can exhibit different responses for different conditions. The system settles to $\pm 10\,\text{nm}$ of the reference signal in $0.175\,\text{s}$ and $0.122\,\text{s}$ in Figures 5-16 and 5-17, respectively.

The system response to a sinusoidal input with varying amplitude is shown in Figure 5-18. The given trajectory is followed accurately. Figure 5-19 shows the tracking error for the same experiment. The root-mean-square tracking error is $0.11\,\mu\text{m}$ or 1.1%.

In the next chapter, this thesis is concluded.

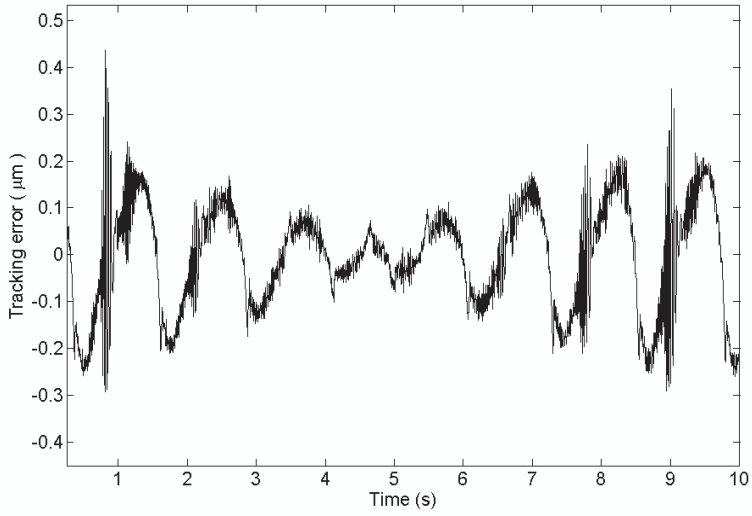

Figure 5-19: Tracking error of the closed loop.

Chapter 6

Conclusions

In this thesis, the details of recent analysis, modeling and control of Terfenol-D were discussed. The test rig has been upgraded and new experiments were performed to evaluate an existing load-dependent hysteresis model and develop a new one. The passivity of magnetostrictive systems was used to develop a velocity controller. By using the properties of the Preisach model, an alternative velocity controller and a position controller was developed.

Before a Terfenol-D actuator can be used for a nanopositioning task, an accurate model for the material should be available. This model is used to simulate the response of the material and optimize the input for desired operation. The model should be able to predict the material response for any input magnetic field and load condition. It was observed that the response of Terfenol-D depends on loading conditions significantly. As a result, the effects of the load needs to be included in the hysteresis model.

Because of the importance of minor loops for control applications, the hysteresis model should reproduce the minor loops correctly. A set of experimental data was obtained and used to find the model parameters for a Preisach model with a general weight function, the homogenized energy model with Gaussian and log-normal weight functions, and the Jiles-Atherton model. A second set of experimental data was used to evaluate the accuracy of the models in reproducing the minor loops. It was shown that the Preisach model with a general weight function provides the best accuracy.

To analyze the load-dependent hysteresis of Terfenol-D, a set of hysteresis curves at different loads was obtained. This set was used to identify the model parameter for an existing load-dependent hysteresis model. The hysteresis curves generated by the model were discussed. A modification to the model was proposed and shown to provide more accuracy at low stresses.

Using the balance of energy, a new load-dependent model was developed. In the new model, a Preisach model with a general weight function is used. As a result, the model inherited some of the properties of the Preisach model. The new model can generate minor loops consistently and provides accurate results at different stresses.

A closed loop feedback system is required to achieve the required accuracy and performance. Physical conditions such as mechanical loading affect the hysteretic behaviour of magnetostrictive materials. Dependence of hysteresis on many physical conditions together with intrinsic nonlinearity of the system make it difficult and challenging to design a feedback control system.

In this proposal, the passivity approach was used to design a controller and establish stability. A passivity framework was developed and it was shown that under certain conditions, the system is passive. The associated storage function was also studied. This result was used to develop a closed-loop velocity controller for the material.

Using the properties of hysteretic systems, an alternative approach for showing stability and controller design was developed. It was shown that the Preisach model satisfies the requirements. This new approach can be used not only for magnetostrictive materials, but also for many other hysteretic systems. The results were used to develop an alternative velocity controller based on the monotonicity of the Preisach model. For position control, a PI controller was used. It was shown that if certain assumptions are satisfied, zero steady-state error is guaranteed. In addition, L_∞-stability of the closed loop was proven. It was also shown that under certain conditions, the controller will not exhibit an overshoot.

The controllers developed in this thesis were optimized by simulation and numerical optimization. For the simulation, a Preisach model with a general weight function was used. The controllers were evaluated experimentally. The responses for different inputs to the closed loop were compared and discussed.

The following future work is proposed:

1. The assumptions proven for the Preisach model can be investigated for other hysteresis models. If the assumptions can be proven, the results presented here can be used for many hysteresis models.

2. There are many hysteretic system that can be represented by the Preisach model. The results presented here can be used to develop controllers for these systems.

3. The new load-dependent hysteresis model can be inverted to develop a model inverse-based controller.

4. The effects of eddy currents and the actuator mass can be included to have a rate-dependent hysteresis model.

5. In this thesis, the energy-based passivity results apply only at a constant temperature. A new storage function should be found to extend the results when the temperature is not constant.

Appendix A

The maximization of entropy

In this appendix, it is shown that the entropy function equation (4.21) is maximized when $H = 0$.

From Subsection 4.2.2, the following relations define entropy for a paramagnetic sample with N dipoles:

$$\begin{aligned} Z &= \frac{\sinh\left[(J+\frac{1}{2})\eta\right]}{\sinh\left[\frac{1}{2}\eta\right]}, \\ S &= kN\left(\ln Z - \beta\frac{\partial \ln Z}{\partial \beta}\right), \\ \eta &= c\beta\left\|H\right\|, \\ \beta &= \frac{1}{kT}, \end{aligned} \tag{A.1}$$

where c is a positive constant.

Define $D = \frac{\eta}{2} = \frac{c\beta}{2}\left\|H\right\|$ and $q = 2J + 1$. Since J is a positive half-integer, q is an integer greater than one. We can write

$$S = kN\left(\ln\frac{\sinh qD}{\sinh D} - qD\coth qD + D\coth D\right). \tag{A.2}$$

This function is not defined at $D = 0$, but $\lim_{D\to 0} S(D)$ exists:

$$\begin{aligned}
\lim_{D\to 0} S(D) &= \lim_{D\longrightarrow 0} kN\left(\ln\frac{\sinh qD}{\sinh D} + \frac{D\cosh D\sinh qD - qD\cosh qD\sinh D}{\sinh D\sinh qD}\right) \\
&= \lim_{D\longrightarrow 0} kN\left(\ln\frac{qD + h.o.t.}{D + h.o.t.} + \frac{\frac{D^4}{6}(2q - 2q^3) + h.o.t.}{qD^2 + h.o.t.}\right) \\
&= kN\ln q.
\end{aligned} \tag{A.3}$$

For $D \neq 0$, $S(D) = S(-D)$; i.e., this is an even function. We don't need to analyze this function for both positive and negative values of D. For simplicity $D > 0$ is studied.

If $D > 0$,

$$\frac{dS}{dD} = kN\left(\frac{q^2 D}{\sinh^2 qD} - \frac{D}{\sinh^2 D}\right). \tag{A.4}$$

It will be shown that for $D > 0$, $\frac{dS}{dD} < 0$. Consider the Taylor series of the following expression:

$$\begin{aligned}
\sinh qD - q\sinh D &= qD + \frac{q^3D^3}{3!} + \frac{q^5D^5}{5!} + \cdots - qD - \frac{qD^3}{3!} - \frac{qD^5}{5!} - \cdots \\
&= q\left((q^2-1)\frac{D^3}{3!} + (q^4-1)\frac{D^5}{5!} + \cdots\right).
\end{aligned} \tag{A.5}$$

Since $q > 1$ and $D > 0$ all of the terms in the Taylor series are positive. It follows that

$$\sinh qD - q\sinh D > 0. \tag{A.6}$$

This inequality can be written as

$$1 < \frac{\sinh qD}{q \sinh D}. \tag{A.7}$$

or

$$1 < \frac{\sinh^2 qD}{q^2 \sinh^2 D}. \tag{A.8}$$

This inequality can be further written as

$$\frac{q^2}{\sinh^2 qD} - \frac{1}{\sinh^2 D} < 0. \tag{A.9}$$

By rewriting equation (A.4), the terms in equation (A.9) appear in the derivative of S with respect to D.

$$\frac{dS}{dD} = kND\left(\frac{q^2}{\sinh^2 qD} - \frac{1}{\sinh^2 D}\right). \tag{A.10}$$

Since $D > 0$, this implies that $\frac{dS}{dD} < 0$.

Since $\frac{dS}{dD} < 0$, S can be increased by lowering D, or

$$\sup_{D>0} S(D) = \lim_{D\to 0} S(D) = kN \ln q. \tag{A.11}$$

Since $S(D)$ is an even function, this result can be extended to all values of $D \neq 0$: $kN \ln q$ is an upper bound for $S(D)$.

Appendix B

Proof of Theorem 29 for $K_P = 0$

In this appendix, Theorem 29 is proven when $K_P = 0$. For nonzero K_P, the proof is included in Chapter 4.

Theorem 29 *Assume that assumptions (A1), (A4), (B1) and (B2) hold and $r \in L_\infty$. Further, assume that $u(0) = 0$. If $|y(0)| \leq \|r\|_\infty$, then $\|y\|_\infty \leq \|r\|_\infty$.*

Proof. Assume $K_P = 0$. Equation (4.86) simplifies to

$$u(t) = K_I f(t) \tag{B.1}$$

where $f(t)$ is defined in equation (4.85).

Define L to be

$$L = \|r\|_\infty . \tag{B.2}$$

Assume that for some t_f,

$$y(t_f) > L. \tag{B.3}$$

Define $t_{\max f}$ to be the time at which $f(t)$ is maximized on $[0, t_f]$:

$$f(t_{\max f}) \geq f(t), \forall t \in [0, t_f]. \tag{B.4}$$

Using equation (B.1),

$$u(t_{\max f}) \geq u(t), \forall t \in [0, t_f]. \tag{B.5}$$

Using assumption (A4), we have:

$$y(t_{\max f}) \geq y(t_f). \tag{B.6}$$

Using equation (B.3), we have:

$$e(t_{\max f}) = r(t_{\max f}) - y(t_{\max f}) < 0. \tag{B.7}$$

Using assumptions (A1) and (B2), $y(t)$ is continuous. By using assumption (B2) again, it is found that $e(t)$ is continuous. Equations (B.2) and (B.3) imply that $e(t_f) < 0$. Using continuity of $e(t)$, there is a neighborhood around t_f at which, $e(t) < 0$. Since $\dot{f}(t) = e(t)$, f is strictly decreasing in this neighborhood. As a result, $f(t)$ is not maximized at t_f:

$$t_{\max f} \neq t_f. \tag{B.8}$$

Since $e(t)$ is continuous and $\dot{f}(t) = e(t)$, $f(t)$ is continuously differentiable. If $t_{\max f} \neq 0$, maximization of $f(t)$ at $t_{\max f}$ implies that $\dot{f}(t_{\max f}) = 0$ or,

$$e(t_{\max f}) = 0, \text{ if } t_{\max f} \neq 0. \tag{B.9}$$

By comparing with equation (B.7), the following conclusion is obtained:

$$t_{\max f} = 0. \tag{B.10}$$

By combining equations (B.3) and (B.6), we have

$$y(0) \geq y(t_f) > L. \tag{B.11}$$

Similarly, if $y(t_f) < -L$, $y(0) < -L$. Thus $|y(0)| \leq \|r\|_\infty$ implies that $\|y\|_\infty \leq \|r\|_\infty$. ■

Bibliography

[1] A. A. Adly, I. D. Mayergoyz, and A. Bergqvist. Utilizing anisotropic Preisach-type models in the accurate simulation of magnetostriction. *IEEE transaction on magnetics.* vol. 33, no. 5, September 1997, pp. 3931-3933.

[2] P. Akella and J. T. Wen. Synthesized passive feedback control of sensor-rich smart structures - experimental results. *Proceedings, IEEE conference on control applications.* 1995, pp. 1098-1103.

[3] W. D. Armstrong. A directional magnetization potential based model of magnetoelastic hysteresis. *Journal of applied physics.* vol. 91, no. 4, Feb. 2002, pp. 2202-10.

[4] D. L. Atherton and J. R. Beattie. A mean field Stoner-Wohlfarth hysteresis model. *IEEE transaction on magnetics.* vol. 26, no. 6, November 1990, pp. 3059-3063.

[5] V. Basso and G. Bertotti. Hysteresis models for the description of domain wall motion. *IEEE transactions on magnetics.* vol. 32, no. 5, September 1996, pp. 4210-4212.

[6] A. Bergqvist and G. Engdahl. A stress-dependent magnetic Preisach hysteresis model. *IEEE transactions on magnetics.* vol. 27, no. 6, November 1991, pp. 4796-98.

[7] D. P. Bertsekas. *Nonlinear Programming.* Athena Scientific, Belmont, Massachusetts, 1999.

[8] T. R. Braun and R. C. Smith. Efficient implementation algorithms for homogenized energy models. *Continuum mech. thermodyn.* vol. 18, 2006, pp. 137-155.

[9] T. R. Braun, R. C. Smith, and M. J. Dapino. Experimental validation of a homogenized energy model for magnetic after-effects. *Applied physics letters.* vol. 88, 2006, pp. 122511-3.

[10] K. H. Carpenter. A differential equation approach to minor loops in the Jiles-Atherton hysteresis model. *IEEE transactions on magnetics*. vol. 27, no. 6, Nov. 1991, pp. 4404-6.

[11] K. Cohen, T. Weller, and J. Z. Ben-Asher. Active control of flexible structures using a fuzzy logic algorithm. *Smart materials and structures*. vol. 11, no. 4, August 2002, pp. 541-552.

[12] C. J. Damaren and D. C. Oguamanam. Vibration control of spacecraft box structures using a collocated piezo-actuator/sensor. *Journal of intelligent material systems and structures*. vol. 15, May 2004, pp. 369-374.

[13] M. J. Dapino, R. C. Smith, L. E. Faidley, and A. B. Flatau. A coupled structural-magnetic strain and stress model for magnetostrictive transducers. *Journal of intelligent material systems and structures*. vol. 11, February 2000, pp. 135-152.

[14] C. A. Desoer and M. Vidyasagar. *Feedback systems: input-output properties*. Academic Press, New York, 1975.

[15] L. R. Dupre, R. Van Keer, and J. A. A. Melkebeek. Evaluation of magnetostrictive effects in soft magnetic materials using the Preisach theory. *Journal of magnetism and magnetic materials*. vol. 254-255, 2003, pp. 121-123.

[16] R. B. Gorbet. *Control of hysteretic systems with Preisach representations*. PhD thesis, University of Waterloo, Department of Electrical Engineering, 1997.

[17] R. B. Gorbet, K. A. Morris, and D. W. L. Wang. Control of hysteretic systems: a state-space approach. *Learning, control, and hybrid systems*. Edited by Y. Yamamoto, S. Hara, B. A. Francis and M. Vidyasagar, Springer-Verlag, New York, 1998, pp. 432-451.

[18] R. B. Gorbet, K. A. Morris, and D. W. L. Wang. Passivity-based stability and control of hysteresis in smart actuators. *IEEE transactions on control systems technology*. vol. 9, no. 1, January 2001, pp. 5-16.

[19] D. Hughes and J. T. Wen. Preisach modeling of piezoceramic and shape memory alloy hysteresis. *Smart materials and structures*. vol. 6, 1997, pp. 287-300.

[20] ETREMA Products Inc. WWW document, 2003. http://etrema-usa.com/core/terfenold/.

[21] D. C. Jiles. A self consistent generalized model for the calculation of minor loop excursions in the theory of hysteresis. *IEEE transaction on magnetics*. vol. 28, no. 5, September 1992, pp. 2602-2604.

[22] D. C. Jiles. Theory of the magnetomechanical effect. *Journal of physics D: applied physics*. vol. 28, no. 8, 14 August 1995, pp. 1537-1546.

[23] D. C. Jiles and D. L. Atherton. Theory of ferromagnetic hysteresis. *Journal of magnetism and magnetics materials*. vol. 61, 1986, pp. 48-60.

[24] D. C. Jiles and D. L. Atherton. Theory of ferromagnetic hysteresis. *Journal of applied physics*. vol. 55, no. 6, March 1984, pp. 2115-2120.

[25] D. C. Jiles and J. B. Thoelke. Modelling of the combined effects of stress and anisotropy on the magnetostriction of $Tb_{0.3}Dy_{0.7}Fe_2$. *IEEE transactions on magnetics*. vol. 27, no. 6, November 1991, pp. 5352-5354.

[26] D. C. Jiles and J. B. Thoelke. Theoretical modelling of the effects of anisotropy and stress on the magnetization and magnetostriction of $Tb_{0.3}Dy_{0.7}Fe_2$. *Journal of magnetism and magnetic materials*. vol. 134, 1994, pp. 143-160.

[27] M. A. Krasnosel'skii and A. V. Pokrovskii. *Systems with hysteresis*. Springer-Verlag, Berlin, Translated from Russian, 1989.

[28] P. Langevin. Magnetisme et theorie des electrons. *Ann. chim. et phys.* vol 5, 1905, p. 245.

[29] F. Liorzou, B. Phelps, and D. L. Atherton. Macroscopic models of magnetization. *IEEE transaction on magnetics*. vol. 36, no. 2, March 2000, pp. 418-428.

[30] H. Logemann and A. D. Mawby. Low-gain integral control of infinite-dimensional regular linear systems subject to input hysteresis. *Advances in mathematical systems theory*. Edited by F. Colonius et al., Birkhauser, Boston, 2001, pp. 255-293.

[31] H. Logemann, E. P. Ryan, and I. Shvartsman. A class of differential-delay systems with hysteresis: asymptotic behaviour of solutions. *Nonlinear analysis*. submitted.

[32] H. Logemann, E. P. Ryan, and I. Shvartsman. Integral control of infinite-dimensional systems in the presence of hysteresis: an input-output approach. *ESAIM - control, optimisation and calculus of variations*. to appear.

[33] I. Mayergoyz. *Mathematical models of hysteresis and their applications*. Elsevier Academic Press, Amsterdam, Boston, 2003.

[34] P. Nakmahachalasint, K. D. T. Ngo, and L. Vu-Quoc. A static hysteresis model for power ferrites. *IEEE transactions on power electronics*. vol. 17, no. 4, July 2002, pp. 453-460.

[35] M. H. Nayfeh and M. K. Brussel. *Electricity and magnetism*. John Wiley and sons, 1985.

[36] J. Nealis and R. C. Smith. An adaptive control method for magnetostrictive transducers with hysteresis. *Proceedings, IEEE conference on decision and control*. vol. 5, 2001, pp. 4260-4265.

[37] J. M. Nealis and R. C. Smith. Model-based robust control design for magnetostrictive transducers operating in hysteretic and nonlinear regimes. *IEEE transactions on control systems technology*. vol. 15, no. 1, January 2007, pp. 22-39.

[38] J. M. Nealis and R. C. Smith. Robust control of a magnetostrictive actuator. *Proceedings of SPIE, the international society for optical engineering*. vol. 5049, 2003, pp. 221-232.

[39] W. S. Oates and R. C. Smith. Nonlinear perturbation control for magnetic transducers. *Proceedings of the 45th IEEE conference on decision and control*. 2006, pp. 2441-6.

[40] W. J. Park, D. R. Son, and Z. H. Lee. Modeling of magnetostriction in grain aligned Terfenol-D and preferred orientation change of Terfenol-D dendrites. *Journal of magnetism and magnetic materials*. vol. 248, 2002, pp. 223-229.

[41] M. Pasquale, C. Sasso, and S. H. Lim. Analysis and optimization of the magnetomechanical properties of Terfenol-D composites at audio frequencies. *IEEE transaction on magnetics*. vol. 35, no. 5, September 1999, pp. 3829-3831.

[42] F. Reif. *Fundamentals of statistical and thermal physics*. McGraw-Hill Book Company, New York, 1965.

[43] J. J. Rousseau, L. Zegadi, and P. Tenant. A complete hysteresis model for soft ferrites taking into account the temperature. *PESC record - IEEE annual power electronics specialists conference*. vol. 1, 1996, pp. 322-328.

[44] M. J. Sablik and D. C. Jiles. Coupled magnetoelastic theory of magnetic and magnetostrictive hysteresis. *IEEE transactions on magnetics*. vol. 29, no. 3, July 1993, pp. 2113-2123.

[45] R. C. Smith. A nonlinear optimal control method for magnetostrictive actuators. *Journal of intelligent material systems and structures*. vol. 9, no. 6, June 1998, pp. 468-485.

[46] R. C. Smith. *Smart material systems: model development*. Frontiers appl. Math. 32, society of industrial and applied mathematics, Philadelphia, 2005.

[47] R. C. Smith and M. J. Dapino. A homogenized energy model for the direct magnetomechanical effect. *IEEE transactions on magnetics*. vol. 42, no. 8, August 2006, pp. 1944-1957.

[48] R. C. Smith, M. J. Dapino, T. R. Braun, and A. P. Mortensen. A homogenized energy framework for ferromagnetic hysteresis. *IEEE transactions on magnetics*. vol. 42, no. 7, July 2006, pp. 1747-1769.

[49] R. C. Smith, M. J. Dapino, and S. Seelecke. Free energy model for hysteresis in magnetostrictive transducers. *Journal of applied physics*. vol. 93, no. 1, 1 January 2003, pp. 458-466.

[50] R. C. Smith and A. G. Hatch. Parameter estimation techniques for a class of nonlinear hysteresis models. *Inverse problems*. vol. 21, 2005, pp. 1363-1377.

[51] R. C. Smith, A. G. Hatch, B. Mukherjee, and S. Liu. A homogenized energy model for hysteresis in ferroelectric materials: general density formulation. *Journal of intelligent material systems and structures*. vol. 16, September 2005, pp. 713-732.

[52] R. C. Smith and J. E. Massad. A unified methodology for modeling hysteresis in ferroic materials. *Proceedings of the ASME design engineering technical conference*. vol. 6B, 2001, pp. 1389-1398.

[53] R. C. Smith and S. Seelecke. An energy formulation for Preisach models. *Proceedings of SPIE - the international society for optical engineering.* vol. 4693, 2002, pp. 173-182.

[54] R. C. Smith, S. Seelecke, Z. Ounaies, and J. Smith. A free energy model for hysteresis in ferroelectric materials. *Journal of intelligent material systems and structures.* vol. 14, no. 11, November 2003, pp. 719-739.

[55] E. C. Stoner and E. P. Wohlfarth. A mechanism of magnetic hysteresis in heterogeneous alloys. *Phil. trans. roy. soc.* vol. 240A, May 4, 1948, pp. 599-642.

[56] X. Tan and J. S. Baras. Modeling and control of hysteresis in magnetostrictive actuators. *Automatica.* vol. 40, no. 9, September 2004, pp. 1469-1480.

[57] S. Valadkhan. Modeling of magnetostrictive materials. Master's thesis, University of Waterloo, Department of Mechanical Engineering, 2004.

[58] S. Valadkhan, K. A. Morris, and A. Khajepour. Comparison of hysteresis models for magnetostrictive materials. *Proceedings, 7th cansmart workshop on smart materials and structures.* Montreal, Quebec, October 2004, pp. 133-142.

[59] S. Valadkhan, K. A. Morris, and A. Khajepour. Modeling of magnetostrictive materials under different load conditions. *Proceedings, 8th cansmart workshop on smart materials and structures.* Toronto, Ontario, Canada, October 2005, pp. 281-288.

[60] S. Valadkhan, K. A. Morris, and A. Khajepour. Passivity-based control of magnetostrictive actuators. *IEEE transactions on control systems technology.* submitted.

[61] S. Valadkhan, K. A. Morris, and A. Khajepour. Passivity of magnetostrictive materials. *SIAM Journal of applied mathematics.* vol. 67, no. 3, 2007, pp. 667-686.

[62] S. Valadkhan, K. A. Morris, and A. Khajepour. A review and comparison of hysteresis models for magnetostrictive materials. *Journal of intelligent material systems and structures.* submitted.

[63] M. Vidyasagar. *Nonlinear systems analysis.* Prentice hall, Englewood Cliffs, New Jersey, 1993.

[64] A. Visintin. *Differential models of hysteresis*. Springer-Verlag, New York, 1994.

[65] C. Visone and C. Serpico. Hysteresis operators for the modeling of magnetostrictive material. *Physica B*. vol. 306, 2001, pp. 78-83.

[66] J. C. Willems. Dissipative dynamical systems, part I: general theory. *Archives for rational mechanics and analysis*. vol. 45, 1972, pp. 321-351.

[67] M. W. Zemansky and R. H. Dittman. *Heat and thermodynamics*. McGraw-Hill Book Company, New York, Montreal, 1981.